

Flexure mechanisms for upper-limb support

Towards compliant wearable assistive devices

Martin Tschiersky



Flexure mechanisms for upper-limb support

Towards compliant wearable assistive devices

Martin Tschiersky

The graduation committee is composed of

chairman and secretary	prof. dr. ir. H.F.J.M. Koopman	Universiteit Twente
supervisors	prof. dr. ir. D.M. Brouwer, PDEng prof. dr. ir. J.L. Herder	Universiteit Twente Technische Universiteit Delft
members	prof. dr. ir. D. Lefeber Prof. C.J. Walsh, Ph.D. prof. dr. ir. H. van der Kooij prof. dr. J.S. Rietman	Vrije Universiteit Brussel Harvard University Universiteit Twente Universiteit Twente

In his capacity as daily supervisor ir. E.E.G. Hekman has significantly contributed to the creation of this thesis.

This work was supported by the European Union's Horizon 2020 research and innovation programme under grant agreement No. 688857 (SoftPro) and by the Japan Society for the Promotion of Science (JSPS) under the FY 2019 JSPS Postdoctoral Fellowship for Research in Japan (Short-term) PE19704.

The content of this publication is the sole responsibility of the author.

Cover design by M. Tschiersky.

Page layout based on templates from M. Nijenhuis and J.J. de Jong.

ISBN: 978-90-365-5134-2

DOI: 10.3990/1.9789036551342

© 2021 Martin Tschiersky, The Netherlands.

All rights reserved. No parts of this thesis may be reproduced, stored in a retrieval system or transmitted in any form or by any means without permission of the author.

Alle rechten voorbehouden. Niets uit deze uitgave mag worden vermenigvuldigd, in enige vorm of op enige wijze, zonder voorafgaande toestemming van de auteur.

Alle Rechte vorbehalten. Vervielfältigung, Bereitstellung und Übermittlung jeglicher Art und Weise, auch in Auszügen, nur mit ausdrücklicher Genehmigung des Autors.

FLEXURE MECHANISMS FOR UPPER-LIMB SUPPORT
TOWARDS COMPLIANT WEARABLE ASSISTIVE DEVICES

DISSERTATION

to obtain
the degree of doctor at the University of Twente,
on the authority of the rector magnificus,
prof. dr. ir. A. Veldkamp,
on account of the decision of the Doctorate Board,
to be publicly defended
on Friday the 30th of April 2021 at 16:45 hours

by

Martin Tschiersky

born on the 17th of May 1989
in Düsseldorf, Germany

This dissertation has been approved by

the supervisors

prof. dr. ir. D.M. Brouwer, PDEng

prof. dr. ir. J.L. Herder

Summary

Upper-limb wearable assistive devices are used to facilitate arm movements of their wearer. Thus, they can restore or enhance the ability to execute manual tasks. A prominent subclass is formed by the gravity-compensating devices. These are designed to dynamically support the weight of the wearer's limbs and that of manipulated objects, and thereby reduce the effort to raise the arms and to maintain certain poses. They are used to administer physical therapy, assist people suffering from insufficient muscle strength, and support healthy users in order to prevent injury or enhance their physical capabilities. Traditional gravity-compensating wearable assistive devices are predominantly conceptualized as rigid-link mechanisms. These consist of rigid links and conventional joints which form a support structure encompassing the wearer's body. This support structure, which is the eponymous characteristic of assistive exoskeletons, offers several advantages, for example, allowing to employ powerful actuators and absorb heavy loads. However, it can also be encumbering, negatively affecting wearing comfort and aesthetic appearance.

In order to address this issue, this thesis aims to incorporate structural compliance as an integral design paradigm into the conception of upper-limb wearable assistive devices. To this end, a holistic approach is pursued in which flexible structures integrate several subfunctions, and thereby simultaneously act as energy-storing springs, as complex transmission mechanisms, and as the load-bearing structure. This function integration is applied as a means to reduce size and weight, and thus enable close-fitting designs that, in combination with the inherent structural compliance, can provide comfortable support while potentially being concealable underneath clothing. Following this approach, and by employing numerical multibody models together with global optimization techniques, compliant mechanisms for both passive and active applications were synthesized.

With respect to the passive applications, flexures, i.e., flexible members were used to build compliant mechanisms that provide gravity balancing to different parts of the upper limbs, while pursuing close-to-body alignment and a high degree of biomechanical compatibility. The synthesis methodology has been first conceived and developed for a mechanism which is laterally applied to the elbow and provides gravity balancing to the forearm, and was later extended to provide gravity balancing to the upper arm when applied at the shoulder, partially enclosing the wearer's upper body. In comparison to previous research on flexure-based gravity balancing, several fundamental concepts were uncovered which turned out to be essential for achieving the necessary performance and making the mechanisms compatible for application in close proximity to the body. This includes the use of flexures with a variable thickness along their length to increase the performance relative to size and weight, and improve

robustness of the balancing behavior when dealing with spatial constraints. Moreover, adjusting the kinematic support conditions of the flexure led to further improvements in the handling of spatial constraints, whereby protrusion from the body can be significantly reduced. These kinematic adjustments also proved vital for lowering undesired interface forces and moments, and thus considerably mitigate the need for dedicated load-bearing structures.

In the context of active applications, i.e., actuated compliant devices, a new type of bending actuator was created. By combining flexures with McKibben muscles, this actuator features a low height that makes it potentially suitable to be deployed underneath clothing. For this active application, the use of a flexure-based architecture provides an effective means to achieve an adequate transmission behavior and utilize small actuator strokes within a confined space.

Overall, this thesis shows that flexure-based designs provide promising new solutions to improve upper-limb wearable assistive devices across a wide range of applications. Aside from proposing concrete designs which offer practical alternatives to the traditional rigid-link mechanisms, the synthesis methodology, which was successfully applied to the design of all presented devices, provides the conceptual framework to recreate the work and adapt it to new custom use cases. Furthermore, by presenting crucial design insights, this thesis will help to guide future work in the design of well-performing, close-fitting and comfortable compliant wearable assistive devices.

Samenvatting

Draagbare hulpmiddelen voor de bovenste extremiteiten worden gebruikt om armbewegingen van de gebruiker te ondersteunen. Ze kunnen het vermogen om handmatige taken uit te voeren herstellen of verbeteren. Een belangrijke klasse wordt gevormd door de zwaartekrachtcompenserende hulpmiddelen. Ze zijn ontworpen om het gewicht van de ledematen van de gebruiker en van opgepakte voorwerpen te dragen, en verminderen zo de inspanning die het kost om de armen te heffen of bepaalde houdingen vast te houden. De hulpmiddelen kunnen ingezet worden in fysiotherapie, voor hulp aan mensen met onvoldoende spierkracht, en ter ondersteuning van gezonde gebruikers bij het voorkomen van letsel en het verbeteren van het fysieke vermogen. De traditionele zwaartekrachtcompenserende hulpmiddelen zijn voornamelijk gebaseerd op stangenmechanismen bestaande uit scharnieren en stijve stangen, die een ondersteuningsstructuur vormen die het lichaam van de drager omsluit. Deze ondersteuningsstructuur, het archetype van exoskeletten, biedt diverse voordelen, zoals het kunnen gebruiken van krachtige actuatoren en het kunnen absorberen van zware lasten. De starre structuur kan echter ook hinderlijk zijn, doordat deze zowel het draagcomfort als het uiterlijk negatief beïnvloedt.

Om deze problemen aan te pakken beoogt dit proefschrift flexibiliteit en buigzaamheid als een integraal ontwerpparadigma op te nemen bij de totstandkoming van draagbare hulpmiddelen voor de bovenste extremiteiten. Daartoe wordt een holistische benadering nagestreefd, waarbij flexibele structuren meerdere subfuncties vervullen en zo gelijktijdig fungeren als veren voor energieopslag, als complexe overbrengingen, en als de dragende structuur. Deze functie-integratie wordt toegepast om de grootte en het gewicht te kunnen verminderen, en zo compacte ontwerpen mogelijk te maken die de drager comfortabele ondersteuning kunnen bieden en mogelijk verborgen kunnen worden onder de kleding. Middels de combinatie van deze benadering en het gebruik van numerieke multibody-modellen met globale optimalisatietechnieken, zijn elastische mechanismen voor zowel passieve als actieve toepassingen gesynthetiseerd.

Met betrekking tot de passieve toepassingen is er gebruik gemaakt van flexibele structuren om elastische mechanismen te bouwen die zwaartekrachtcompensatie bieden aan verschillende delen van de bovenste extremiteiten, terwijl een nauwe pasvorm en een hoge mate van biomechanische compatibiliteit worden nagestreefd. De synthesemethodologie is eerst ontwikkeld voor een mechanisme dat lateraal op de elleboog wordt aangebracht en de zwaartekracht op de onderarm compenseert. Vervolgens is de methode uitgebreid om de zwaartekracht op de bovenarm te compenseren met een mechanisme dat op de schouder wordt aangebracht en het bovenlichaam van de drager gedeeltelijk omsluit. In vergelijking met eerder onderzoek naar

zwaartekrachtcompensatie middels flexibele structuren zijn er verschillende fundamentele concepten blootgelegd, die essentieel blijken te zijn om de noodzakelijke prestaties te behalen en om de mechanismen geschikt te maken voor toepassing vlak tegen het lichaam. Zo wordt gebruik gemaakt van flexibele structuren met een dikte die varieert over de lengte, wat zowel de prestatie ten opzichte van grootte en gewicht verbetert, als ook de robuustheid van de balancering vergroot onder de gegeven ruimtelijke beperkingen. Daarnaast wordt middels aanpassingen aan de kinematische ondersteuningscondities van de flexibele structuren nog beter omgegaan met de ruimtelijke beperkingen, waardoor de afstand tot het lichaam aanzienlijk verminderd kan worden. Verder blijken deze aanpassingen ook van cruciaal belang te zijn bij het verlagen van ongewenste krachten en momenten op de interfaces, waardoor de noodzaak voor extra ondersteuningsstructuren aanzienlijk wordt verminderd.

In de context van actieve toepassingen, d.w.z. aangedreven, flexibele structuren, is een nieuw type buigactuator gebouwd. Door de combinatie van bladveren en McKibben-spijeren is deze actuator vanwege zijn geringe hoogte potentieel geschikt om onder kleding te worden toegepast. Voor deze actieve toepassing vormt de architectuur op basis van flexibele structuren een effectief middel om geschikt transmissiegedrag te bereiken met gebruik van kleine actuatorslaglengte in een beperkte ruimte.

Dit proefschrift laat zien dat ontwerpen op basis van flexibele structuren veelbelovende nieuwe oplossingen biedt ter verbetering van draagbare hulpmiddelen voor de bovenste extremiteiten, met een breed scala aan toepassingsgebieden. Naast concrete ontwerpen die praktische alternatieven bieden voor conventionele stangenmechanismen, biedt de synthesesmethodologie, die met succes is toegepast op het ontwerp van alle gepresenteerde apparaten, het conceptuele kader om nieuwe ontwerpen te creëren en aan nieuwe gebruikssituaties aan te passen. Bovendien zal dit proefschrift, door cruciale ontwerpinzichten te presenteren, bijdragen aan toekomstig onderzoek naar het ontwerp van goed presterende, nauwsluitende en comfortabele elastische hulpmiddelen.

Zusammenfassung

Tragbare Unterstützungssysteme für die oberen Extremitäten werden verwendet, um Armbewegungen des Trägers zu erleichtern. Dadurch können sie die Fähigkeit zur Ausführung manueller Tätigkeiten wiederherstellen oder verbessern. Schwerkraftkompensierende Unterstützungssysteme bilden hierbei eine prominente Gerätekategorie. Diese sind so konzipiert, dass sie das Gewicht der Gliedmaßen des Trägers und manipulierter Gegenstände tragen und somit den Kraftaufwand zum Anheben der Arme sowie zur Aufrechterhaltung bestimmter Körperhaltungen verringern. Sie werden zur Physiotherapie, zur Unterstützung von Menschen mit unzureichender Muskelkraft sowie zur Unterstützung gesunder Personen eingesetzt, um Verletzungen vorzubeugen oder ihre körperlichen Fähigkeiten zu verbessern. Herkömmliche tragbare Unterstützungssysteme zur Schwerkraftkompensation werden überwiegend als Starrkörpermechanismen konzipiert. Diese bestehen aus starren, über konventionelle Gelenke verbundenen Gliedern, die eine stabile Stützstruktur bilden, welche den Körper des Trägers umgibt. Diese Stützstruktur, die das namensgebende Merkmal von unterstützenden Exoskeletten ist, bietet mehrere Vorteile, beispielsweise für die Verwendung leistungsstarker Aktoren und für die Aufnahme schwerer Lasten. Sie kann aber auch von Nachteil sein, da sie häufig den Tragekomfort sowie das ästhetische Erscheinungsbild negativ beeinträchtigt.

Um diese Probleme anzugehen, hat sich diese Dissertation zum Ziel gesetzt Flexibilität und Nachgiebigkeit als integrale Paradigmen in die Konzeption und den Entwurf tragbarer Unterstützungssysteme für die oberen Extremitäten einzubeziehen. Zu diesem Zweck wird ein ganzheitlicher Ansatz verfolgt, bei dem flexible Strukturen mehrere Unterfunktionen des jeweiligen Gerätes integrieren und dadurch gleichzeitig als Federn zur Energiespeicherung, als komplexe Mechanismen zur Kraftübertragung sowie als tragende Stützstruktur dienen können. Diese Funktionsintegration wird genutzt, um Größe sowie Gewicht zu reduzieren und damit eng anliegende Bauformen zu ermöglichen, die in Kombination mit der inhärenten Nachgiebigkeit der flexiblen Struktur eine komfortable Unterstützung bieten und darüber hinaus potentiell unter der Kleidung verborgen werden können. Entsprechend dieses Ansatzes und unter Verwendung numerischer Mehrkörpersimulation in Verbindung mit globalen Optimierungstechniken wurden nachgiebige Mechanismen sowohl für passive als auch aktive Anwendungsfälle entworfen.

In Hinsicht auf passive Anwendungen wurden flexible Strukturen verwendet, um nachgiebige Mechanismen zu konstruieren, die einen Schwerkraftausgleich verschiedener Teile der oberen Extremitäten ermöglichen, wobei zugleich eine enge Passform sowie ein hohes Maß an biomechanischer Kompatibilität angestrebt wurden. Die Methoden und Verfahren zum Entwurf dieser Mechanismen wurden zunächst für

einen Mechanismus konzipiert und entwickelt, welcher seitlich am Ellenbogen angebracht wird und die Schwerkraft ausgleicht, welche auf den Unterarm einwirkt. Später wurden diese erweitert und weiterentwickelt, um einen Schwerkraftausgleich des Oberarmes zu erzielen, wobei der Mechanismus im Bereich der Schulter angewendet wird und den Oberkörper des Trägers teilweise umschließt. Im Vergleich zu früheren Forschungsarbeiten zum Schwerkraftausgleich auf Basis flexibler Strukturen wurden mehrere grundlegende Konzepte entdeckt, die sich als wesentlich erwiesen haben, um die erforderliche Leistungsfähigkeit zu erzielen, und um eine Anwendung in unmittelbarer Nähe zum Körper zu ermöglichen. Dies beinhaltet die Verwendung von flexiblen Elementen welche eine variable Dicke entlang ihrer Länge aufweisen, und somit die Leistung im Verhältnis zu Größe und Gewicht erhöhen sowie ein robustes Schwerkraftausgleichsverhalten ermöglichen, wenn zugleich Restriktionen hinsichtlich des verfügbaren räumlichen Volumens bestehen. Darüber hinaus ermöglicht die gezielte Gestaltung der kinematischen Stützbedingungen der flexiblen Elemente eine zusätzlich verbesserte Handhabung räumlicher Restriktionen, wodurch der Abstand zum Körper deutlich verringert werden kann. Diese Modifikationen erwiesen sich des Weiteren auch als entscheidender Vorteil zur Verringerung unerwünschter Kräfte und Momente an den Verbindungsstellen zum Körper, wodurch die Notwendigkeit von zusätzlichen tragenden Stützstrukturen in erheblichem Maße verringert wird.

Im Bereich aktiver Anwendungen, sprich durch Aktoren angetriebener nachgiebiger Komponenten, wurde eine neue Art von Biegeaktor geschaffen. Durch die Kombination aus Blattfederelementen mit McKibben-Muskeln weist dieser eine geringe Bauhöhe auf, welches potentiell den Einsatz unter Kleidung ermöglicht. Für diesen aktiven Anwendungsfall bietet die Verwendung einer nachgiebigen, auf flexiblen Strukturen basierenden Architektur ein wirksames Mittel, um ein geeignetes mechanisches Übertragungsverhalten zu erzielen, mit dem kleine Aktorstellwege auf engem Raum effektiv nutzbar gemacht werden können.

Insgesamt zeigt diese Dissertation, dass auf flexiblen Strukturen basierende Entwürfe vielversprechende neue Lösungen bieten, um tragbare Unterstützungssysteme für die oberen Extremitäten in verschiedenen Anwendungsbereichen zu verbessern. Abgesehen von konkreten Entwürfen, welche praktische Alternativen zu herkömmlichen Starrkörpermechanismen aufzeigen, bieten die Methoden und Verfahren welche beim Entwurf aller vorgestellten nachgiebigen Mechanismen erfolgreich zur Anwendung kamen, den konzeptionellen Rahmen, um diese Arbeit zu reproduzieren und entsprechend neuer benutzerdefinierter Anwendungsfälle anzupassen. Darüber hinaus tragen die grundlegenden Erkenntnisse, welche gesammelt wurden, dazu bei als Leitfaden für zukünftige Arbeiten zu dienen, welche sich mit dem Entwurf leistungsfähiger, eng anliegender und komfortabler Unterstützungssysteme auf Basis flexibler Strukturen auseinandersetzen.

Contents

1	Introduction	1
I	Passive Mechanisms	5
2	Gravity Balancing Flexure Springs for an Assistive Elbow Orthosis	7
2.1	Introduction	7
2.1.1	State of the Art	7
2.1.2	Research Approach	8
2.1.3	Scope	9
2.1.4	Structure	9
2.2	Synthesis	10
2.2.1	Topology	10
2.2.2	Task Definition	10
2.2.3	Parametrization	10
2.2.4	Discretization & Analysis	12
2.2.5	Shape Optimization	13
2.2.6	Computation	17
2.2.7	Nesting	18
2.2.8	Performance Metrics	19
2.3	Experiment	19
2.3.1	Test Specimens	19
2.3.2	Test Setup	20
2.3.3	Data Acquisition	21
2.4	Results	22
2.4.1	Computational Results	22
2.4.2	Experimental Results	23
2.5	Discussion	23
2.5.1	Synthesis Method	23
2.5.2	Experimental Validation	25
2.5.3	Application	28
2.6	Conclusions	29
2.7	Appendix	30
2.7.1	Tables	30
2.7.2	Supplementary Files	33

3 Gravity Balancing Flexure Spring Mechanisms for Shoulder Support	41
3.1 Introduction	41
3.2 Synthesis	43
3.2.1 Model Topology	43
3.2.2 Design Objectives	45
3.2.3 Application Requirements	46
3.2.4 Additional Specifications	46
3.2.5 Computational Model	47
3.2.6 Simulation	48
3.2.7 Parametrization	48
3.2.8 Optimization	48
3.2.9 Investigation Scheme	51
3.3 Experiment	52
3.4 Results	55
3.5 Discussion	68
3.6 Conclusions	70
3.7 Appendix	71
3.7.1 Tables	71
3.7.2 Supplementary Files	73
4 Wearable Implementations of Flexure Spring Mechanisms	89
4.1 SoftPro Wearable System	89
4.2 Wearable Shoulder Supports	91
4.2.1 Prototype 1	91
4.2.2 Prototype 2	93
4.3 Discussion	95
II Active Mechanisms	97
5 Compact McKibben Muscle Based Bending Actuator	99
5.1 Introduction	99
5.2 Methods	101
5.2.1 Application Requirements	101
5.2.2 Actuator Design	102
5.2.3 Materials	103
5.2.4 Parametrization	103
5.2.5 McKibben Muscle Model	104
5.2.6 Simulation	104
5.2.7 Optimization	106
5.2.8 Specimens	106
5.2.9 Test Setup	108
5.2.10 Experiment	109
5.3 Results	110

5.4	Discussion	112
5.5	Conclusions	115
5.6	Appendix	116
5.6.1	Supplementary Files	116
6	Discussion	119
6.1	Passive Mechanisms	119
6.1.1	Protrusion and Collision	119
6.1.2	Volume and Weight	121
6.1.3	Interface Forces and Moments	122
6.1.4	Future Work	122
6.2	Active Mechanisms	125
6.2.1	Buckling and Bending Stress	125
6.2.2	Stiffness and Elastic Energy	125
6.2.3	Actuation and Transmission	125
6.2.4	Future Work	126
6.3	General Remarks and Limitations	126
7	Conclusion	129
7.1	Outlook	131
	References	135
	List of publications	143
	Résumé	145
	Education	145
	Professional Experience	145
	Honors & Awards	146
	Acknowledgments	147

Introduction

Upper-limb wearable assistive devices are externally applied mechanical devices that provide physical support to the musculoskeletal system in order to facilitate functional arm movements. Thereby, they can restore or enhance the ability of the user to perform manual tasks. Aside from tremor suppression and assistance of specific joint motions, gravity compensation is one of their common main functions [66].

Gravity-compensating upper-limb supports help carrying the weight of the user's limbs and that of external loads which are manipulated by the user. From a clinical perspective, three major types can be distinguished: Rehabilitation aids supporting clinicians in administering physical therapy [39, 40], functional supports restoring the ability of people suffering from insufficient muscle strength to perform activities of daily living [14, 57, 66], and augmenting devices to prevent musculoskeletal disorders or enhance physical capabilities in demanding and repetitive work-related tasks [43].

From a technical perspective, two categories can be distinguished: end-effectors and orthoses [39, 66]. End-effectors have a non-anthropomorphic structure and attach at a single point to the upper limb through a serial linkage chain. Orthoses resemble the mechanical structure of the upper limb and have at least two attachment points to the body. Orthoses are also referred to as exoskeletons when featuring a rigid external structure and as exosuits when having a soft, often textile-like structure [68]. Both end-effectors and orthoses can be either body-mounted, i.e., entirely carried by the user, or mounted to an external entity, e.g., the floor, a table or a wheelchair.

Another distinction can be made between passive and active devices [39, 40, 66]. Passive devices do not use any external power. They work either by simply providing a supporting kinematic structure, e.g., in the form of a dynamic arm rest to facilitate planar movements parallel to the ground, or by storing energy internally, usually via springs, and releasing that energy in a predefined manner to support arm movements. Active devices use actuators, e.g., electric motors and pneumatic or hydraulic components, to actively support arm motions. The effort for the user can be reduced drastically, up to a degree at which the device executes the motion on its own while the user remains passive. However, active devices rely on external power which can only be temporarily stored internally, e.g., with batteries or pressure tanks, and precise control of the active components is necessary to provide adequate support and to avoid injury [69]. Passive and active components can also be combined to create devices that make use of both internal and external power [34, 40, 66].

Using passive components a concept called gravity balancing can be employed [35, 40, 57]. In an ideal gravity-balanced upper-limb support the potential energy of the combined mass of the wearer's limb, external loads and the device itself is perfectly exchanged with the internal energy storing elements as the arm moves in space, and no additional forces or moments are required to maintain static equilibrium.

1 However, to achieve wide-spread adoption of upper-limb assistive devices further technological advances are necessary that enable the design of devices which can be comfortably used in everyday settings [21, 40]. To this end, the current shortcomings in terms of functional and social acceptability need to be addressed [53]. With respect to the functional aspects, primarily the wearability and portability have to be improved in order to allow for extended periods of comfortable use [40, 68]. With regards to social considerations, reducing the conspicuity and improving the appearance are paramount to avoid social stigmatization [14, 40]. For this purpose, the ability to wear and thus conceal the device underneath clothing is currently considered the ‘gold standard’ [14, 53, 68, 69]. Consequently, reducing the size and weight of the components which make up most of the volume and mass are obvious steps towards higher acceptability. On top of that, specifically reducing protrusion from the body and making components applicable for close-to-body arrangements, which may result in contact with the wearer, are crucial aspects [14, 68].

The goal of this thesis is to explore mechanisms for upper-limb support that employ flexible elements that can be simultaneously used for internal energy storage, power transmission and as load-bearing structures. These elements, which are hereinafter referred to as flexures, are hence suitable for integrating different subfunctions of assistive orthoses, and thereby potentially allow for more space and energy-efficient designs. Furthermore, through their yielding nature, flexures can offer the intrinsic compliance to make resulting mechanisms applicable for close-to-body use.

Flexures, however, also pose several design challenges. As their function relies on elastic deformation, the maximum endurable stress of the flexure material becomes a limiting factor to the mechanism performance. This affects the achievable range of motion, amount of storable strain energy, energy-to-size and energy-to-weight ratios, as well as the lifetime of the device. Furthermore, when large deformations occur the motion path of such mechanisms can be hard to predict, as nonlinear effects due to the changes in geometric stiffness of the flexure elements become predominant.

To deal with these constraints and design suitable flexure mechanisms, numerical models and optimizations are developed. Using these tools, both passive and active flexure-based mechanisms are synthesized. In the context of passive devices, the objective is to find mechanism topologies and flexure shapes that provide gravity balancing while staying in close proximity to the body. This concept and the respective synthesis method are first established for a mechanism which is placed on the elbow joint, and then extended to be applicable for balancing at the shoulder joint. In the context of active devices, the objective is to build compact and concealable actuators. To this end, a novel approach is explored which combines flexures with soft pneumatic components in order to create a low-profile bending actuator.

In short, this thesis is concerned with the application of flexures to build compliant close-to-body upper-limb wearable assistive orthoses that offer:

1. Gravity balancing in passive orthoses
2. Concealed actuation in active orthoses

OUTLINE

This thesis is divided into two parts. The first addresses passive mechanisms for gravity balancing, while the second covers active mechanisms for concealed actuation. The main chapters of each part are written as self-contained scientific articles. Thus, each main chapter features its own introduction, discussion and conclusions. While this creates a certain degree of redundancy, it allows the reader to read and comprehend each chapter separately from the others. The present introductory chapter to this thesis serves to provide the overarching research context and to establish a relation between the individual contributions of each chapter. Likewise, the final discussion and conclusion chapters reflect upon the contents of this thesis in their entirety and aim to put them into the greater research context.

Appendices appear directly after each respective chapter in order to present them in context. Some appendices feature extensive supplementary materials. Aside from additional figures and tables, these also include animated graphics, movies and CAD files. Due to their nature, these cannot be appropriately portrayed within this document. However, links to the respective online resources are provided and previews are shown to help capture the gist of each respective material. All references are listed at the end of this thesis. This is done as to keep the list concise and to avoid the same reference from appearing under different labels.

Part I begins with Chapter 2. It addresses three distinct subgoals. The first is the development of a reliable synthesis method to obtain gravity-balancing flexure mechanisms. The second is the improvement of the energy density and specific energy to provide adequate support at a reasonable size and weight. The third is the handling of basic spatial constraints imposed by the kinematic structure of the anatomical joint to control the shape of the spring and allow for nested designs. These three subgoals are vital to use this technology and make it viable for portable use, and thus represent the first essential milestone of this research track. In line with these subgoals Chapter 2 describes the synthesis of gravity-balancing flexure springs for application in an assistive elbow orthosis. Thereby, the chapter lays the foundation for the methodology that is henceforth used for finding gravity-balancing flexure spring mechanisms. Each step of the synthesis and optimization process is presented in detail through figures and equations, and the results are validated in experiment. Aside from the fundamental synthesis process, the chapter establishes the concept of using non-prismatic flexures, specifically flexures with a variable thickness along their length to gain better control over the flexure shape, its deformation and the resulting motion. This enables adherence to basic spatial constraints, whereby the flexure can be arranged concentrically around the assisted joint without compromising the balancing quality. Given a lateral placement, this in turn allows for concentric nesting of the flexure springs as a strategy to significantly improve energy density. Furthermore, using a variable thickness generally resulted in a more uniform stress distribution along the flexure leading to additional gains in specific energy and energy density.

Chapter 3 expands on the methodology laid out in Chapter 2 and pursues three additional subgoals. The first two deal with advanced spatial constraints when considering the actual human upper-body geometry. These are: to avoid collision with the wearer, and to limit protrusion from the wearer. These two subgoals are crucial to make devices that are viable for close-to-body use and to reduce conspicuity. The third additional subgoal aims to minimize the reaction forces and moments between mechanism and wearer. This subgoal is key to break the dependence on a dedicated load-bearing structure, and thus to give this technology a distinct advantage over traditional devices based on rigid-link mechanisms. Accordingly, Chapter 3 describes the synthesis of gravity-balancing flexure spring mechanisms for shoulder support applications. In this new use case the flexure is no longer laterally placed onto the assisted joint, but partially encloses the wearer's upper body. An extensive investigation into different mechanism topologies is conducted by varying the kinematic support conditions of the flexure element. The main contribution of this chapter, aside from its case-specific additions and general improvements to the synthesis method, is to provide a broad overview over the feasible mechanism topologies and their suitability for the proposed use case. To that effect, the synthesized mechanisms are categorized based on features pertaining to their topology and function principles. Two promising designs are chosen for further investigation and used to experimentally validate the results. It is found that the addition of hinges and sliders, with and without an associated spring stiffness, can be instrumental for allowing close-to-body arrangements with less protrusion, for lowering the reaction forces and moments at the interfaces, as well as for improving the performance with respect to size and weight.

Chapter 4 which concludes the first part briefly presents practical wearable implementations of the flexure-based technologies that originated from Chapter 2 and Chapter 3. It mainly serves an illustrative purpose and does not adhere to the typical article format of the main chapters.

Part II, Chapter 5, follows a more exploratory approach and aims to reveal potential synergies of combining soft actuation technologies with flexures. As in Chapter 3, a mechanism for providing shoulder support is presented. The active mechanism features a structure in which miniaturized McKibben muscles are combined with flexures to create a compact bending actuator for close-to-body application in wearable assistive robotic orthoses. The flexures are used to leverage the high-force low-displacement properties of the McKibben muscles towards a large rotational range of motion, and to decouple the exerted tension forces from the user. The chapter presents the actuator topology, the applied parameter optimization and the experimental evaluation of several physical test specimens. The results show that this flexure-based semi-soft actuator has good potential for offering a concealable means of actuation, since it allows for close-to-body use and is potentially wearable underneath clothing, as is illustrated by a proof-of-concept prototype.

Finally, Chapter 6 presents a comprehensive discussion and Chapter 7 finishes with the conclusions of this thesis.

Part I

Passive Mechanisms

Gravity Balancing Flexure Springs for an Assistive Elbow Orthosis

Abstract In this chapter a flexure spring based gravity compensation device is proposed which provides assistance to lift the forearm. Three different spring designs are obtained and evaluated. The synthesis method to obtain these is explained in detail and an experimental evaluation validates the desired gravity balancing properties. It is found that in comparison to a flexure spring with constant thickness, a variable thickness distribution along the spring leads to a drastic reduction of its width, which amounts to 81 % in the presented case, and offers an energy to weight ratio that is 94 % higher. Employing a nested spring design further increases the storable elastic energy of the variable thickness design by 145 % through utilization of the otherwise unused space within the original spring envelope. A proof-of-concept prototype is built to illustrate a practical implementation. The presented synthesis method provides a tool to obtain gravity balancing flexure springs that offer a promising solution for the design of assistive devices which aim to be both wearable and inconspicuous.

2.1 INTRODUCTION

Gravity balancing supports for the upper limb are used to facilitate functional movements of the arm. The main group associated with the use of gravity balancing arm supports are people suffering from neuromuscular disorders. Due to muscular weakness their ability to execute activities of daily living (ADLs) is severely impeded which leads to a large dependency on external help in the form of caregivers. Furthermore, social participation is often heavily affected. Assistive devices using gravity balancing principles can play a key role in restoring the ability to execute ADLs independently and enhancing social participation [14, 57].

2.1.1 State of the Art

Within the domain of assistive devices two categories can be distinguished: end-effectors and exoskeletons. These can be further subdivided by method of actuation [39, 66]. While most of the commercially available arm supports are passive end-effector devices [66], the benefits of wearable exoskeletons are evident, as they allow for close alignment to the body, offer a more natural range of motion, allow for independent balancing of the upper arm and forearm, and enable increased mobility for both ambulatory users as well as wheelchair-bound users [14, 15, 23, 66].

A significant growth of upper-limb exoskeletons occurred in the last decades [21]. Yet, remarkably, the majority of upper-limb exoskeletons have never been used in daily life by their intended target populations [66]. Numerous reasons can be found to explain why potential target groups refrain from using upper-limb exoskeletons outside of clinical settings. In terms of system acceptability, these can be classified as a lack of either functional acceptability or social acceptability [53]. In order to achieve high functionality and biomechanical compatibility a trend towards an ever increasing technical complexity can be observed [21]. However, an increase in functionality does not necessarily correspond to an improved usability or usefulness for the user. As is generally observed by the academic community, the cost-benefit ratio associated with the use of current assistive devices is in most cases unfavorable [14, 21, 39, 53, 57, 66]. The most critical issue, as indicated by some authors, is the lack of social acceptability due to appearance. Thus arose the demand to make future devices inconspicuous, for example, by making them wearable underneath clothing [14, 53].

In the light of these considerations and given the present state-of-the-art of actuation and energy storage technology, it appears evident that the most promising solutions are currently to be found in passive wearable exoskeletons with spring-based gravity compensation. The number of devices which are designed to assist ADLs and feature these attributes, however, is very small. To the author's knowledge only four such devices exist at this point of time. The WREX [23, 57] and the A-Gear [35] are devices that support both upper arm and forearm against gravity. The SpringWear [7, 8] applies gravity compensation to the upper arm. The Wilmer elbow orthosis [52] supports the forearm.

2.1.2 Research Approach

With the exception of the Wilmer elbow orthosis, which is wearable underneath clothing, critique towards the above mentioned devices mainly concerns their inadequate weight, size and conspicuity. Common features of these devices are the use of rigid-link mechanisms and rubber bands, which are used to store potential energy. While rubber bands, loaded in tension, offer a very high specific energy, they rely on a rigid structure to which they attach. Without this structure the spring forces would induce inadmissible levels of shear to the skin.

In the broader field of robotics many spring-based gravity balancing mechanisms have been devised. However, in most cases these also use linear extension and compression springs in combination with rigid-link mechanisms [4].

In order to build energy storing elements, i.e., springs, which do not induce high shear forces at their attachment points, this study intends to explore the utilization of large stroke bending deformation for storing elastic strain energy. The hypothesis is that by doing so it will be possible to reduce the size of the frame and ultimately to refrain from using rigid linkages entirely. This aims to address the problems of the aforementioned assistive devices regarding their weight, size and conspicuity.

2.1.3 Scope

In the scope of this study an elbow orthosis is designed, which features a flexure spring that undergoes large deflections and balances the forearm against gravity when the upper arm maintains a low elevation angle. In previous work by Cheng *et al.* [9, 10] it was shown that such flexure springs can be synthesized and used to balance a planar linkage, representing the upper arm and forearm. Similar work outside the scope of assistive devices was conducted by Radaelli and Herder [54, 55, 56], where beam shapes have been synthesized that are used for general gravity balancing purposes. However, in all cases the resulting spring designs turn out to be large in respect to the amount of torque or force which they can deliver.

Therefore, as the first step towards the ultimate goal, this study does not yet attempt to minimize the shear forces exerted by the spring, but concentrates on finding ways to increase the specific energy and energy density of the spring, as these are fundamental key factors to make the use of such elements feasible in wearable devices.

The core of this study is the synthesis and experimental evaluation of three spring designs. The first spring, though different in topology and shape, is comparable to the design shown by Cheng *et al.* [10], featuring a constant cross-section. It is consequently suffering from similar shortcomings. The synthesis method is extended, however, to additionally optimize the thickness distribution along the spring. Thereby, a second design is obtained which features major improvements in terms of its size to energy ratio. Furthermore, it enables concentric nesting of additional spring elements. This leads to the third design in which, by utilizing the otherwise unused space within the original spring envelope, the energy density is further increased.

These two novel approaches in the field – variable thickness distribution and concentric nesting – provide the theoretical framework to build gravity balancing flexure springs which can be smaller and lighter than the above mentioned comparable predecessors.

2.1.4 Structure

The main focus of this chapter is on conveying the synthesis method by which the three spring designs are obtained. This is elaborated on in detail in the *Synthesis* section which follows this introduction. In order to verify the presented synthesis method a technical validation is conducted in a test bench environment, described in the *Experiment* section. The outcomes of both synthesis and experiment are presented in the *Results* section and are critically reflected upon in the *Discussion* section. In addition, an early proof-of-concept prototype is shown to illustrate the practical applicability. In the *Conclusions* section the contents of this chapter are concisely recapitulated and its contributions are put into the broader research context.

2.2 SYNTHESIS

In this section the synthesis method is described by which desired beam geometries and their respective dimensions are obtained.

2.2.1 Topology

It is assumed that the forearm can be represented by a point mass m on a lever with length L rotating around a fixed point P representing the elbow joint. In order to statically balance this system a moment has to be generated that will counteract the moment generated by the point mass under the influence of gravity. To this end, a compliant curved beam which acts as a spring is clamped to the forearm link on one end and to the fixed world, representing the upper arm, on the other end. An idealized physical model topology can be seen in Figure 2.1.

2.2.2 Task Definition

An angular displacement of the lever in the range of $\theta = [0 \dots \pi]$ rad is investigated, as this fully covers the the range of motion of the human elbow joint. Ideally, the energy is exchanged reversibly between the spring and the mass, such that the total energy of the system remains constant for any angle θ . Since the potential energy of the mass is maximum at $\theta = 0$ and the gravity forces are supported by the rigid linkage in this position, it is chosen as the initial position such that no pre-stress is required.

The goal is to achieve mechanical equilibrium for the entire deflection range of θ . As a sufficient condition in this case, only the moments around the pivot P are observed. The moment generated by the mass under the influence of gravity is

$$M_g = mgL\sin(\theta) \quad (2.1)$$

where M_g is the gravity moment and g is the gravitational acceleration constant. Consequently, the balancing moment M_b is the additive inverse of M_g , thus

$$M_b = -M_g = -mgL\sin(\theta) \quad (2.2)$$

2.2.3 Parametrization

The spring is considered mathematically as a beam. In order to optimize the beam, its geometry is described by an appropriate vector of design parameters. The parameter vector \mathbf{x} is divided into three parts, of which the first two parts describe the shape of the neutral beam axis, and the third part determines the thickness distribution along the beam.

To obtain the shape of the neutral axis of the beam, a control polygon formed by an array of control points is interpolated using the piecewise biarc Hermite spline interpolation function `rscvn()` from the MATLAB Curve Fitting Toolbox.

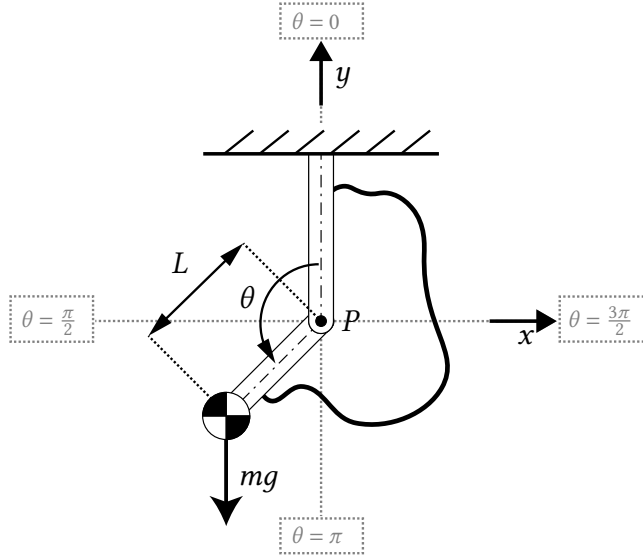


Figure 2.1: Model topology at position $\theta = \frac{3\pi}{4}$. The bold black solid line represents an arbitrary compliant beam. The black dashed-dotted lines depict the linkage axes, the gray dotted lines the coordinate axes with the respective angles indicated at their ends. The bold black dot shows the location of pivot P coinciding with the origin of the Cartesian space.

The start-point (x_0, y_0) and end-point (x_n, y_n) of the control polygon are directly described in terms of Cartesian coordinates. Since in its initial configuration both endpoints are defined to coincide with the vertical coordinate axis at $x = 0$, only the y-components $[y_0, y_n]$ are explicitly specified as variables in the parameter vector \mathbf{x} .

The positions of all intermediate points are determined using a linkage chain formulation as proposed by Radaelli and Herder [54]. To this end, the lengths l and relative angles φ of all links in the linkage chain are stored in the second part of the parameter vector \mathbf{x} . As described by Radaelli and Herder [54, 56], this formulation enables efficient control of the distances between control points and of the relative angles between links through the use of bounds during the optimization. The parametrization of the neutral axis is depicted in Figure 2.2.

In order to prescribe a stiffness variation along the beam an array of two or more thickness modifiers tm is appended to the parameter vector \mathbf{x} . This yields the complete parameter vector of the form

$$\mathbf{x} = [[y_0, y_n], [l_1, \varphi_1, \dots, l_n, \varphi_n], [tm_1, \dots, tm_n]] \quad (2.3)$$

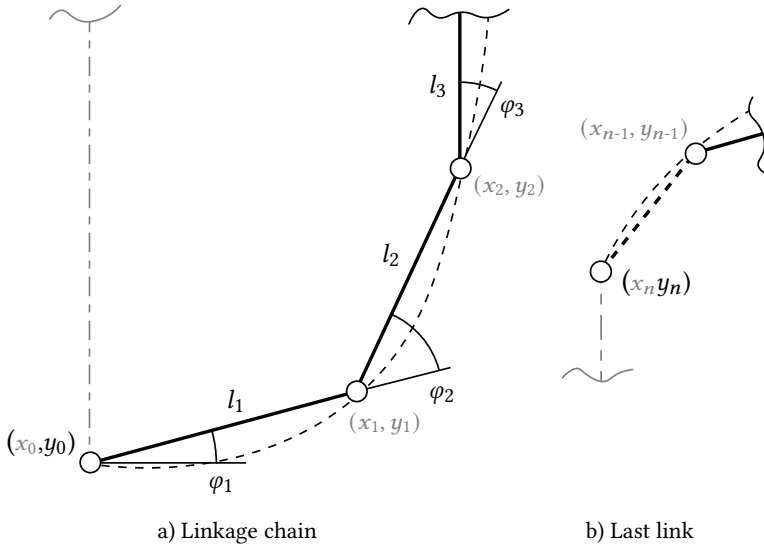


Figure 2.2: Parametrization of the neutral axis through linkage chain formulation. Black values indicate explicit parameters. Grey values show the respective implicit coordinates. The solid line depicts the control polygon, the weak dashed line the Hermite spline interpolation, the bold dashed line the last link of the control polygon which is not part of the linkage chain and the gray dashed-dotted line the vertical axis at $x = 0$.

2.2.4 Discretization & Analysis

To evaluate design parameter sets defined by \mathbf{x} during the optimization routine numerical analyses are conducted using the flexible multibody dynamics software package SPACAR [29]. The mechanism is modeled using finite planar beam elements. Levers are modeled as rigid, massless beams. An extension of the two-node beam element is used, to model the flexible, pre-curved beams [44].

Bending deformations of a single beam element in SPACAR are modeled using a cubic polynomial shape function that interpolates between its two nodes. Furthermore, each beam element possesses constant cross-sectional properties. Thus, in order to model a complex-shaped beam with changing thickness it has to be discretized by multiple beam elements.

The nodal coordinates of these beam elements are obtained by linear subdivision of the neutral axis spline function according to its basic interval $\Psi = [\psi_0 = 0 \dots \psi_{max}]$ (see Figure 2.3-a). However, the value of ψ is not directly proportional to the arc length of the spline. As a result the beam element nodes are generally not evenly distributed along the neutral axis.

The thickness modifiers tm are linearly interpolated across these nodes, to obtain a refined thickness modifier tm_r for each node (see Figure 2.3-b). The median of two refined thickness modifiers tm_r at both end-nodes of a beam element determines the discretized thickness modifier tm_d for that element.

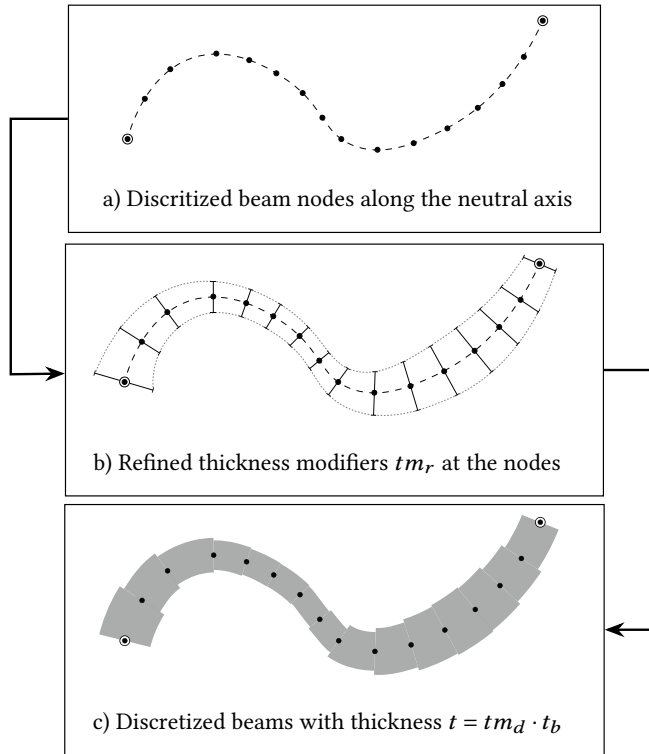


Figure 2.3: Three-step model discretization procedure.

To obtain the corresponding actual thickness t of that beam element, the dimensionless thickness modifier tm_d is multiplied with a thickness base value t_b , which provides the absolute scale (see Figure 2.3-c).

2.2.5 Shape Optimization

The goal of the shape optimization is to find an ideal beam shape and stiffness distribution along the beam which leads to optimal gravity balancing behavior while observing multiple constraints. The Genetic Algorithm function $ga()$ from the MATLAB Global Optimization Toolbox is used for solving the minimization problem.

To obtain an optimal parameter set \mathbf{x}^* a minimization problem for the cost function $f(\mathbf{x})$ is considered. The function $f(\mathbf{x})$ comprises the objective δ and a set of penalties \mathbf{p} , which are multiplied by a penalty coefficient k_p .

$$f(\mathbf{x}) = \delta + k_p \mathbf{p} \quad (2.4)$$

The problem is subject to lower bounds \mathbf{b}_l and upper bounds \mathbf{b}_u . Furthermore, linear inequality constraints \mathbf{c}_l and non-linear inequality constraints \mathbf{c}_{nl} apply.

The objective is to find a beam design that creates a negative sine-shaped moment curve as the lever travels from $\theta = 0$ to $\theta = \pi$ rad. Assuming isotropic material properties, the shape of that moment curve is solely determined by the dimensionless beam shape and the relative stiffness distribution, as described by \mathbf{x} . Therefore, the other design variables: actual in-plane size (i.e., scale), actual beam thickness, beam width and material properties can be determined separately and are chosen arbitrarily for the shape optimization. These remaining variables are obtained in a subsequent dimensioning step, described in subsection 2.2.6, that determines a mechanical feasible design based on desired metrics, such as the desired absolute moment amplitude and in-plane size, while considering maximum and minimum values of the beam thickness and beam width, respectively. This two-step procedure is used to reduce the amount of design variables that are optimized simultaneously, in order to minimize the design space for the computationally demanding shape optimization.

The discrete moment curve \dot{M} generated by a certain spring design is determined in simulation and normalized by its absolute maximum amplitude $|\dot{M}|_{max}$. The objective δ is defined as the mean absolute error between the value of this normalized moment response and the value of the ideal moment characteristic $-\sin(\theta)$ at each angle θ_k .

$$\delta = \sum_{k=1}^{\bar{n}} \frac{|\dot{M}_k / |\dot{M}|_{max} + \sin(\theta_k)|}{\bar{n}} \quad (2.5)$$

where k is a discrete load step and \bar{n} is the total number of load steps at which the objective is evaluated.

Two linear constraints are used to limit both the sum of the lengths of the linkage chain links l and the relative angles φ , avoiding an excessive beam length and loops. The maximum permitted total length and angle are represented by \mathbb{L}_{max} and Φ_{max} , respectively.

$$\mathbf{c}_{l(1)} = \left| \sum_{i=1}^n l_i \right| - \mathbb{L}_{max} \quad (2.6)$$

$$\mathbf{c}_{l(2)} = \left| \sum_{i=1}^n \varphi_i \right| - \Phi_{max} \quad (2.7)$$

Seven non-linear constraints are used of which one is treated as an option. The first non-linear constraint limits the distance between the end of the linkage chain (x_{n-1}, y_{n-1}) and the end-node of the control polygon (x_n, y_n) . The maximum distance \mathbb{l}_{max} is equal to the upper boundary \mathbf{b}_{ul} of the link lengths l .

$$\mathbf{c}_{nl(1)} = \sqrt{(x_n - x_{n-1})^2 + (y_n - y_{n-1})^2} - \mathbb{l}_{max} \quad (2.8)$$

The remaining non-linear constraint checks are carried out at discrete points (\hat{x}_i, \hat{y}_i) , $i \in [1, \dots, \hat{n}]$ on the beam neutral axis, given by the spline interpolation.

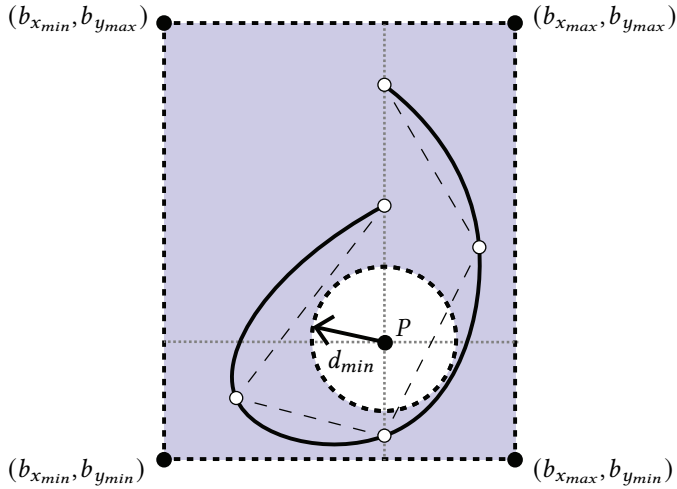


Figure 2.4: Spatial constraints of the neutral axis spline. The bold black dashed lines show the borders of the feasible region, which is indicated by the shaded area. The solid black line shows the neutral axis spline. The spline and its control points must lie within the feasible region. The control polygon of the spline, drawn as the weak dashed lines, can pass through infeasible regions.

A feasible region is defined by a rectangle with lower bounds $[b_{x_{min}}, b_{y_{min}}]$ and upper bounds $[b_{x_{max}}, b_{y_{max}}]$.

$$\mathbf{c}_{nl(2,3)} = [b_{x_{min}} - \hat{x}_i, \quad b_{y_{min}} - \hat{y}_i] \quad (2.9)$$

$$\mathbf{c}_{nl(4,5)} = [\hat{x}_i - b_{x_{max}}, \quad \hat{y}_i - b_{y_{max}}] \quad (2.10)$$

Thereby, mainly the position of the neutral axis in relation to the rotary joint is controlled. For an overview of the spatial constraints refer to Figure 2.4.

To detect self-intersections of the neutral axis in the undeformed state an iterative procedure is conducted. Two line segments L_1 and L_2 are considered. L_1 spans the distance between (\hat{x}_i, \hat{y}_i) and $(\hat{x}_{i+1}, \hat{y}_{i+1})$, while L_2 spans the distance between (\hat{x}_j, \hat{y}_j) and $(\hat{x}_{j+1}, \hat{y}_{j+1})$. For each line segment L_1 in the interval $i = [1 \dots \hat{n} - 2]$ potential intersections with all consecutive line segments L_2 in the interval $j = [i + 1 \dots \hat{n} - 1]$ are determined. First the x -component of the intersection point $I_{(i,j)}$ of the two straight lines collinear with the line segments L_1 and L_2 , respectively, are determined.

$$I_{x(i,j)} = \frac{a - b}{c - d}, \quad (2.11)$$

$$\begin{aligned} a &= (\hat{x}_i \hat{y}_{i+1} - \hat{y}_i \hat{x}_{i+1})(\hat{x}_j - \hat{x}_{j+1}), \\ b &= (\hat{x}_i - \hat{x}_{i+1})(\hat{x}_j \hat{y}_{j+1} - \hat{y}_j \hat{x}_{j+1}), \\ c &= (\hat{x}_i - \hat{x}_{i+1})(\hat{y}_j - \hat{y}_{j+1}), \\ d &= (\hat{y}_i - \hat{y}_{i+1})(\hat{x}_j - \hat{x}_{j+1}) \end{aligned}$$

Subsequently, a logic operation determines whether the intersection lies within both intervals L_1 and L_2 . The result is stored in the matrix $n_{\times(i,j)}$.

$$n_{\times(i,j)} = \begin{cases} 1, & \text{if } e \wedge f \leq 0 \\ 0, & \text{else} \end{cases} \quad (2.12)$$

$$e = (I_{x(i,j)} - \hat{x}_i)(I_{x(i,j)} - \hat{x}_{i+1}),$$

$$f = (I_{x(i,j)} - \hat{x}_j)(I_{x(i,j)} - \hat{x}_{j+1})$$

Since the segments are linear it is sufficient to only consider the x -components. The sum of all elements in $n_{\times(i,j)}$ yields the total number of intersections n_{\times} . As self-intersections are not admissible, the limit value is zero. Thus, the respective constraint is

$$c_{nl(6)} = n_{\times} = \sum_{i=1}^{\hat{n}-2} \sum_{j=i+1}^{\hat{n}-1} n_{\times(i,j)} \quad (2.13)$$

The last nonlinear constraint is optional. It ensures, that the neutral axis encloses the rotary pivot P while maintaining a minimum distance d_{min} . First, the MATLAB function *inpolygon()* is used to determine, if the polygon of all points (\hat{x}_i, \hat{y}_i) , $i = [1, \dots, \hat{n}] \rightarrow 1$ encloses the rotary pivot P at $(0, 0)$. The result is stored in the Boolean variable Ξ , where $\Xi = 1$ indicates the joint being inside and $\Xi = 0$ it being outside the polygon. Next, the minimum distance between the polygon vertices and the pivot P is determined and depending on Ξ subtracted, respectively added to d_{min} . Thus,

$$c_{nl(7)} = \begin{cases} d_{min} + \min \sqrt{\hat{x}_i^2 + \hat{y}_i^2}, & \text{if } \Xi = 0 \\ d_{min} - \min \sqrt{\hat{x}_i^2 + \hat{y}_i^2}, & \text{if } \Xi = 1 \end{cases} \quad (2.14)$$

Two soft constraints are integrated into the cost function $f(\mathbf{x})$ as penalties \mathbf{p} , which are multiplied by a large penalty coefficient $k_p = 10^5$ and added to the objective δ . They are used to avoid dedicated runs of the computationally expensive SPACAR simulation for the evaluation of non-linear constraints.

The first of these soft constraints limits the self-intersections for the entire deflection range. Analog to the prior introduced self-intersection constraint $c_{nl(6)}$ for the undeformed state, a self-intersection test is performed at every load step k . In this case, the evaluated line segments correspond to the positions of the beam element nodes given by the SPACAR simulation. The sum of all self-intersections for all load steps $k = [1 \dots \bar{n}]$ yields the score \bar{n}_{\times} , which shall equal zero. The respective penalty is

$$p_{(1)} = \bar{n}_{\times} = \sum_{k=1}^{\bar{n}} \sum_{i=1}^{\hat{n}-2} \sum_{j=i+1}^{\hat{n}-1} n_{\times(i,j,k)} \quad (2.15)$$

The second soft constraint limits relative stress concentrations along the beam, which are expressed by the ratio between the maximum stress in the most stressed beam element and the average maximum stress that each beam element endures during one load cycle.

Each planar beam element has three discrete deformation modes e , which are each associated with a respective generalized stress σ . These deformation modes are elongation (e_1, σ_1) and bending $(e_2, \sigma_2), (e_3, \sigma_3)$ at each end-node, respectively.

The penalty $\mathbf{p}_{(2)}$ is obtained by first separately evaluating the maximum absolute generalized stress per deformation mode which each beam element i endures throughout all load steps k .

$$\sigma_{(e,i)_{max}} = \max |\sigma_{(e,i,k)}| \quad \forall \quad k \in [1, \dots, \bar{n}] \quad (2.16)$$

Then, the maximum stress per deformation mode, for all load steps is determined as

$$\sigma_{(e)_{max}} = \max |\sigma_{(e,i)_{max}}| \quad \forall \quad i \in [1, \dots, \hat{n}] \quad (2.17)$$

Analogously, the mean per deformation mode is

$$\sigma_{(e)_{mean}} = \sum_{i=1}^{\hat{n}} \frac{|\sigma_{(e,i)_{max}}|}{\hat{n}} \quad (2.18)$$

The ratio between the maximum and the mean for each deformation mode is computed, and the highest ratio out of these yields the value λ .

$$\lambda = \max \frac{\sigma_{(e)_{max}}}{\sigma_{(e)_{mean}}} \quad \forall \quad e \in [e_1, e_2, e_3] \quad (2.19)$$

If λ exceeds a predefined limit λ_{max} , then the difference yields Λ which equals the penalty $\mathbf{p}_{(2)}$.

$$\mathbf{p}_{(2)} = \Lambda = \begin{cases} \lambda - \lambda_{max} & \text{if } \lambda - \lambda_{max} > 0 \\ 0 & \text{if } \lambda - \lambda_{max} \leq 0 \end{cases} \quad (2.20)$$

2.2.6 Computation

Optimizations are conducted according to subsection 2.2.5 using two sets of optimization parameters, **Set A** and **Set B**, that define the bounds \mathbf{b} , constraints \mathbf{c} , and penalties \mathbf{p} . Both parameter sets are shown in Table 2.3 in the Appendix. The key difference between the two sets is to be found in tm_{min} , the lower bound of the thickness modifiers tm , and the specification of d_{min} , the minimum distance to the pivot. When applying **Set A** the beam is optimized using a constant thickness and without constraining the beam to enclose the pivot P . In contrast, when applying **Set B** the beam thickness can vary between 0.2 and 1 times the thickness base value t_b and it is constrained to enclose P by enforcing $\mathbf{c}_{nl(7)}$.

Subsequent to the shape optimization, a dimensioning procedure is conducted for each set of optimization parameters, respectively. First, a desired footprint size of the spring is defined and the corresponding ideal beam thickness base value t_b^* is determined. The desired footprint is described by a bounding box with prescribed height h_s and width w_s . A uniform scale factor s is determined such that the neutral line of the beam coincides tangentially with the inside of the bounding box. For this given in-plane size of the spring, the optimal beam base thickness t_b^* is defined as the value of t_b which, when multiplied with the discretized thickness modifiers tm_d to obtain the actual thickness t along the beam, results in a maximum simulated von Mises stress σ_{mises} that equals a target stress $\dot{\sigma}$, defined as the tensile strength σ_t divided by a factor of safety FOS . The objective η for this unconstrained optimization problem is

$$\eta = |\sigma_{mises} - \dot{\sigma}|, \quad \dot{\sigma} = \frac{\sigma_t}{FOS} \quad (2.21)$$

The problem is solved with the MATLAB `fminbnd()` command, using the dimensioning parameters shown in Appendix Table 2.4. Next, the ideal out-of-plane beam width w_b^* is determined, which is defined as the value of w_b at which the amplitude of the moment curve a matches the requested amplitude a^* . Since the moment amplitude is linearly proportional to the out-of-plane width w_b , the optimal value w_b^* can be analytically determined from any out-of-plane width \tilde{w}_b and its corresponding moment amplitude \tilde{a} through

$$w_b^* = \tilde{w}_b \frac{a^*}{\tilde{a}} \quad (2.22)$$

The dimensioning is done for the material properties of PA 2200, as provided by the manufacturer data sheets [17, 49]. They can be found in Appendix Table 2.5. Furthermore, limitations of the laser sintering process are considered. For both the dimensioning procedure and the numerical evaluation, the weight of the beam itself is taken into account.

2.2.7 Nesting

As the variable thickness beam (**Set B**) encloses the pivot P , it allows the creation of the spring design **Set C** in which multiple scaled versions of the same beam design are nested in an array of parallel beams arranged concentrically around the pivot P . Each beam in this compound structure shares the same shape parameters as the variable thickness beam defined by **Set B**. However, for each beam the thickness base value t_b is determined separately according to its scale factor s . For comparability, the dimensions of the outer beam are chosen to be identical with the original variable thickness beam and the width of all beams is chosen to be equal. The minimum distance between the beams is set to approximately 0.8 mm, in order to avoid fusing of the beams during laser sintering, and the smallest beam is determined by the minimum manufacturable beam thickness of 0.4 mm.

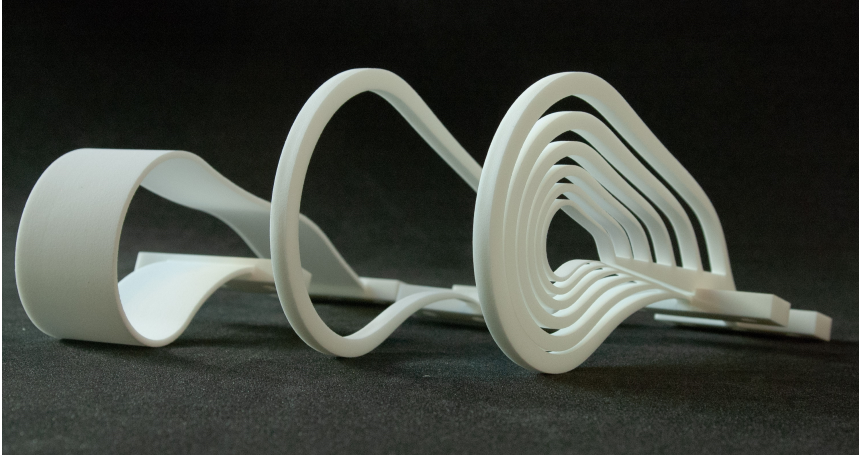


Figure 2.5: Specimens, from left to right: **Set A, Set B, Set C**

2.2.8 Performance Metrics

Gravity balancing quality, expressed in the objective δ , is considered to be the main performance metric in the scope of this study, as it represents the fundamental function of the spring. However, for further comparison of the different spring designs secondary performance metrics are considered. These are the specific strain energy ε with respect to the fully deflected state, as well as the energy density ω with respect to the occupied bounding box volume during deflection V_{Δ} .

The total strain energy U that is stored in the spring in its fully deflected state is determined from the respective SPACAR simulation. The mass m is derived from CAD models. Division of U by m yields the specific energy ε of the spring, which can be used as a measure of the material utilization efficiency. The bounding box volume of the cumulative volume V_{Δ} that is occupied by the spring during a full deflection cycle is determined by multiplying the beam width w_b with the corresponding envelope area A_{Δ} . The latter is obtained from generating the convex hull of the point cloud formed by all beam element nodes, that are superimposed for all load steps of the SPACAR simulation. Division of U by V_{Δ} yields the energy density ω , which can be used as a measure of the space utilization efficiency.

2.3 EXPERIMENT

2.3.1 Test Specimens

Specimens with smooth surfaces are obtained through further beam refinement. This is done in order to avoid stress concentrations at the transition between two discrete thicknesses. The refinement process is equivalent to increasing the number of beam elements in the simulation. Convergence studies showed that numerical results only change marginally when using more than the 50 beam elements, which are used for the dimensioning and for generating the computational results.

The physical test specimens are modeled such that the beam elements transition into large bodies (74x20x10 mm) at each end, which are used to mount the specimens onto the test bench. For the nested spring design, extensions from these bodies connect to all parallel beams. The test specimens are made via plastic laser sintering on a EOS Formiga P110 using PA 2200, which is based on a polyamide 12.

Refer to Figure 2.5 for a comparison of the specimens and to Figure 2.6 to see the fixation to the test bench.

2.3.2 Test Setup

The experimental test setup, which is used to validate the simulation results is shown in Figure 2.6. The frame is built using 40x40 mm aluminum profiles and 3 mm steel plate, mounted on a 25 mm thick aluminum optical plate. The profiles form a box-shaped frame, which is closed at the top by two traverse profiles and supported on the left side by two triangular sections. The box frame is closed to the left and the right by steel plates. Between the two steel plates a rotating lever made from 10 mm thick aluminum is supported on each side by a roller bearing mounted in the respective steel plate, held in place by housings made from polylactide (PLA) polymer. Above the rotational axis a transverse beam connects both plates and serves as a rigid interface to the frame.

The test specimens are clamped to the lever on one side and to the traverse beam to the other side, using M6 screws. A short lever extension made from PLA is used to compensate for the geometry changes between specimens. To the left side, the lever is connected via a rigid coupling to a YUMO E6B2-CWZ3E digital quadrature encoder. The encoder is mounted onto the steel plate using a PLA mount. To the right side, the lever connects to a timing pulley via a bellows coupling. The pulley is again supported by two roller bearings mounted to two opposing steel plates, using PLA housings. The plates are connected to each other by bolts that run through steel tubes that act as spacers. Both plates are fixed to the optical plate via aluminum profiles.

A timing belt runs over the pulley, from which it extends horizontally to one side and vertically downward to the other side. At the horizontal end the belt is connected to a ME-Meßsysteme KM10z load cell. The load cell is mounted at its other side to a LinMot P01-23x160H-HP linear motor for actuation. The linear motor is fixed to a steel plate, which connects to the box shaped frame via aluminum profiles. At the downward end of the belt a counter mass is attached, which provides the required belt tension for two-way actuation.

Electrically, the linear motor is connected to a LinMot B1100-VF-HC linear motor driver, which is connected to a PC via the RS-232 serial port. The force sensor is connected to a ME-Meßsysteme GSV-11H 010-5/20/2 measuring amplifier. The amplifier and the digital encoder both connect to a National Instruments BNC-2110 adapter, that sends the signals to a National Instruments PCI-6221 multifunction I/O device. The linear motor is controlled with command tables using the proprietary software LinMot-Talk. Sensor read-outs are performed using Simulink Real-Time.

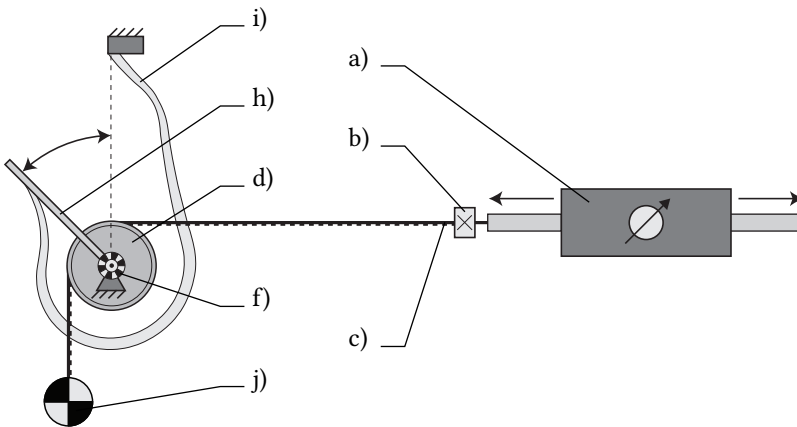
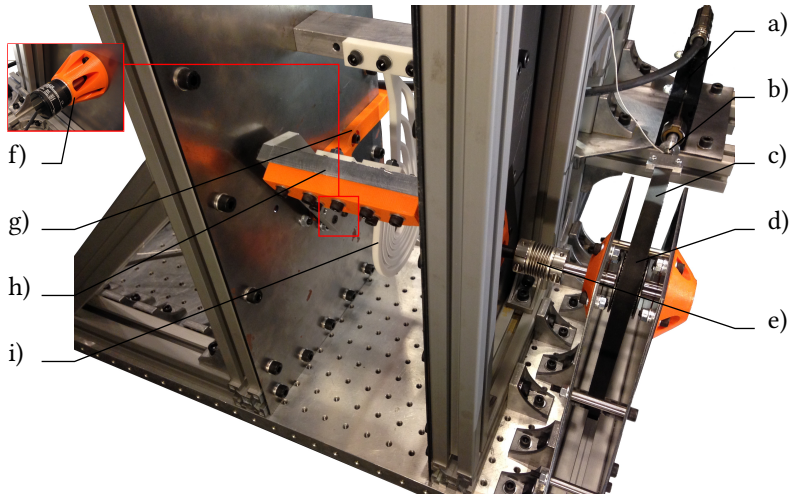


Figure 2.6: Experimental setup: a) linear motor, b) force sensor, c) timing belt, d) timing pulley, e) bellows coupling, f) encoder (mounted to the opposite side), g) lever homing end-stop, h) lever, i) specimen, j) counter mass

2.3.3 Data Acquisition

Prior to every measurement, the lever performs a homing procedure using the end-stop bracket to set the initial motor position and encoder angle. The measurements begin at an initial inclination to avoid static indetermination at the upright vertical position due to friction in the system. From that initial angle the lever moves to the upright vertical position ($\theta = 0$), to the downright vertical position ($\theta = \pi$), and back to the upright vertical position ($\theta = 0$), which marks the end of the measurement. The measurement data are obtained at a constant angular velocity of $\frac{\pi}{40}$ rad/s and a data acquisition rate of 55 Hz for **Set A** and **Set B** and $\frac{\pi}{80}$ rad/s and 105 Hz for **Set C**.

Table 2.1: Performance metrics

Parameter	Unit	Set A	Set B	Set C
δ	-	0.02004	0.01526	0.01659
U	J	2.02905	2.04874	5.01264
m	kg	0.03156	0.01642	0.03987
ϵ	J/kg	64.2917	124.771	125.725
A_{Δ}	cm ²	319.899	447.576	447.576
V_{Δ}	cm ³	1094.79	293.565	293.565
ω	J/cm ³	0.00185	0.00698	0.01708

The force sensor signal is filtered in post-processing using a moving average filter with a window size of 110 and 105 samples, respectively. For each beam the angle-moment characteristic is measured with and without the beam being mounted. The difference between both measurements yields the presented spring characteristic.

A target angle-moment characteristic is defined as

$$\dot{M} = -\dot{a}\sin(\theta) \quad (2.23)$$

where the factor \dot{a} is equal to the maximum absolute amplitude of the mean spring characteristic. Subtracting the target characteristic from the spring characteristic, yields the balanced angle-moment characteristic. For a movie showing the compound spring specimen (**Set C**) performing one load cycle on the test setup, please refer to supplementary file 5.

2.4 RESULTS

2.4.1 Computational Results

For all presented results the respective optimizations exited normally and without any constraint violations. Multiple runs for each set of optimization parameters are performed with different optimizer settings, in order to avoid local minima and to increase the chance of finding the global optimum.

The sets of optimized parameters for **Set A** and **Set B** are shown in Table 2.6 and the dimensions are given in Table 2.7 in the Appendix. The dimensions of all six beams that constitute the compound beam **Set C** are shown in Appendix Table 2.8. A significant difference between the dimensions is the out-of-plane width, which is 34.3 mm for **Set A** and 6.6 mm for **Set B** and **Set C**.

Table 2.2: Experimental results

Parameter	Unit	Set A	Set B	Set C
MAE	Nm	0.09628	0.05105	0.27291
NMAE(δ)	-	0.08757	0.05008	0.10906
RMSE	Nm	0.16450	0.06640	0.33337
NRMSE	-	0.14960	0.06514	0.13322

The final beam geometries are shown in Figures 2.7 and 2.8 for different deflected states. The corresponding moment response curves are shown in Figure 2.9. Note that, while the balancing behavior of **Set C** is qualitatively equivalent to **Set B**, the absolute amplitude of the moment curve has increased to 2.45 Nm. For a version of Figures 2.7 and 2.8 using the jet color map and animations of the deflecting beams, please refer to the supplementary files 1 - 4.

A comparison of the performance metrics of all spring designs is given in Table 2.1. The balancing errors for **Set A**, **Set B** and **Set C** as determined by the normalized mean absolute error (δ) are 2 %, 1.5 % and 1.7 %, respectively. Furthermore, it can be seen that the specific energy ε in the variable thickness designs is 94-96 % higher compared to the constant thickness design. In addition, the energy density ω increases by 277 % from constant to variable thickness, and further by 145 % from single beam to compound design, constituting a total increase of 823 % from **Set A** to **Set C**.

2.4.2 Experimental Results

The results in Figure 2.10 all show a pronounced hysteresis field. The balancing error between the mean spring characteristic and the target spring characteristic, listed in Table 2.2, is expressed in terms of the mean absolute error (MAE), the root mean square error (RMSE) and their normalized counterparts, NMAE respectively NRMSE. Normalization is achieved through division by the target amplitude \hat{a} . The balancing error according to the NMAE, which has the same definition as the objective δ , is 8.8 %, 5 % and 10.9 % for **Set A**, **Set B** and **Set C**, respectively.

2.5 DISCUSSION

2.5.1 Synthesis Method

While the original rationale to use the thickness as an additional design parameter was to gain more design freedom in order to allow for concentric stacking of beams, the results suggest that doing so, in addition, leads to an increased specific energy and energy density of the spring. The variable thickness approach appears particularly well suited to reduce the out-of-plane width. The variable thickness spring design **Set B** features a width, that is 81 % smaller in respect to the constant thickness counterpart **Set A**. However, along with the decrease in width the in-plane area covered by the variable thickness spring during deflection A_{Δ} increased by 40 %.

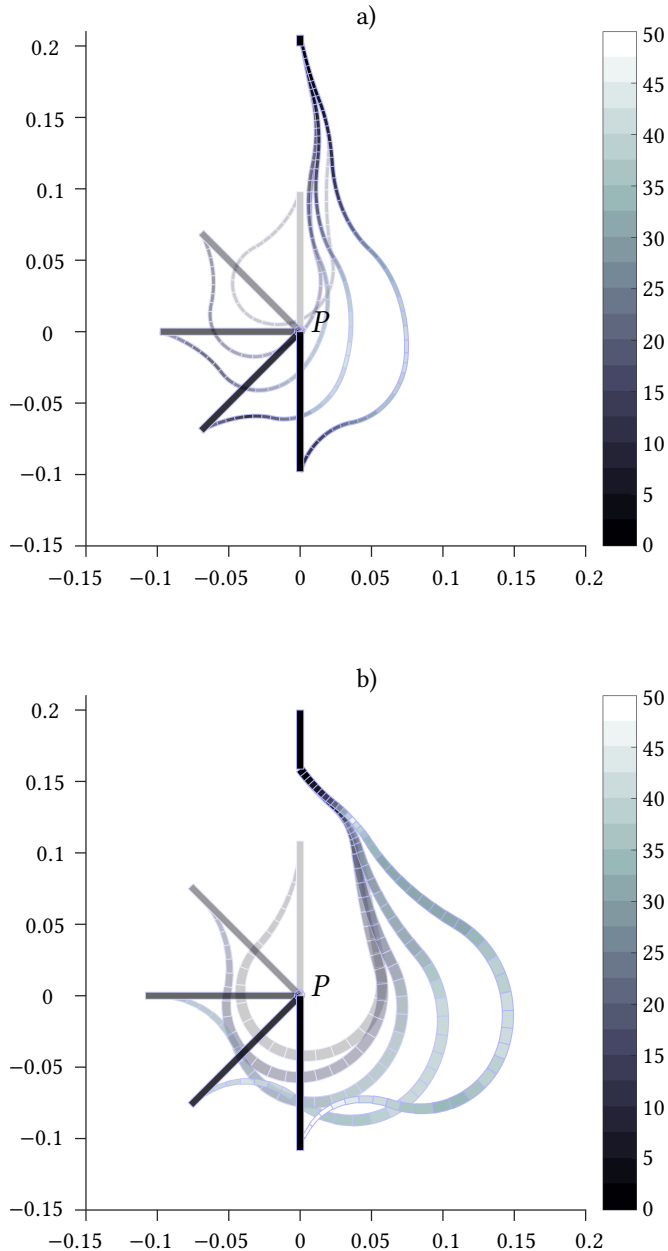


Figure 2.7: Deflection of the different beam designs. a): the constant thickness beam **Set A** and b): the variable thickness beam **Set B**. Transparency decreases linearly from 80 % to 0 % with increasing deflection. Axes in m, color scale in MPa (true color at 0 % transparency, i.e., full deflection).

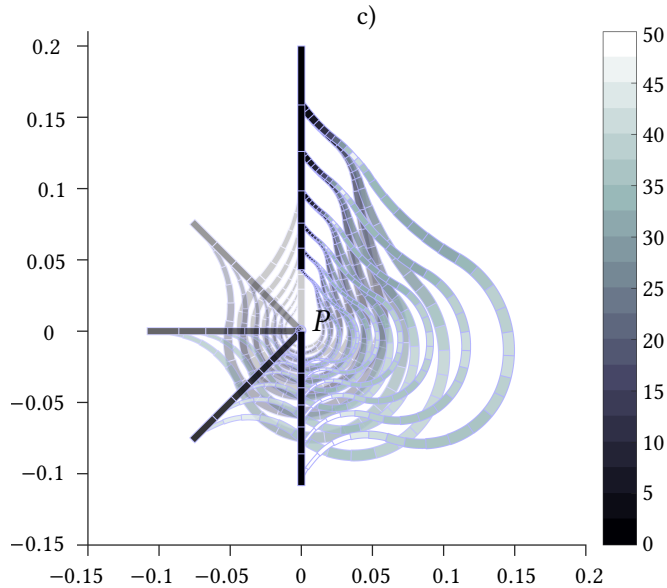


Figure 2.8: Continuation of Figure 2.7. c): the compound variable thickness beam **Set C**. Transparency decreases linearly from 80 % to 0 % with increasing deflection. Axes in m, color scale in MPa (true color at 0 % transparency, i.e., full deflection).

The nesting approach, on the other hand, appears well suited to reduce that in-plane area. By elimination of the outer beam of the presented nested design **Set C** the in-plane area can be reduced by 37 %, while maintaining a load capacity which is still higher than that of the original variable thickness spring **Set B**. Therefore, a promising direction for future work appears to specifically optimize springs towards an increased stack density of nested beams.

Still, the number of investigated designs is low and increasing the specific energy and the energy density are not immediate optimization objectives in this study. The complex relationship between the admitted amount of thickness variation, the resulting beam shape and achievable number of nested beams as well as their specific influences on gravity balancing quality, specific energy and energy density remain unclear.

2.5.2 Experimental Validation

The quality of the experimental validation is impaired by the choice of the spring material. The specimen made from laser sintered PA 2200 exhibit significant viscoelastic behavior. This negatively influences the validity of the presented results. Aside from the pronounced hysteresis, shown in Figure 2.10, a positive correlation between the stiffness and the testing speed was observed. Furthermore, performing consecutive experiments led to a rapid degradation of the desired mechanical behavior.

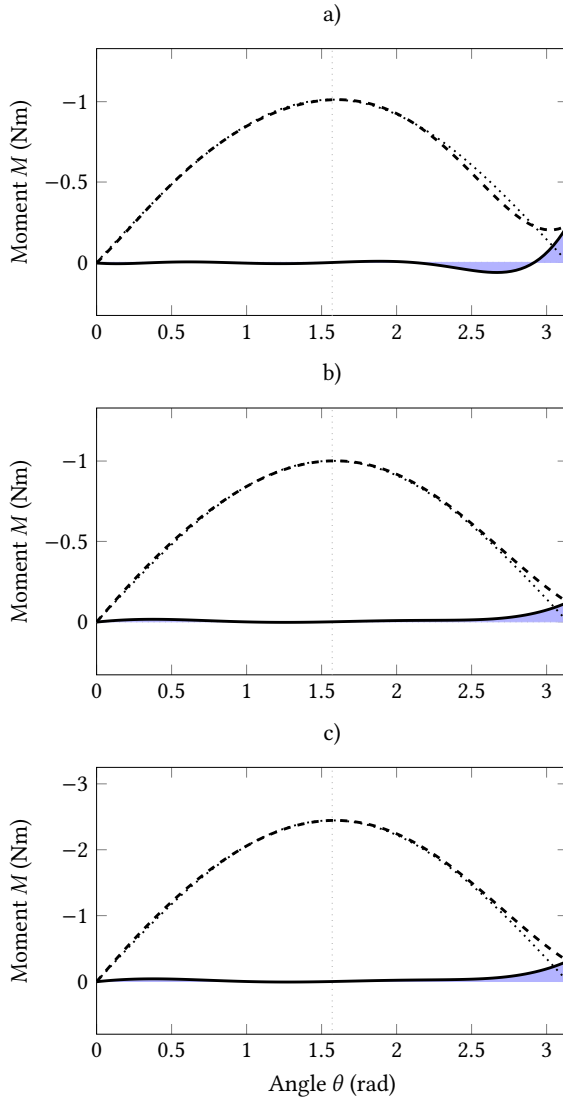


Figure 2.9: Moment response curves. From top to bottom a): **Set A**, b): **Set B** and c): **Set C**. The dashed line depicts the moment generated by the beam. The dotted line indicates the ideal angle-moment characteristic. The solid line shows the balanced moment, which results from adding the load moment (inverse of the ideal moment) to the beam moment. The shaded area between the solid line and zero depicts the mean absolute error, i.e., the objective. This diagram shows that in all three cases the gravity load is nearly completely balanced throughout the entire range of motion.

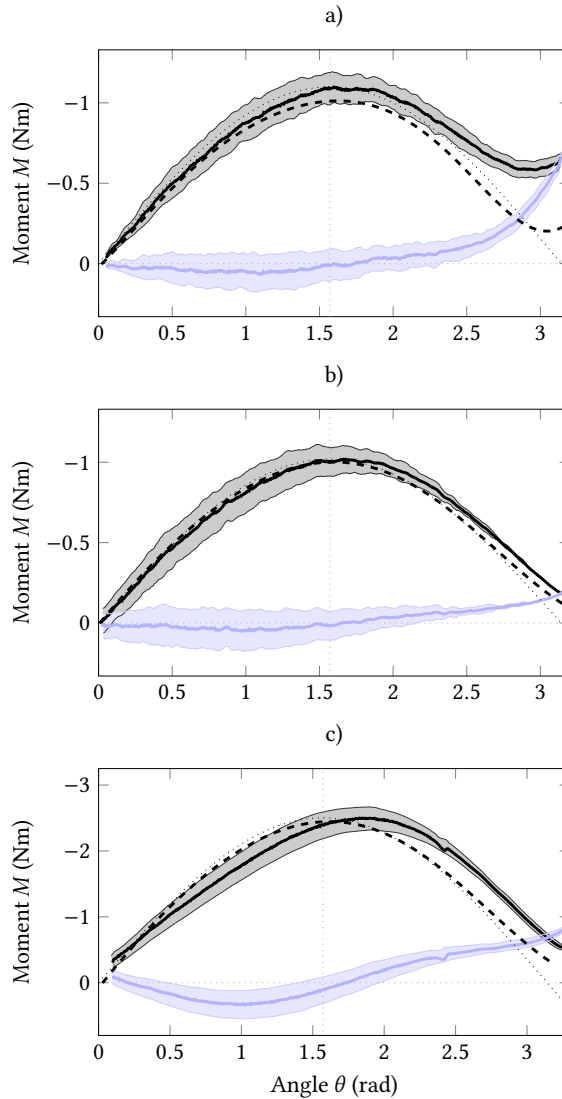


Figure 2.10: Experimental results for the beam specimens. From top to bottom a): **Set A**, b): **Set B** and c): **Set C**. The target angle-moment characteristic is depicted by the black thin dotted line. The thin black solid line depicts the moment generated by the beam specimen. The shaded area in-between indicates the hysteresis, while the thick black solid line depicts the mean. The balanced moment characteristic is depicted analogously in light blue. The corresponding simulation result is shown by the thick dashed line (compare also with Figure 2.9). This diagram shows that for all specimens the gravity load is mostly balanced throughout the entire range of motion with general trend of a slightly increasing deviation towards full deflection at π rad.

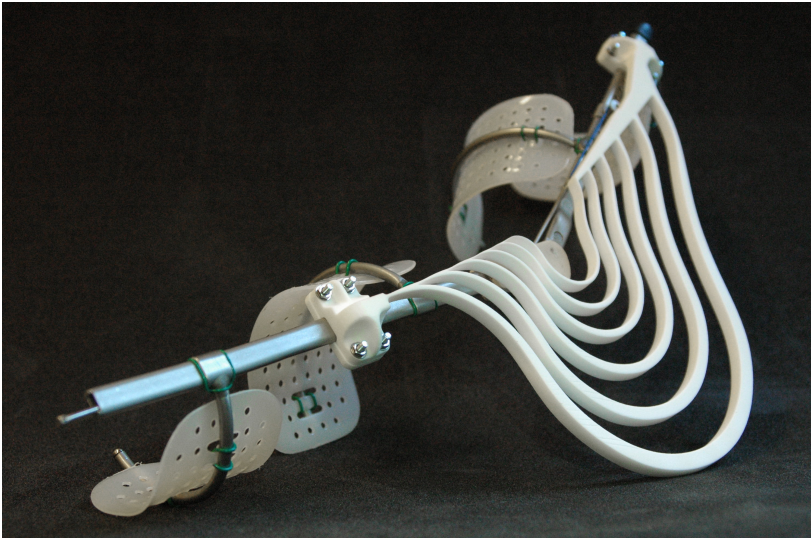


Figure 2.11: Wearable proof-of-concept prototype of the Assistive Elbow Orthosis (ÆOs). It consists of a Wilmer elbow orthosis [52] and a laser-sintered PA 2200 spring based on **Set C**, illustrating the lateral spring alignment. The orthosis is locked in the extended position.

2.5.3 Application

Based on a Wilmer elbow orthosis [52] and the **Set C** spring design a proof-of-concept prototype of an Assistive Elbow Orthosis (ÆOs) is built, which is shown in Figure 2.11. This prototype illustrates the close lateral alignment of the spring to the orthosis and thus to the body of the wearer. A lateral positioning appears conceptually advantageous, as in this configuration the spring does not impede tactile sensation on the backside of the arm, e.g., when resting the elbow and forearm on an object. The total weight of the device is 0.213 kg.

However, since the spring design from **Set C** is not adapted for increased wearability, its in-plane size remains too large to be worn underneath clothing. In future devices, a trade-off between using beams with smaller in-plane size and larger out-of-plane width may lead to a more favorable design. Dividing the effective out-of-plane width between two springs that are worn on either side of the arm may be done to mitigate lateral protrusion from the body. In addition, other materials may be investigated to further reduce the size of the spring and to avoid mechanical degradation due to creep and stress relaxation. For a movie showing the wearable prototype used by a healthy subject, refer to supplementary file 6. For a CAD model of the wearable spring shown in Figure 2.11, refer to supplementary file 7.

Extending the presented synthesis method to the other joints of the human upper and lower limb seems largely feasible. In many cases, the same spring designs as presented in this chapter can be used for that purpose. However, a few limitations and design challenges arise.

Due to the planar design of the spring it can only balance a single rotational degree of freedom. Proper alignment of the rotational axis of the spring to the balanced degree of freedom in the joint has to be ensured. This can pose a challenge for joints that have multiple degrees of freedom, large ranges of motion and shifting rotation axes.

Since collision with the wearer is disregarded and the nesting procedure attempts to use the entire space within the spring, a lateral alignment is always assumed.

Due to its passive nature, one side of the spring needs to maintain a fixed orientation relative to the gravity vector. Balancing of multiple joints across body segments can be achieved by decoupling mechanisms as shown in [10]. However, their technical embodiment may lead to an increased complexity, size and weight of the device and may impede the mobility of the affected joints.

For the shoulder joint specifically, a design with a fully extended initial lever position appears more favorable, as to avoid the fixed side of the spring being above the shoulder. Implementing this would require changes to the topology and task definition, which is left for future study.

2.6 CONCLUSIONS

This study is the first to explore variable thickness beam profiles as well as concentric nesting of beams in the context of gravity balancing flexure springs. Utilizing the presented synthesis method, three spring designs are obtained which exhibit gravity balancing behavior. The error in balancing quality is $\leq 2\%$ in simulation and 5-11% in experiment. By employing a variable thickness profile along the beam, the out-of-plane width is reduced drastically, by 81% in the presented case, and the energy to weight ratio is increased by 94% in comparison to the constant thickness design. Furthermore, this novel approach provides the additional design freedom to enable concentric nesting of multiple differently-sized beams. The resulting nested spring design exhibits a 145% increase of storable elastic energy compared to its single beam counterpart, while preserving the same outer dimensions.

These results show that employing the presented design methodology, gravity balancing springs can be obtained which ultimately feature a smaller size and a lower weight than comparable predecessors. In the context of passive gravity balancing exoskeletons the presented nested spring design offers a promising solution to increase wearability and decrease conspicuity, which are important criteria to promote the adoption of assistive devices for daily use. The proof-of-concept prototype illustrates a practical implementation.

2.7 APPENDIX

2.7.1 Tables

Table 2.3: Bounds, constraint values and penalty coefficients

Item	Parameter	Unit	Set A	Set B
\mathbf{b}_{ly_0}	y_{0min}	m	0.1	0.1
\mathbf{b}_{uy_0}	y_{0max}	m	0.2785	0.2785
\mathbf{b}_{ly_n}	y_{nmin}	m	0.05	0.05
\mathbf{b}_{uy_n}	y_{nmax}	m	0.2835	0.2835
\mathbf{b}_{ll}	l_{min}	m	0.005	0.005
\mathbf{b}_{ul}	l_{max}	m	0.5	0.5
$\mathbf{b}_{l\varphi}$	φ_{min}	rad	$-2/3\pi$	$-2/3\pi$
$\mathbf{b}_{u\varphi}$	φ_{max}	rad	$2/3\pi$	$2/3\pi$
$\mathbf{b}_{l_{tm}}$	tm_{min}	-	1	0.2
$\mathbf{b}_{u_{tm}}$	tm_{max}	-	1	1
$\mathbf{c}_{l(1)}$	L_{max}	m	3	3
$\mathbf{c}_{l(2)}$	Φ_{max}	rad	$8/3\pi$	$8/3\pi$
$\mathbf{c}_{nl(1)}$	l_{max}	m	0.5	0.5
$\mathbf{c}_{nl(2)}$	$b_{x_{min}}$	m	-0.05	-0.05
$\mathbf{c}_{nl(3)}$	$b_{y_{min}}$	m	-0.05	-0.05
$\mathbf{c}_{nl(4)}$	$b_{x_{max}}$	m	0.01	0.01
$\mathbf{c}_{nl(5)}$	$b_{y_{max}}$	m	0.3285	0.3285
$\mathbf{c}_{nl(6)}$	$n_{\times max}$	-	0	0
$\mathbf{c}_{nl(7)}$	d_{min}	m	-	0.05
$\mathbf{P}(1)$	λ_{max}	-	2	2
$\mathbf{P}(1)$	$k_{p(1)}$	-	10^5	10^5
$\mathbf{P}(2)$	$\bar{n}_{\times max}$	-	0	0
$\mathbf{P}(2)$	$k_{p(2)}$	-	10^5	10^5

Table 2.4: Dimensioning parameters

Parameter	Unit	Value
h_s	m	0.2
w_s	m	0.2
$t_{b_{min}}$	m	0.0004
$t_{b_{max}}$	m	0.05
FOS	-	1.2

Table 2.5: Material parameters of PA 2200 (PA12) Performance 1.0, at room temperature

Property	Parameter	Unit	Value
Tensile Modulus	E	MPa	1700
Shear Modulus	G	MPa	800
Tensile Strength	σ_t	MPa	50
Density	ρ	kg/m ³	930

Table 2.6: Optimized shape parameters

$\mathbf{x} =$			
Parameter	Unit	Set A	Set B
y_0	m	0.222087	0.192382
y_n	m	0.104909	0.131396
l_1	m	0.097847	0.082104
φ_1	rad	-1.354998	-0.92193
l_2	m	0.129454	0.185152
φ_2	rad	-0.630883	-0.94523
tm_1	-	1	0.799912
tm_2	-	1	0.463851
tm_3	-	-	0.999999
tm_4	-	-	0.999999
tm_5	-	-	0.200226

Table 2.7: Dimensions: single beams

Parameter	Unit	Set A	Set B
h	m	0.200000	0.200000
w	m	0.048781	0.044597
s	-	0.934411	0.824749
t_b	m	0.002765	0.007867
w_b	m	0.034223	0.006559

Table 2.8: Dimensions: compound beam

Par.	Unit	Set C					
		c_1	c_2	c_3	c_4	c_5	c_6
h	m	0.2000	0.1588	0.1240	0.0955	0.0733	0.0543
w	m	0.0446	0.0354	0.0276	0.0213	0.0164	0.0121
s	-	0.8247	0.6550	0.5114	0.3938	0.3024	0.2241
t_b	m	0.0079	0.0062	0.0049	0.0038	0.0029	0.0021
w_b	m	0.0066					

2.7.2 Supplementary Files

- **Supplementary file 1 – Fig_Stress_Jet.pdf**
Alternative version of Figures 2.7 and 2.8 using the jet color map. Axes in m, color map in MPa.
- **Supplementary file 2 – Animation_A.gif**
Animated image showing the deflection and stress distribution of the optimized constant thickness beam design. Axes in m, color map in MPa.
- **Supplementary file 3 – Animation_B.gif**
Animated image showing the deflection and stress distribution of the optimized variable thickness beam design. Axes in m, color map in MPa.
- **Supplementary file 4 – Animation_C.gif**
Animated image showing the deflection and stress distribution of the optimized nested beam design. Axes in m, color map in MPa.
- **Supplementary file 5 – Experiment.mp4**
Movie showing the nested beam design performing one load cycle on the test setup. The movie has an increased playback speed of four times.
- **Supplementary file 6 – Wearable_Prototype.mp4**
Movie showing the wearable prototype worn and used by a healthy subject.
- **Supplementary file 7 – Wearable_Spring_2,45Nm.STEP**
CAD model of the wearable spring in a neutral file format (STEP AP214).
- **Supplementary file 8 – Nomenclature.pdf**
Nomenclature tables which explain the symbols, indices and abbreviations.

The downloadable supplementary materials are available at:

<https://research.utwente.nl>

Digital Object Identifier 10.3990/1.9789036551342

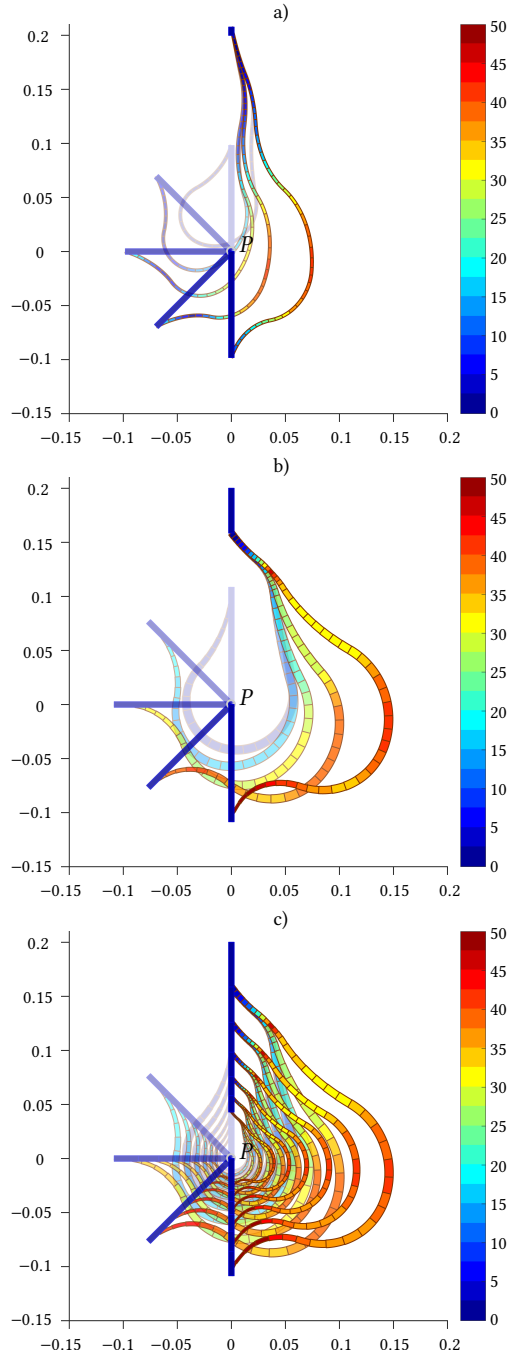
High image resolution movies (261 MB)

<https://ieeexplore.ieee.org>

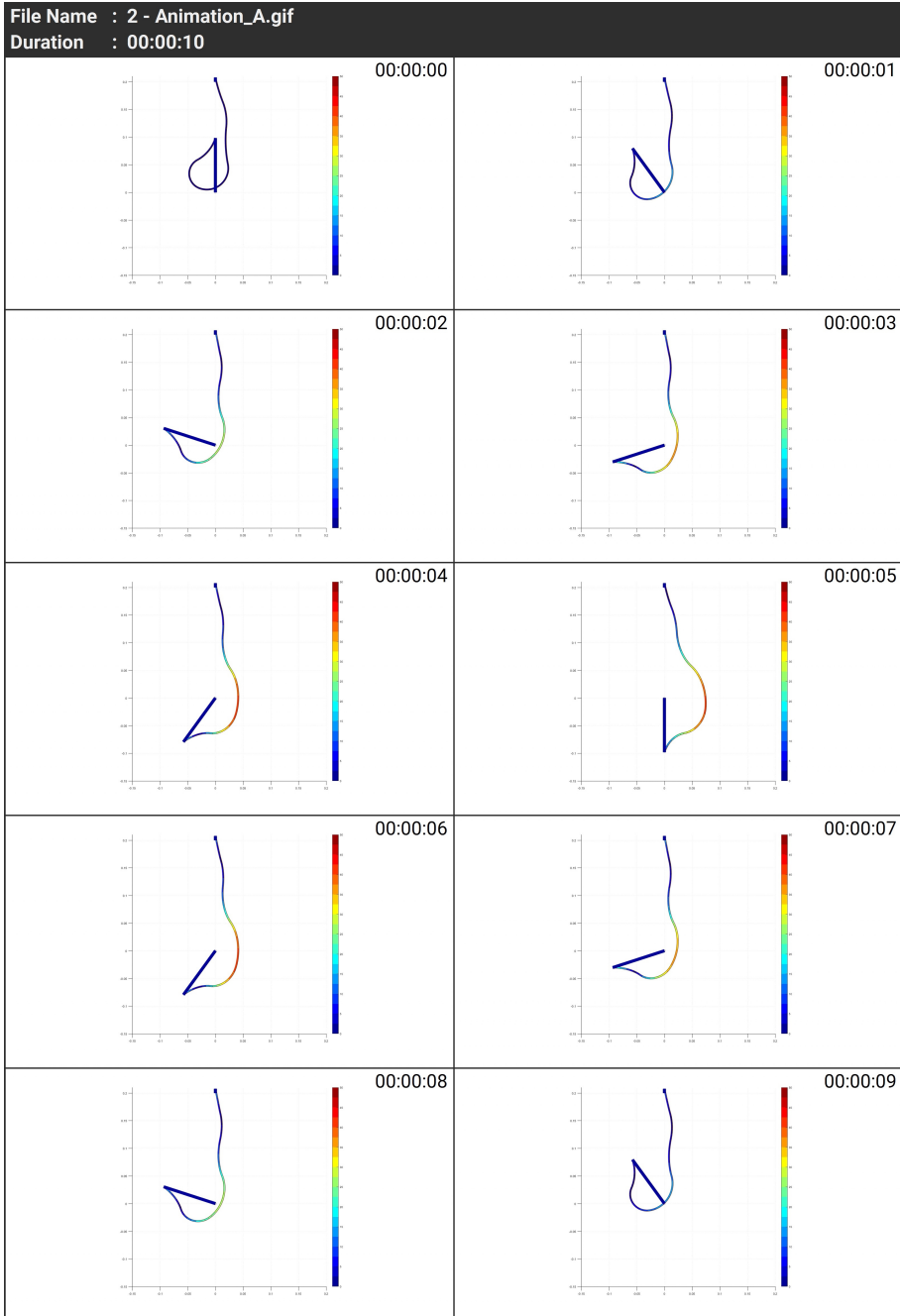
Digital Object Identifier 10.1109/TMRB.2019.2930341

Standard image resolution movies (68 MB)

For alternative links and additional materials, visit: <https://tschiersky.org/dissertation>

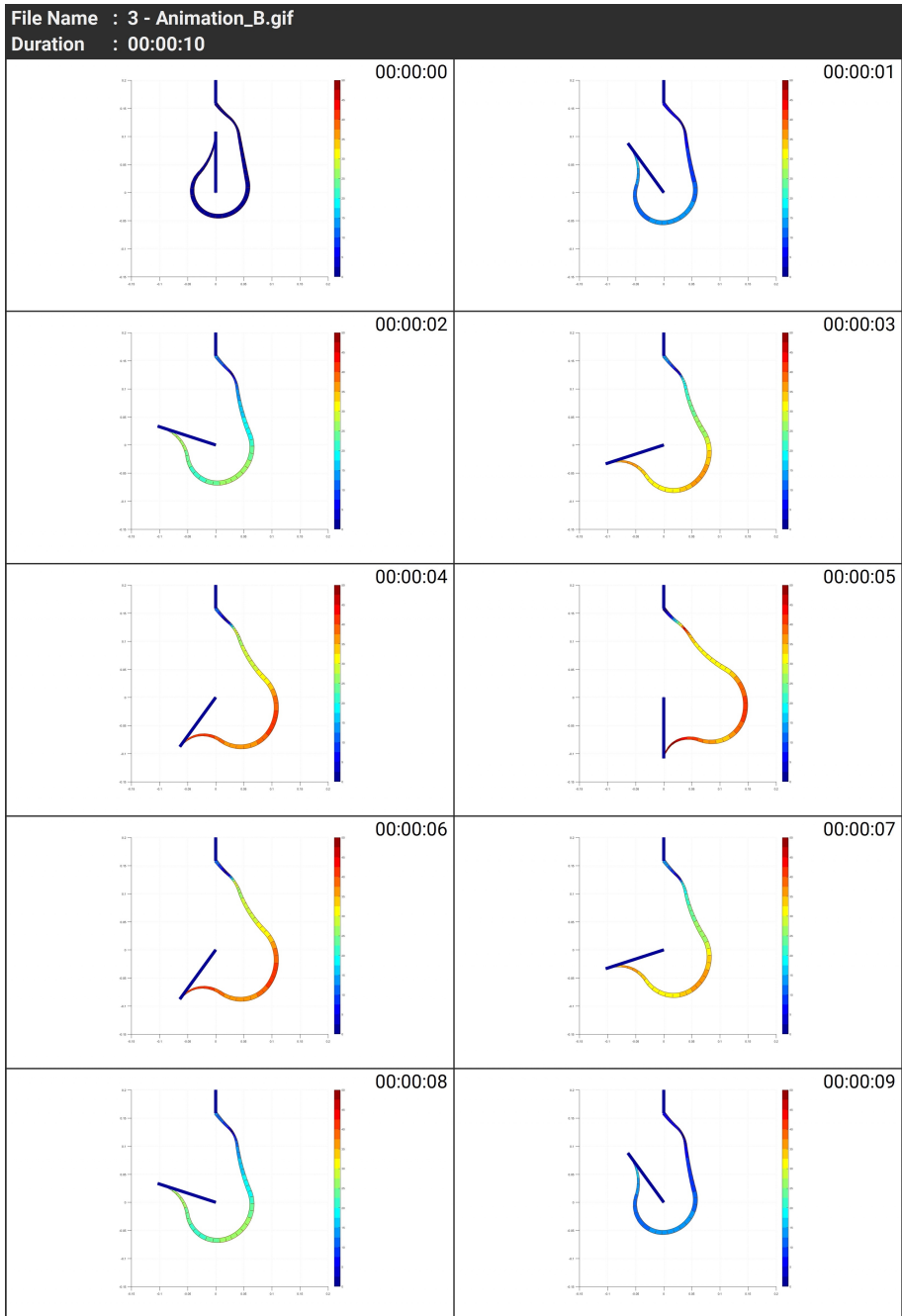


Preview: Supplementary file 1 – Fig_Stress_Jet.pdf

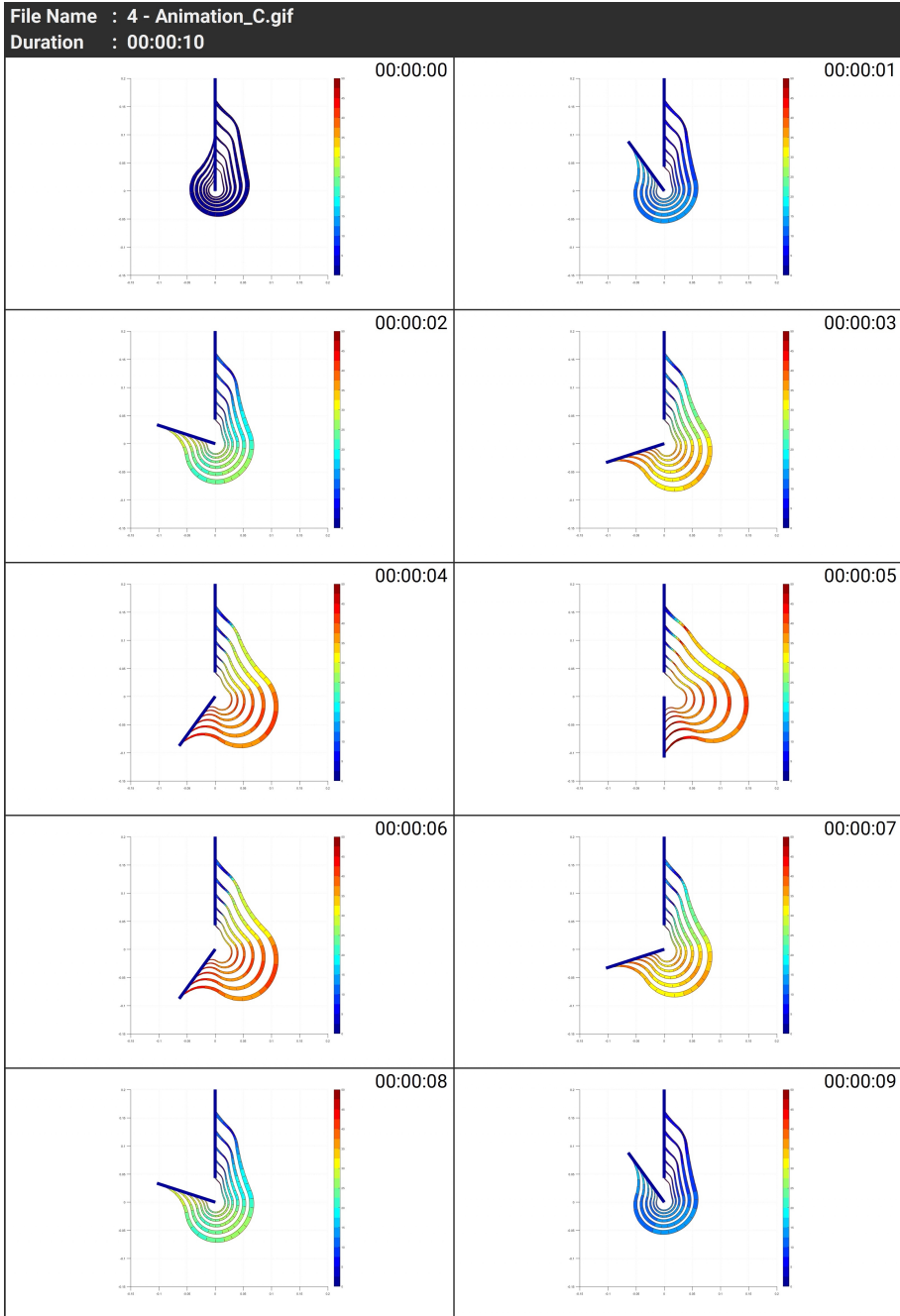


2
A

Preview: Supplementary file 2 – Animation_A.gif

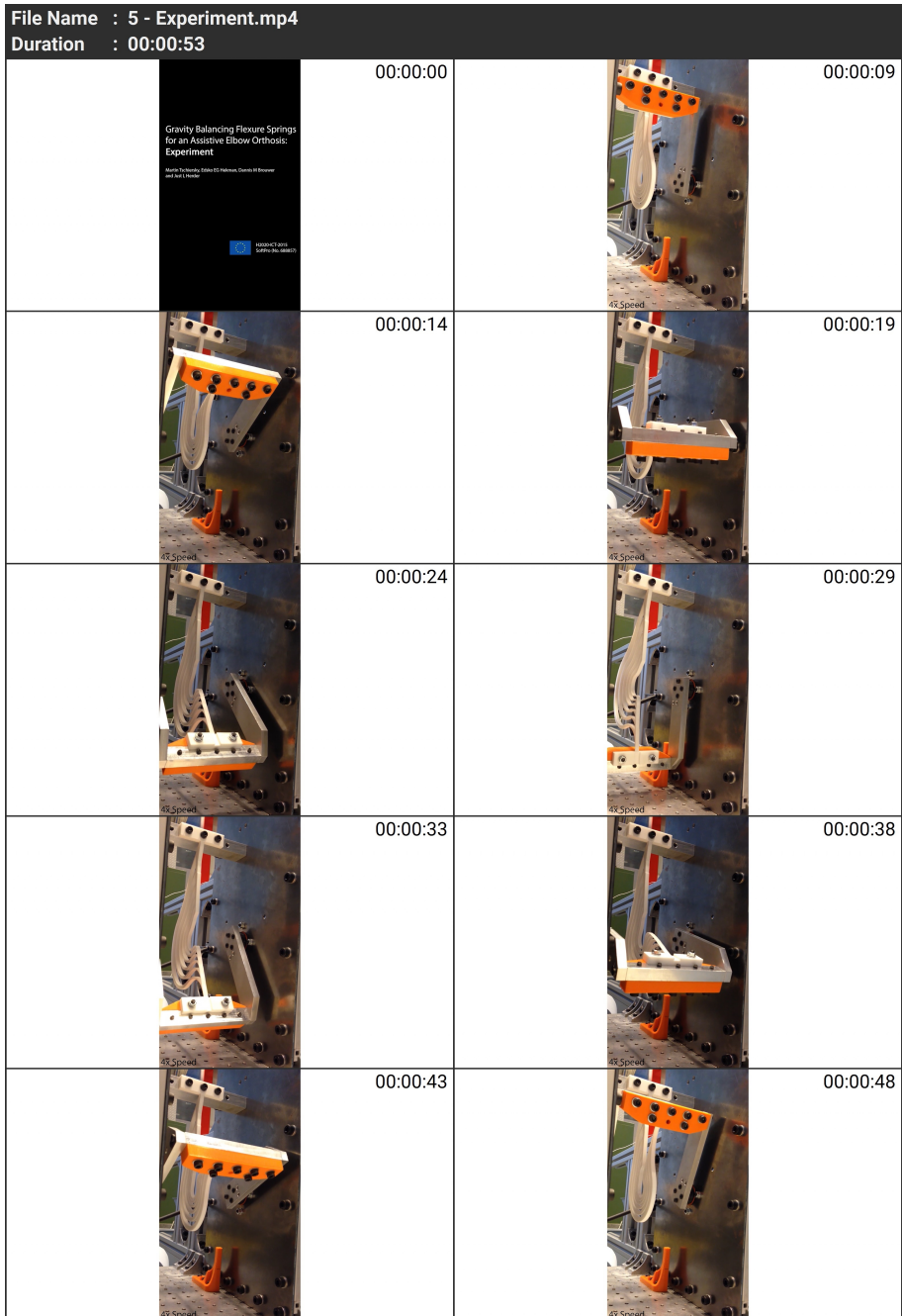


Preview: Supplementary file 3 – Animation_B.gif

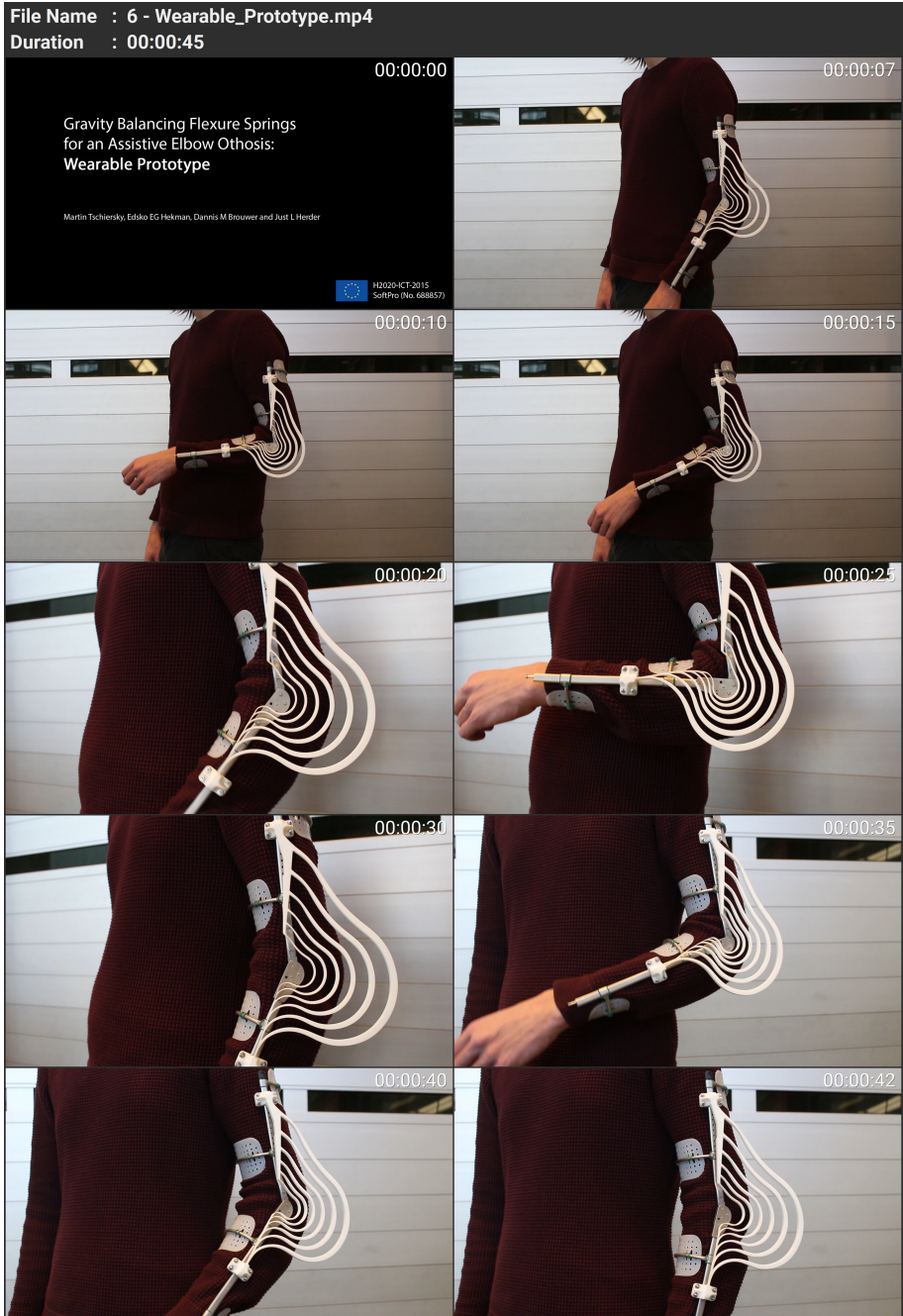


2
A

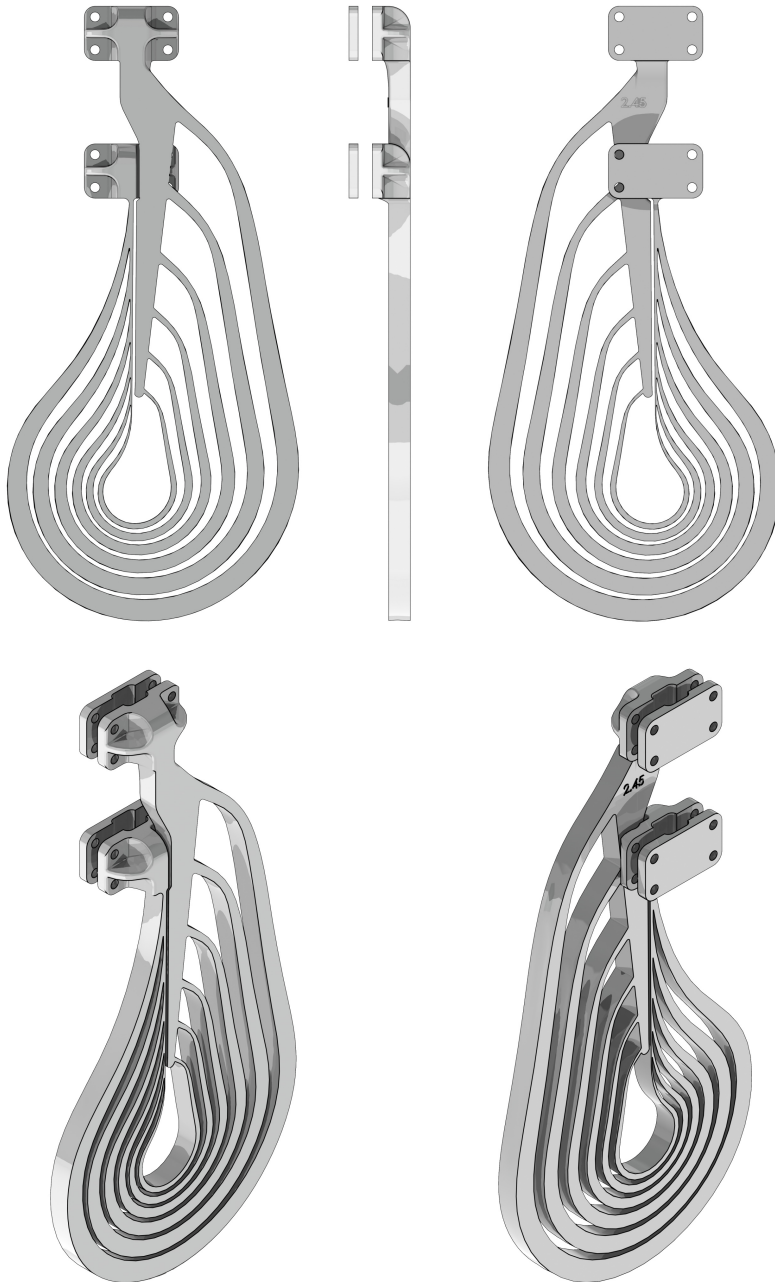
Preview: Supplementary file 4 – Animation_C.gif



Preview: Supplementary file 5 – Experiment.mp4



Preview: Supplementary file 6 – Wearable_Prototype.mp4



Preview: Supplementary file 7 – Wearable_Spring_2,45Nm.STEP

Gravity Balancing Flexure Spring Mechanisms for Shoulder Support in Assistive Orthoses

Abstract Passive shoulder supports show large potential for a wide range of applications, such as assisting activities of daily living and supporting work-related tasks. The rigid-link architecture used in currently available devices, however, may pose an obstacle to finding designs that offer low protrusion and close-to-body alignment. This study explores the use of mechanisms that employ a flexible element which connects the supported arm to an attachment at the back and acts as energy storage, transmission and part of the load bearing structure. Based on the synthesis method explained in this chapter, a large scope investigation into possible flexure-based mechanism topologies is conducted. Thereby, many potential designs are discovered, which are presented, categorized and compared. Two promising designs are developed into prototypes, and are built and tested on a dedicated test bench. These two mechanisms reduce the necessary moment to lift the arm by more than 80 % throughout 85 % of the range of motion, while staying within 18 cm and 10 cm distance from the body, respectively. The study indicates that, due to its lower protrusion and interface loads, a design with a tapered flexure connecting the upper arm via a hinge to a spring loaded slider at the back offers the most promising solution.

3.1 INTRODUCTION

Upper-limb wearable assistive devices are used to facilitate functional arm movements. By providing supporting forces and moments to the wearer they reduce the amount of muscle exertion necessary to perform manual tasks. While potentially beneficial for a wide range of use cases, they are currently mostly used and investigated in two main areas. The first pertains to people suffering from deficient motor function who can use such devices to restore their ability to perform activities of daily living (ADLs), and thus reduce their reliance on external help [14, 66]; The second concerns workers who are exposed to physically demanding tasks, and who may use them to mitigate their risk of work-related musculoskeletal disorders (MSDs) [43].

Assistive devices for the upper limb can be broadly characterized as either end-effectors or orthoses. The latter can be subdivided into rigid exoskeletons and soft exosuits. Within each category further distinctions can be made based upon the applied actuation scheme [14, 39, 40, 66, 68, 69]. Active exoskeletons and, more recently, exosuits are being extensively investigated in academic research. However, commercially available devices for assisting ADLs are predominantly passive end-effectors

Submitted to IEEE Transactions on Medical Robotics and Bionics

Preprint available at TechRxiv.org

Co-authors: E.E.G. Hekman, J.L. Herder and D.M. Brouwer.

[66], while work-assist devices that support the upper limb are exclusively passive exoskeletons [43].

Considering passive orthoses that provide dynamic shoulder support, five potentially fully wearable devices designated for assisting ADLs exist to the author's knowledge. The A-Gear [35], Panto-Arm Exo [25] and SpringWear [8] are academic research prototypes, while the EksoUE [16] and Wilmington Robotic Exoskeleton (WREX) [23, 73] are commercially available devices. On the other hand, in recent years several companies have entered the market with wearable work-assist exoskeletons. Examples are: the Airframe [3, 27], EksoVest and EVO [16, 31], MATE [41, 50], PAEXO [42, 51], ShoulderX [60, 67] and SkelEx [61, 71].

All the above mentioned are passive devices that work by applying forces and moments to the wearer's upper limb, which counter the gravity loads acting upon it. Thus, the amount of force the user has to exert in order to lift the arms is reduced. To this end, these exoskeletons employ rigid-link mechanisms that contain energy storing elements like tension and compression springs [3, 41, 60], gas springs [16, 25], rubber bands [8, 35, 51, 73] and leaf spring flexures [61] in combination with transmission elements like rigid linkages [8, 25, 35, 51, 61, 73], cable-pulley configurations [3, 60], gears [41] and cams [16] which together create the desired mechanical behavior. These types of mechanisms, however, imply an exoskeleton design in which a rigid frame and rigid links are used to interface with the wearer's body. Such being the case, additional links, joints and sliders are added to make the largely rigid structure adjustable and comply with the shoulder kinematics, increasing the complexity and number of parts necessary. Furthermore, to avoid potentially harmful collision moving parts are required to maintain a safe distance to the body, often leading to significant protrusion.

The research presented in this chapter attempts to address these issues. In the presented design approach a flexible element resembling a curved flexure with variable thickness is connected between the user's back and upper arm. Like in the SkelEx device, this flexure acts as both the energy storing element and as part of the frame. However in contrast, the flexure is designed to be more compliant and exhibit large deformations. Furthermore, no additional links between the arm and the back are used to prescribe its deformation and to create the gravity-balancing properties. Instead, by utilizing the natural shoulder kinematics, the gravity-balancing behavior emerges from the shape of the flexure in combination with the kinematic constraints prescribed at each end. Thus, the flexure integrates functions of energy storage, transmission and the load bearing structure.

This approach is used to obtain devices that are structurally more compliant than current exoskeletons, while preserving comparable external load bearing capabilities. Utilizing the gain in flexibility, the goal is to bring the device closer to the wearer's body, as due to the yielding nature of the flexure it is hypothesized that the wearer would not incur any harm in the event of a collision. Furthermore, the flexure may offer enough compliance to allow motion in the non-actuated directions, reducing the need for dedicated mechanisms to comply with the degrees of freedom of the shoulder. Together with the above described function integration this may reduce the overall complexity and lead to a smaller part count.

To find appropriate designs, a computational model is created which encompasses the flexible element and the wearer, to simulate the mechanical behavior of the entire system and to determine the distance between the two. Using this model, flexure shapes are optimized for various support conditions at each end, to find flexure spring mechanisms that offer both adequate gravity-balancing support and close-to-body alignment.

The approach is based on the previous work concerning gravity-balancing flexure springs for an assistive elbow orthosis [65]¹ and similar work on gravity-balancing flexure mechanisms within [9, 10] and without [54, 55, 56] the context of assistive devices. However, the method is expanded by introducing a new use case, multiple design objectives and more complex spatial constraints, in which collision with the body is to be avoided while remaining in close proximity to it. Furthermore, an extensive investigation is conducted to examine the effects of using different kinematic support conditions at each end of the flexure, representing sliders, hinges and combinations thereof with zero, finite or infinite stiffness.

Following this introduction the *Synthesis* section describes the applied methods by which gravity-balancing flexure spring mechanisms for several different kinematic support conditions are obtained. From these, two support conditions are selected for further investigation, from which two prototype designs are derived. The subsequent *Experiment* section deals with the physical validation of these prototypes on a dedicated test bench. The outcomes of both the synthesis and experiment are presented in the *Results* section and reflected upon in the *Discussion* section. Lastly the key insights are provided in the *Conclusions* section.

3.2 SYNTHESIS

3.2.1 Model Topology

For the design of the flexure mechanisms, the flexible element with its end supports, as well as the torso and right arm of the wearer are considered. The schematic model topology is shown in Figure 3.1. Mechanically, the shoulder joint is reduced to a pair of revolute joints which are connected to each other and coincide with the position of the glenohumeral joint. The joints are oriented perpendicular to each other and their motion corresponds to the upper arm elevation θ and horizontal flexion/extension γ , respectively. Their position in space is fixed with respect to ground. Endo/exorotation of the arm is not considered. The arm itself is treated as a rigid link with a mass m located at the center of gravity and is connected to the pair of revolute joints at its proximal end. The position of the mass is fixed as elbow and hand motion are not considered.

¹Reference [65] is equivalent to Chapter 2 of this thesis

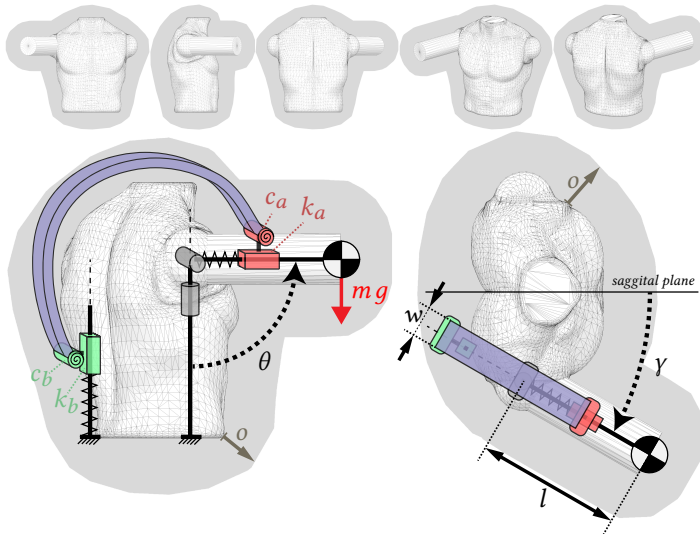


Figure 3.1: Model topology. The triangulated meshes for the torso and right upper arm are shown in white, the offset mesh volume is indicated in gray. The top figures show the meshes from several perspectives. The bottom left figure is a view perpendicular to the arm elevation plane. The bottom right figure is a view from the top. Rigid links are shown as black bold lines. Their axes are indicated by dashed lines. The prismatic and revolute joints are drawn in gray for the shoulder, red for the arm interface and green for the back interface. The flexible element, i.e., the flexure, is shown in blue.

The flexible element is treated as a prismatic beam with a rectangular cross-section and a varying thickness along its length. It is connected to a point at the back of the wearer at one end, travels above the top of the right shoulder, and connects to the upper arm section of the arm link at the other end. At each interface point the flexure is connected via a slider/hinge combination. The slider at the back allows motion along the vertical axis and the slider on the arm motion along the arm axis. The orientation of the hinges is perpendicular to the arm elevation plane. By setting the stiffnesses of these kinematic elements, each connection can be modeled as either a clamp, slider, hinge or a combination of both slider and hinge. In addition, when using finite stiffness values, each element can also act as a spring with a translational stiffness k or rotational stiffness c , respectively.

The volumes of the torso and right upper arm are represented by triangulated meshes. The position and orientation of the torso mesh is fixed, while the upper arm mesh orientation follows the arm link. For each mesh a corresponding offset mesh with a uniform offset o prescribes the space in which the flexible element is allowed to operate.

3.2.2 Design Objectives

The primary goal of this study is to find the ideal shape and thickness distribution of the flexible element, and the ideal joint stiffness values for each prescribed kinematic support condition, such that the resulting mechanism balances the mass m on the arm link, while not colliding with, but staying within close proximity to the wearer. This should be achieved while featuring a small flexure width to reduce the overall size, protrusion and out-of-plane stiffness. Furthermore, to allow for a design in which the flexible element can be directly connected to the arm, parasitic forces and moment that do not contribute to the gravity-balancing behavior should be minimal. To this end, four metrics are used to assess the quality of a design.

Gravity balancing quality, which is the primary objective, is defined as the ability of the flexure mechanism to counteract the effect of gravity on a mass m , such that the moment M at the shoulder elevation joint is zero for any elevation angle θ in the range from 0 to π . For the given model, the moment caused by gravity can be expressed as:

$$M_g = -a_g \sin(\theta) \quad a_g = mgl \quad (3.1)$$

where a is the moment amplitude, g the gravitational acceleration and l the distance between the center of gravity and the shoulder joint. Consequently, the moment M_f exerted by the flexure mechanism has to be the inverse. However, M_g and M_f are normalized by their respective maximum amplitude to obtain the relation for the ideal case:

$$\frac{M_f}{a_f} - \sin(\theta) = 0 \quad a_f = \max(|M_f|) \quad (3.2)$$

The gravity balancing quality can now be expressed by the cumulative error in this equation for the considered range of motion. Since the elevation angle in both simulation and experiment is discretized, the normalized mean absolute error (NMAE) is chosen for this purpose:

$$\delta = \sum_{i=0}^n \frac{\left| \frac{M_{f,i}}{a_{f,i}} - \sin(\theta_i) \right|}{n} \quad (3.3)$$

where i is a data point and n the total number of data points.

The second metric is the ratio between the maximum moment amplitude and the flexure width w , serving as an indicator for the relative strength of the design. This is defined as:

$$\epsilon = \frac{a_f}{w} \quad (3.4)$$

The third metric is the maximum protrusion of the flexible element from the body. It is measured as the maximum distance between the left or right edge of the flexure's neutral plane, i.e., mid-plane, to the respective closest position on the combined torso and arm mesh.

Finally, the fourth metric is the ratio between the maximum amount of shear force at the arm interface and the maximum moment amplitude. The shear force is defined as the force component at the arm interface parallel to the arm axis. It is defined positive when pointing in distal direction, and negative when pointing in proximal direction.

3.2.3 Application Requirements

The device is intended to assist in the lifting of the arms when no additional payload is considered. This type of support is rather task independent and would potentially benefit both prior mentioned use case scenarios of assisting ADLs and physically demanding work-related tasks. The device shall work for the entire range of motion of the shoulder from the relaxed arm position at $\theta = 0$ to the raised position at $\theta = \pi$.

In order to provide adequate gravity compensation, both the balancing quality and the balancing quantity have to be sufficient. Based on the experience from previous work [65], it is determined that a NMAE ≤ 0.05 would constitute a good balancing behavior. Regarding the quantity, it is calculated that based on the mean body segment data of female and male subjects [38] a moment amplitude of 9.16 Nm would be necessary to fully compensate for the gravity loads acting upon the arm. Based on this number a target moment amplitude of 10 Nm is chosen, offering a margin for customization.

The protrusion of the device from the body should be minimal. A study on passive assistive orthoses found that devices should stay within 30 mm from the body, and to be wearable underneath clothing even below 20 mm [14]. However, considering existing passive assistive shoulder supports, these figures seem overly ambitious. Therefore, no hard requirement is derived. Instead, this design aspect is treated as a main point of investigation.

It is known from literature that contact pressure and shear applied to the skin should be minimal in order to comfortably use a device for extended periods of time [58]. However, no practical threshold values that pertain to the presented use case could be found in literature. Therefore, this aspect is also left open for investigation.

3.2.4 Additional Specifications

This study is limited to planar mechanism designs. This is done in order to reduce the number of design parameters for the optimization. In addition, to reduce simulation effort the arm elevation is only investigated in one plane. To this end, an elevation plane with a horizontal extension angle of $\gamma = \frac{\pi}{6}$ towards the sagittal plane is chosen.

Regarding the protrusion criterion, heightened attention is placed on arm elevations between $\theta = 0$ and $\theta = \frac{\pi}{2}$, since a low protrusion is deemed more critical for ADLs of which most only require this range of motion [48].

A model of a 183 cm tall male subject is used for reference to determine collision with and protrusion from the torso. The upper arm is assumed to be a cylinder with 10 cm diameter and 30 cm length.

3.2.5 Computational Model

For analysis the flexible multibody dynamics software package SPACAR [29] is used. The entire mechanism is modeled using hinges and finite two-node beam elements which feature geometric nonlinear behavior and flexibility formulated in six discrete deformation modes.

At the shoulder a hinge corresponding to the arm elevation is fixed to the ground at one end and connected to the arm link at the other. Its position marks the origin of the Cartesian coordinate system. The arm link is modeled as a beam with one released deformation mode that corresponds to its elongation. As it can only permit motion along its axis and otherwise acts rigid, it can be used to model a slider with a linear stiffness k_a . A small perpendicular rigid beam extends from the arm link, i.e., the arm axis, to a position 2 cm above the surface of the arm cylinder. At this position, which serves as the interface point to the flexure, a hinge with a rotational stiffness c_a is placed to connect arm and flexure. At the back a similar construction is used to model the vertical slider with linear stiffness k_b and the back hinge with rotational stiffness c_b , though in this case no extension beam is used.

Setting the stiffnesses to infinite, zero or finite values enables the modeling of clamps, hinges, sliders and slider/hinge combinations at each interface point, with and without springs acting in parallel to the joints. A point mass of 0.2 kg is assigned to the back interface to account for the weight of the mechanical components.

The flexure which connects the hinge at the back to that on the arm is modeled as a chain of multiple beam elements that allow initial pre-curvature [44] and are fully released, thus exhibit full flexible behavior. By definition the chain starts at the back and ends at a point above the shoulder joint. The initial position of the back slider and hinge are set according to the start position of the beam. Similarly, the initial length of the arm link and the initial elevation angle of the shoulder hinge are set such that the arm interface point coincides with the end of the flexure. As a consequence and since no pre-tension is applied, the elevation angle that corresponds to the unstressed position of mechanism depends on the flexure design.

The mesh of the torso is derived from a CAD model of a full human body. The head, arms and lower extremities are removed and spherical volumes are placed at the position of the glenohumeral joints. The position of the right glenohumeral joint is made to coincide with the shoulder hinge. The torso is rotated about the origin to set the relative angle $\gamma = \frac{\pi}{6}$ between the plane of the mechanism and the torso's saggital plane. The cylinder mesh representing the upper arm is fixed to the origin at its proximal end and is aligned with the upper arm link. The offset meshes for the torso and arm are generated from the original collision detection meshes using a voxel-based approach, and placed and oriented in the same way.

3.2.6 Simulation

To analyze a mechanism design, a kinetostatic analysis is performed. The model is first moved from its arbitrary initial position to the fully raised position at $\theta = \pi$. Then the shoulder hinge controlling arm elevation is rotated from $\theta = \pi$ to $\theta = 0$ in a number of predefined load steps n . For each load step the moment at the shoulder, as well as the forces and moments at the interface points are evaluated. Furthermore, based on the node positions and orientations as well as the width of each flexible beam element constituting the flexure, contact nodes are generated that lie on the vertices of each beam's neutral plane. These contact nodes are used to determine whether a beam lies within the torso mesh, arm mesh or their respective offset meshes. Based on that information, the protrusion distance from, or the penetration depth into the torso and arm mesh is measured for each node.

3.2.7 Parametrization

In order to optimize the mechanism its components have to be parameterized. The neutral axis of the flexure, and thus the node positions and orientations for each beam element, is obtained by constructing a Frenet ribbon with minimum torsion from a natural cubic spline curve which interpolates a number of control points. The position of the first control point is given explicitly by its coordinates, while all other points are obtained through a linkage chain formulation similar to the one used in [65]. To this end, the first two parameters of the parameter set are the horizontal position s_x and the vertical position s_z of the starting point at the back. These are followed by a number of link lengths l and angles φ corresponding to the number of links in the linkage chain and consequently to the number of additional control points. An illustration of such a linkage chain can be found in [65], though for this study instead of relative angles between links, absolute angles towards the ground are used. The thickness of each beam element is obtained by linear interpolation of the thickness parameters t over the beam nodes. The mean value of the thickness values at the two nodes of each beam element yields its thickness in the model. An illustration of this can also be found in [65], though instead of multipliers, absolute thickness values are used. Lastly, depending on the investigated support conditions for the flexure, the stiffness values of the slider and hinge elements are appended, yielding a parameter set in the form:

$$\mathbf{x} = [[s_x, s_z], [l_1, \dots, l_n], [\varphi_1, \dots, \varphi_n], [t_1, \dots, t_n], [k_a, c_a, k_b, c_b]] \quad (3.5)$$

3.2.8 Optimization

To find optimal parameter sets a two-step optimization procedure is conducted. First the mechanisms are optimized towards a high balancing quality, i.e., to minimize the error δ as defined in Equation 3.3. In the second step, this error is limited to $\delta \leq 0.05$, while the relative strength of the mechanism is optimized towards a maximum value of ϵ as defined in Equation 3.4.

With the exception of the redefinition of δ from objective to constraint, both optimizations are subject to the same set of bounds and constraints. The constraints are implemented as inequality constraints, denoted \mathbf{c} , and soft constraints, i.e., penalties \mathbf{p} . The inequality constraints \mathbf{c} are evaluated for the initial mechanism state, before running the SPACAR simulation. If any of these produce a value > 0 , the simulation is skipped and an error value returned. The penalties \mathbf{p} , similar to the objectives δ and ϵ , are evaluated after the simulation. Their values are multiplied with a penalty factor $k_p = 10^5$ and added to the cost function. The two cost functions can be written as:

$$f_1(\mathbf{x}) = \delta + k_p \mathbf{p}_{(1-6)} \quad (3.6)$$

$$f_2(\mathbf{x}) = \frac{1}{\epsilon} + k_p \mathbf{p}_{(1-7)} \quad (3.7)$$

$$\text{subject to } \mathbf{c}_{(1-7)} \leq 0$$

The first two constraints $\mathbf{c}_{(1)}$ and $\mathbf{c}_{(2)}$ check, whether the distal end of the arm is pointing upwards with a maximum deviation of $\alpha = \frac{\pi}{9}$ from vertical.

$$\mathbf{c}_{(1)} = \cos(\theta_{init}) \quad (3.8)$$

$$\mathbf{c}_{(2)} = |\sin(\theta_{init})| - \sin(\alpha) \quad (3.9)$$

where θ_{init} is the initial angle of the arm link.

The next two constraints $\mathbf{c}_{(3)}$ and $\mathbf{c}_{(4)}$ check, whether the flexure attaches to the upper arm within a specified distance range $l = [0.05 \dots 0.3]$ m from the shoulder.

$$\mathbf{c}_{(3)} = l_{min} - l \quad (3.10)$$

$$\mathbf{c}_{(4)} = l - l_{max} \quad (3.11)$$

where l is the length of the arm link, i.e., of the respective beam element in the SPACAR model.

For the constraint $\mathbf{c}_{(5)}$ a self-intersection test is performed on the flexure. To this end, each line segment, given by the end nodes of the beam elements constituting the flexure, is checked for intersections with all other line segments. This procedure, which is described in detail in [65], yields the total number of self-intersections n_x .

$$\mathbf{c}_{(5)} = n_x \quad (3.12)$$

Constraint $\mathbf{c}_{(6)}$ determines whether the beam penetrates either the torso or the arm mesh. Each contact node j is assigned a value of $n_\epsilon = 1$, if it lies within at least one of the two meshes, and $n_\epsilon = 0$, if not. The sum of n_ϵ for all contact nodes yields the constraint value.

$$\mathbf{c}_{(6)} = \sum_{j=0}^m n_\epsilon \quad (3.13)$$

Analogously, the constraint $c_{(7)}$ determines whether the beam lies outside both offset meshes. Each contact node is assigned a value of $n_{\notin} = 1$, if it lies outside both the torso and arm offset mesh, and $n_{\notin} = 0$, if not. However, in the scope of this constraint only the first four contact nodes of the beam element at the back interface are checked, to ensure the flexure starts within the protrusion limit.

$$c_{(7)} = \sum_{j=0}^4 n_{\notin} \quad (3.14)$$

The first three penalties directly correspond to the constraints $c_{(3)}$, $c_{(4)}$ and $c_{(5)}$, whereby the respective constraint values are evaluated for each load step i and added in case they are positive. Penalties $p_{(1)}$ and $p_{(2)}$ shall prevent the interface point from sliding outside the specified range from the shoulder, when the arm link acts as a slider.

$$p_{(1)} = \sum_{i=0}^n l_{min} - l \quad \forall \quad l_{min} - l > 0 \quad (3.15)$$

$$p_{(2)} = \sum_{i=0}^n l - l_{max} \quad \forall \quad l - l_{max} > 0 \quad (3.16)$$

Penalty $p_{(3)}$ shall prevent self-intersections throughout the full deformation range of the flexure.

$$p_{(3)} = \sum_{i=0}^n n_{\times} \quad (3.17)$$

Penalties $p_{(4)}$ and $p_{(5)}$ are an extension to the constraints $c_{(6)}$ and $c_{(7)}$. In addition to evaluating whether a node lies within the torso and arm mesh or outside the offset meshes, the penetration depth and protrusion distance are evaluated for each respective node, as to provide a more continuous change in the cost function. For both $p_{(4)}$ and $p_{(5)}$ this evaluation is carried out for all contact nodes. However, while the penetration depth is considered for the entire range of motion, the protrusion is only taken into account for the lower elevation angles $\theta \leq \frac{\pi}{2}$ which are most critical for ADLs [48].

$$p_{(4)} = \sum_{i=0}^n \sum_{j=0}^m |d| \quad \forall \quad n_{\in} = 1 \quad (3.18)$$

$$p_{(5)} = \sum_{i=n/2}^n \sum_{j=0}^m d \quad \forall \quad n_{\notin} = 1 \quad (3.19)$$

where d is the shortest distance to either the torso or the arm mesh and index j denotes each contact node. By convention, d is signed negative when pointing inside the mesh and positive when pointing outside.

The last regular penalty $\mathbf{p}_{(6)}$ returns the value by which the von Mises stress exceeds the stress limit σ_{lim} . The von Mises stress in each beam element constituting the flexure is determined for each load step, and the highest overall value is assigned to σ_{Mises} .

$$\mathbf{p}_{(6)} = \begin{cases} 0, & \text{if } \sigma_{Mises} - \sigma_{lim} \leq 0 \\ \sigma_{Mises} - \sigma_{lim}, & \text{if } \sigma_{Mises} - \sigma_{lim} > 0 \end{cases} \quad (3.20)$$

$$\sigma_{lim} = \frac{\sigma_t}{FOS} \quad (3.21)$$

where σ_t is the tensile stress of the flexure material and $FOS = 1.2$ the applied factor of safety.

As stated previously, the objective δ of the first optimization is turned into a penalty for the second optimization. To this end, a conditional extra penalty $\mathbf{p}_{(7)}^*$ applies only during that second optimization.

$$\mathbf{p}_{(7)}^* = \begin{cases} 0, & \text{if } \delta - \delta_{lim} \leq 0 \\ \delta - \delta_{lim}, & \text{if } \delta - \delta_{lim} > 0 \end{cases} \quad (3.22)$$

where $\delta_{lim} = 0.05$ is the limit on the gravity balancing error.

The two cost functions $f_1(\mathbf{x})$ and $f_2(\mathbf{x})$ are optimized sequentially using the *particleswarm()* solver from the MATLAB Global Optimization Toolbox, whereby the optimized parameter set of the first optimization serves as the initial point for the second optimization.

3.2.9 Investigation Scheme

Using this optimization routine, mechanism designs for every feasible combination of support conditions are optimized. First, all combinations of support conditions are investigated which feature either only approximately zero or infinite stiffness at each joint. Hence, no joint stiffness parameters are optimized. However, since these designs rely on storing all their energy in the flexure, only designs with a mobility of the flexure of ≤ 0 are considered. Consequently, combinations with ≥ 3 degrees of freedom and with two sliders are excluded. The latter, is due to the kinematic singularity that occurs when both sliders are parallel. This leaves 10 feasible out of 16 possible combinations.

Next, all combinations of support conditions are investigated for which a stiffness parameter is assigned to each released joint, i.e., when considering only a finite or infinite stiffness at each joint. Each assigned stiffness parameter becomes part of the parameter set, and thus is optimized along with the flexure shape. In this case no mobility issues arise, making all combinations feasible. However, since the case with infinite stiffness in all joints is already covered only 15 additional combinations are considered, making it in total 25 different support conditions that are investigated. An overview of the investigated support conditions is given in Table 3.1.

Table 3.1: Overview of feasible support conditions

		Back			
		Clamp	Hinge	Slider	Slider/ Hinge
DOF		0	1	1	2
Arm	Clamp	✓	✓	✓	✓
	Hinge	✓	✓	✓	(✓)*
	Slider	✓	✓	(✓)*	(✓)*
	Slider/Hinge	✓	(✓)*	(✓)*	(✓)*

★: only feasible when considering stiffness in at least one joint

For each of the different support conditions the optimization routine is conducted at least 51 times, and on average 65 times. During this process the maximum allowed protrusion, affecting the offset mesh and thus penalty $p_{(5)}$, is alternated between the values $o = [75, 100, 150]$ mm. Based on this broad investigation the combinations of support conditions that yield feasible results are identified.

These feasible mechanisms are subsequently categorized regarding their kinematic behavior at each interface, and for each category two representative designs are chosen and dimensioned. PA2200 with a Young's modulus of $E = 1.7$ GPa, a tensile stress of $\sigma_t = 50$ MPa and a density of $\rho = 930$ kg/m³ is used as flexure material, and the maximum flexure thickness is limited to 25 mm. By adjusting the flexure width and joint stiffnesses, a moment amplitude of 10 Nm is set for every example mechanism. This provides a comparison between the different categories of feasible mechanisms. Subsequently, two of those categories are selected for further investigation. For these more targeted optimizations are conducted, yielding the improved flexure mechanism designs that are then experimentally evaluated.

3.3 EXPERIMENT

Following the investigation scheme physical prototypes for the two improved flexure mechanism designs, labeled **A** and **B**, are made and tested on a dedicated test bench. The test bench is designed to emulate the conditions in the simulation, and thereby validate both the angle-dependent stiffness behavior and the alignment with the body.

Due to the different support conditions, prototype **A** and prototype **B** require different test bench configurations. The test bench as configured for prototype **B** is shown in Figure 3.2, while the configuration for prototype **A** is shown in the *Results* section Figure 3.10. For the structural components 40×40 mm aluminum profiles and 3 mm steel plate are used, while a 25 mm thick aluminum plate serves as the base. The tested flexure prototypes, the arm and torso shells, as well as the hub of the shuttle assembly are made from laser-sintered PA2200. Due to size limitations imposed by the laser sintering machine both flexures are split into two parts.

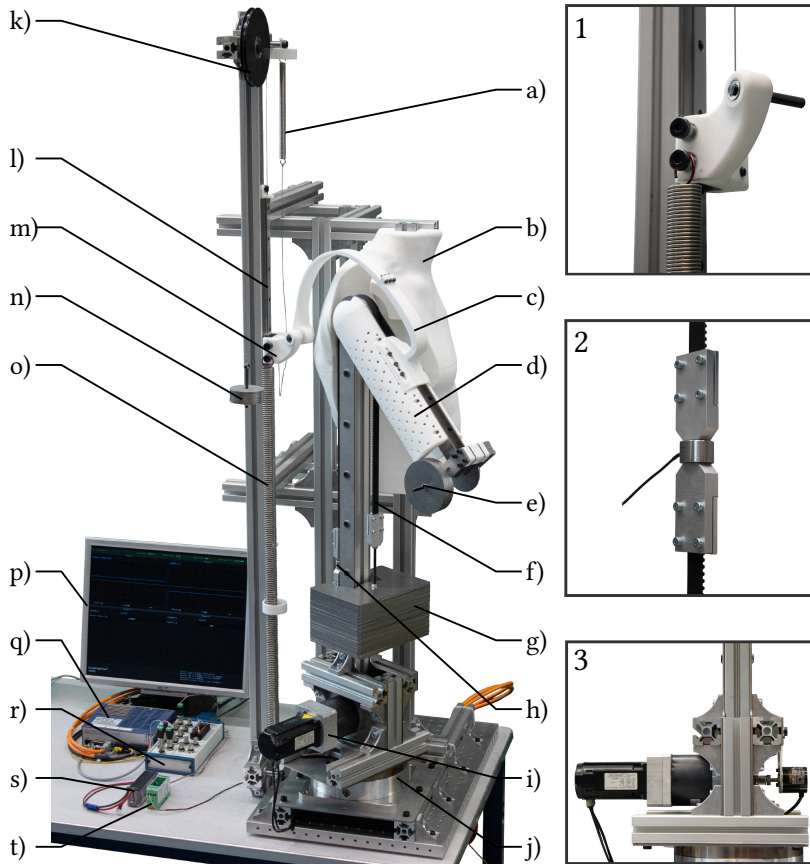


Figure 3.2: Experimental setup, configuration **B**. a) secondary spring (connected to the shuttle via a string), b) torso shell, c) flexure specimen (prototype **B**), d) arm shell, e) balance weight, f) timing belt, g) counterweight, h) force sensor assembly, i) actuator (motor and gearbox), j) rotary stage, k) pulley, l) linear guide, m) shuttle assembly, n) shuttle counterweight, o) primary spring, p) Simulink Real-Time scope, q) motor driver, r) NI adapter, s) battery, t) measuring amplifier. Detail 1: shuttle assembly without specimen; Detail 2: force sensor assembly; Detail 3: auxiliary view showing the position of the encoder, connected to the actuator output via a bellows coupling.

The arm consists of two parallel steel plates to which two shells with mounting holes are attached. At the distal end both plates are connected, and an adjustable balance weight is fixed to set the moment amplitude. The weight can be shifted to align the arm's center of gravity with the arm axis.

At the proximal end both plates are connected to a timing pulley which is mounted to the top of a pole via two ball bearings. Below the pole a second timing pulley is located and fixed to the output of a Neugart PLE080 gearbox which is driven by a Kollmorgen AKM22C motor. The motor is powered and controlled via a Kollmorgen

S20260-VTS servo drive. Opposite to the gearbox a YUMO E6B2-CWZ3E digital quadrature encoder is connected to the same output through a bellows coupling.

Both timing pulleys are connected via an open timing belt. The belt is clamped to the lower pulley, runs over the top pulley and extends back down where it connects to an adjustable counterweight. In between the two pulleys the belt is interrupted by an assembly consisting of two clamps and a ME-Meßsysteme KM26z load cell. The signals from the load cell are amplified by a ME-Meßsysteme GSV-11H 010-5/20/2 measuring amplifier, using a battery for power supply.

The entire assembly rests on a rotary stage, that can be used to set the horizontal flexion/extension angle γ . A separate frame serves as the mount for the prototype's back interfaces and the torso reference shell.

Prototype **A** consists of three major parts. The first part of the flexure containing the back interface, is simply bolted to the frame. It is connected to the second part of the flexure via a flange, which is bolted and reinforced with instant adhesive. At its other end, the second part of the flexure is mounted via a shaft to a ball bearing which is contained in the the arm interface. This hinged interface in turn is bolted to the arm shells via two slotted holes.

Prototype **B**, shown in Figure 3.2 features a more complex design. A shuttle which incorporates a sliding block, bolts for connecting springs and counterweights, as well as a shaft supported by two ball bearings constitutes the back interface of this design. The sliding block runs in a linear track, which is fixed to a long aluminum profile that is attached to the frame. To set the bi-directional stiffness of the translational degree of freedom two tension springs are used. The main spring covers most of the range of motion and is fixed between the lower end of the aluminum profile and the shuttle. The secondary spring is suspended from the top of the profile and connected to the shuttle via a string which disengages the spring when not in use. In addition to the springs, another string connects the shuttle to a counterweight, which is suspended from a pulley at the top of the aluminum profile. It is used to adjust the effective weight of the shuttle assembly to the value set in simulation. The first part of the flexure is fixed to the shaft of the shuttle and connects to the second part of the flexure in the same way as prototype **A**. That second part containing the arm interface is then directly fixed to the arm shells.

The entire setup is controlled and the sensor readings obtained via Simulink Real-Time. To this end, a PC with a National Instruments PCI-6221 multifunction I/O card and a National Instruments BNC-2110 adapter are used. During experiments the arm is raised from the lowest position $\theta = 0$ to the raised position $\theta = \pi$, and lowered back to the lowest position using a constant speed. The signals are acquired at a rate of 100 Hz and the force signal is filtered using a moving average filter with a window size of 20 samples. Each configuration is measured with and without the flexure. The two measurements are then subtracted from each other to isolate the mechanical behavior of the flexure mechanism. Multiplying the force data with the partial diameter of the timing pulley at the arm yields the shoulder moment. In the absence of an absolute zero reference for the force signal, the moment offset is adjusted such that the zero crossing for the unstressed state at which the mechanism is assembled matches the simulation.

3.4 RESULTS

A total number of 1616 optimizations is conducted, resulting in 204 feasible mechanism designs. These are found for 18 of the 25 investigated support conditions. All support conditions yield feasible results for finite joint stiffnesses. However, only three achieve a balancing behavior below the threshold of $NMEA \leq 0.05$ when considering no stiffness at the released joints.

Each of the feasible mechanisms is categorized by the amount of displacement displayed at each joint. Accordingly, the label *Clamp*, *Slider*, *Hinge* or *Slider/Hinge* is assigned to each interface. Thereby, 10 feasible categories of mechanisms are found that correspond to the 16 possible kinematic combinations shown in Table 3.1. The other 6 kinematic combinations are avoided in optimization by assigning high stiffnesses to some of the released joints. Consequently, these joints display no significant motion, making them behave as if rigid or absent.

Out of each feasible category two designs are chosen as representative examples, and dimensioned for an amplitude of 10 Nm. Animations of these two examples, labeled 1 and 2, for each category can be seen in Figures 3.3 to 3.7. The categories are named by first stating the condition at the arm interface and then, separated by a dash, at the back interface.

The three kinematic categories that work without considering finite stiffnesses are the first three shown in Figures 3.3 and 3.4. They feature either two clamped interfaces, or one clamped and one hinged interface. The chosen examples for these three categories all feature approximately zero stiffness in the joints. All other categories require finite joint stiffnesses in order to work. Some rely solely on the interfaces for their function, using the flexure as a structural element. An example for this is the *Slider/Hinge–Hinge* category in which both designs resemble the inverse slider-crank mechanism described by Kim *et al.* [30].

The *Hinge–Clamp* and the *Clamp–Slider/Hinge* categories are chosen for further investigation. **A** is obtained by re-optimizing the *Hinge–Clamp* category with no hinge stiffness. For **B** the stiffness of the back hinge is set to zero, while a constant stiffness of 100 N/m is assigned to the back slider, when re-optimizing the *Clamp–Slider/Hinge* category. The prototypes for **A** and **B** were accidentally dimensioned only on basis of the stresses at the last load step. Consequently, they surpass the stress limit by 1.9 MPa and 10.8 MPa, respectively, when considering the entire range of motion. However, this did not lead to failure or any other observed negative consequences. To provide an accurate comparison with the other examples, corrected values for beam dimensions observing the stress limit are given in brackets.

A comparison between the computed performance metrics of the prototypes and the two examples of each kinematic category is given in Table 3.2. Since the mechanisms in this study are all designed for a moment amplitude of 10 Nm, the relative shear force represents 10 % of the absolute maximum shear force. Graphs showing the optimized angle-dependent balancing behavior for **A** and **B** are shown in Figure 3.8. Corresponding graphs for all other examples are provided in supplementary file 1.

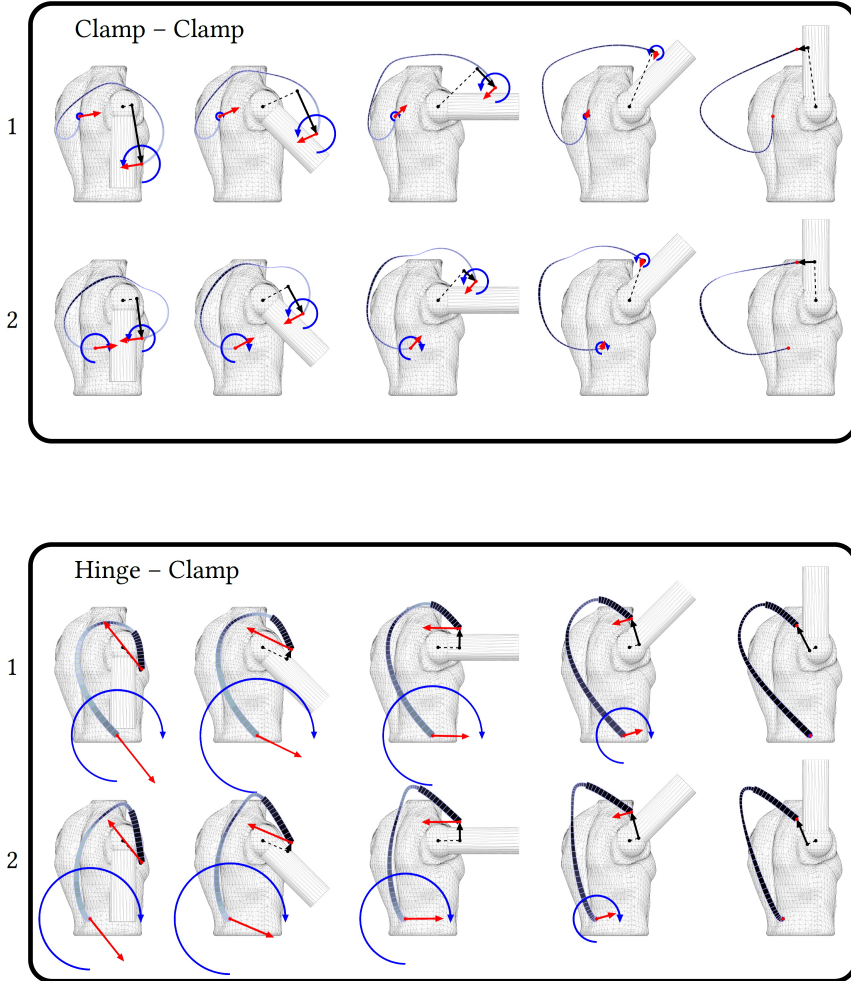


Figure 3.3: Animations of the example mechanisms of the kinematic categories *Clamp-Clamp* and *Hinge-Clamp*. Red arrows are proportional to reaction forces (1 mm/N), the blue arrow's radii to reaction moments (33 mm/Nm). Black arrows depict the lever arm of the arm interface force with respect to the shoulder joint, marked by a dot. A perpendicular dashed line connects the lever arm arrow and shoulder joint.

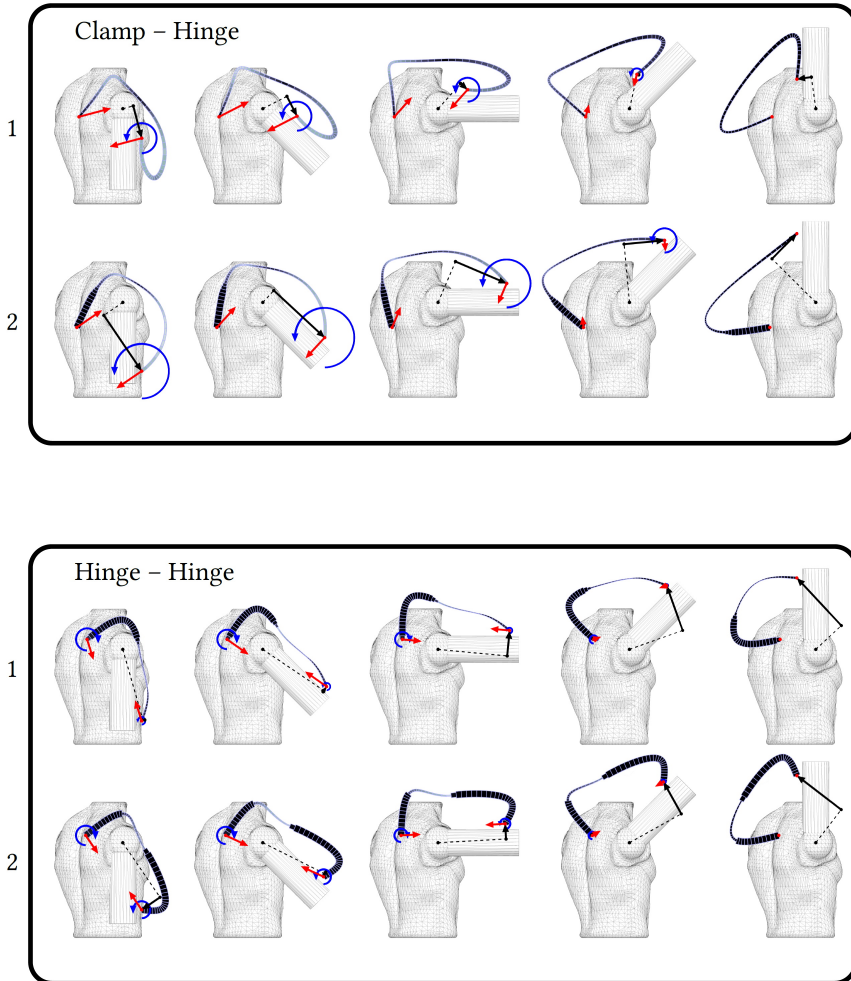


Figure 3.4: Animations of the example mechanisms of the kinematic categories *Clamp-Hinge* and *Hinge-Hinge*. Red arrows are proportional to reaction forces (1 mm/N), the blue arrow's radii to reaction moments (33 mm/Nm). Black arrows depict the lever arm of the arm interface force with respect to the shoulder joint, marked by a dot. A perpendicular dashed line connects the lever arm arrow and shoulder joint.

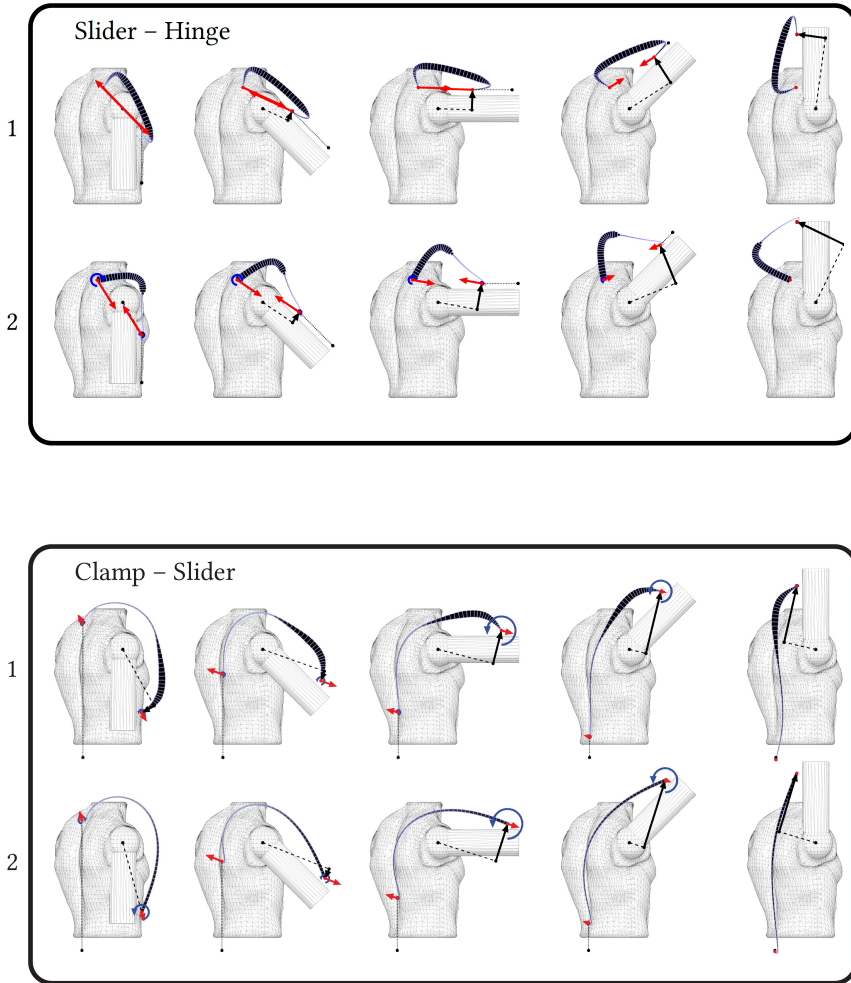


Figure 3.5: Animations of the example mechanisms of the kinematic categories *Slider-Hinge* and *Clamp-Slider*. Red arrows are proportional to reaction forces (1 mm/N), the blue arrow's radii to reaction moments (33 mm/Nm). Black arrows depict the lever arm of the arm interface force with respect to the shoulder joint, marked by a dot. A perpendicular dashed line connects the lever arm arrow and shoulder joint. Dotted lines show slider displacements from the initial positions marked by dots.

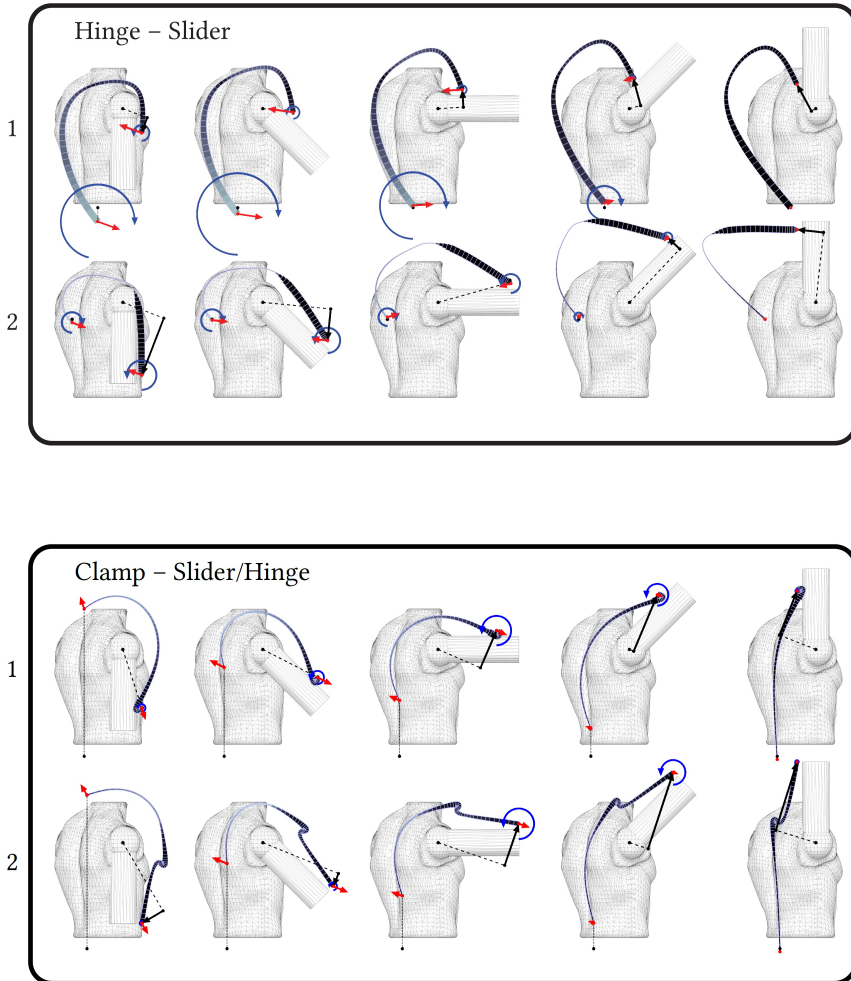


Figure 3.6: Animations of the example mechanisms of the kinematic categories *Hinge-Slider* and *Clamp-Slider/Hinge*. Red arrows are proportional to reaction forces (1 mm/N), the blue arrow's radii to reaction moments (33 mm/Nm). Black arrows depict the lever arm of the arm interface force with respect to the shoulder joint, marked by a dot. A perpendicular dashed line connects the lever arm arrow and shoulder joint. Dotted lines show slider displacements from the initial positions marked by dots.

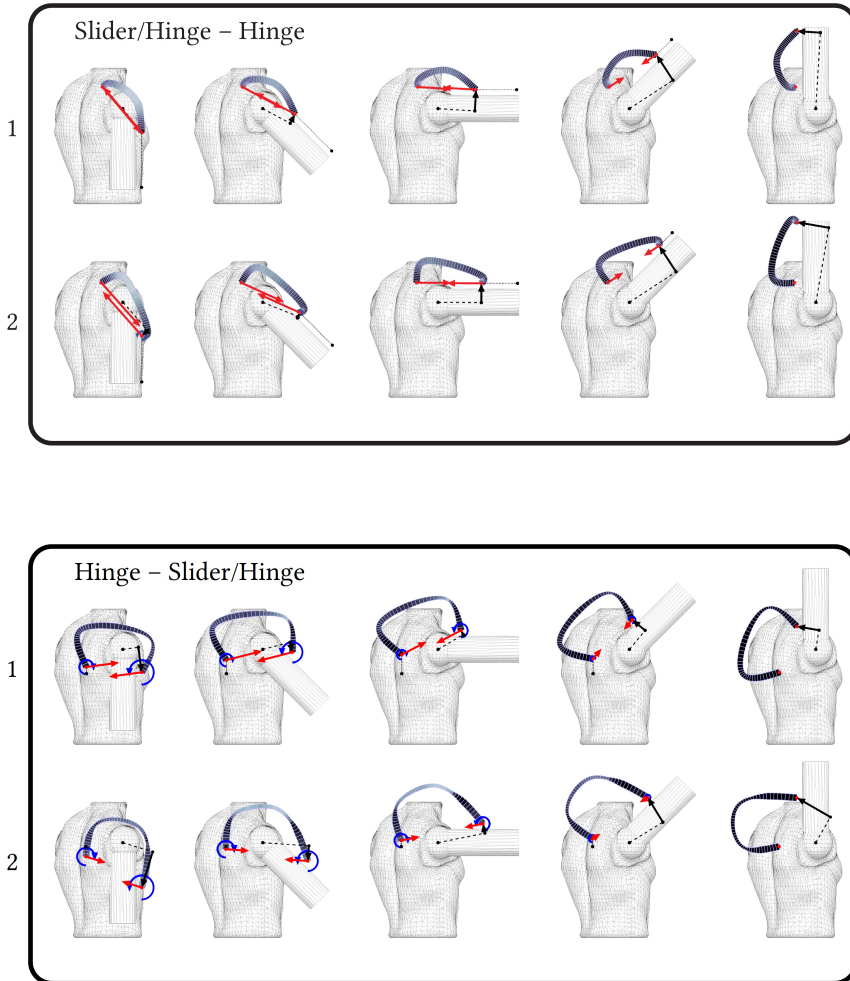


Figure 3.7: Animations of the example mechanisms of the kinematic categories *Slider/Hinge-Hinge* and *Hinge-Slider/Hinge*. Red arrows are proportional to reaction forces (1 mm/N), the blue arrow's radii to reaction moments (33 mm/Nm). Black arrows depict the lever arm of the arm interface force with respect to the shoulder joint, marked by a dot. A perpendicular dashed line connects the lever arm arrow and shoulder joint. Dotted lines show slider displacements from the initial positions marked by dots.

Table 3.2: Performance metrics

		Balancing Error δ	Relative Strength ϵ	Maximum Protrusion	Relative Shear Force
		-	Nm/cm	cm	N/Nm
A		0.0440	2.58	18.40	-16.63
<i>Hinge-Clamp</i>		(0.0440)	(2.27)	(18.51)	(-16.63)
B		0.0435	3.33	9.96	+6.61
<i>Clamp-Slider/Hinge*</i>		(0.0434)	(1.68)	(11.02)	(+6.65)
Clamp-Clamp	1	0.0419	1.23	29.15	-4.54
	2	0.0433	0.94	29.69	-4.22
Hinge-Clamp	1	0.0413	5.11	17.03	-18.29
	2	0.0454	3.77	20.62	-16.56
Clamp-Hinge	1	0.0462	3.43	21.59	-6.57
	2	0.0455	1.98	26.71	+6.39
Hinge-Hinge*	1	0.0410	4.34	21.03	-9.67
	2	0.0443	5.50	19.67	-8.78
Slider-Hinge*	1	0.0500	1.60	11.63	-17.74
	2	0.0511	0.34	22.61	-11.34
Clamp-Slider*	1	0.0574	0.74	14.71	+5.93
	2	0.0723	0.94	13.53	+6.09
Hinge-Slider*	1	0.0495	8.39	21.43	-8.46
	2	0.0443	1.45	35.14	-5.06
Clamp-Slider/Hinge*	1	0.0392	1.96	12.26	+5.84
	2	0.0379	1.36	12.91	+5.66
Slider/Hinge-Hinge*	1	0.0401	28.94	10.62	-16.86
	2	0.0417	25.1	11.24	-16.77
Hinge-Slider/Hinge*	1	0.0377	8.73	13.98	-9.48
	2	0.0372	21.85	19.85	-7.39

*feasible results only for beam support conditions with finite stiffness values.

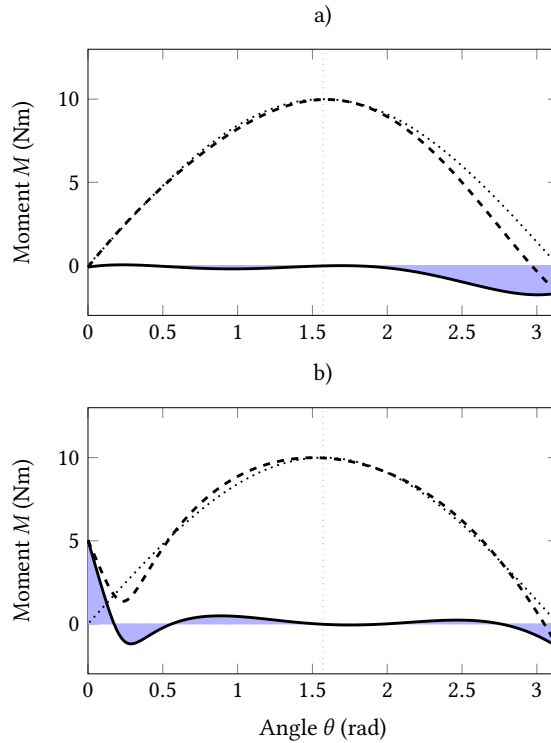


Figure 3.8: Optimized balancing behavior of a) **A** and b) **B**. The dashed line depicts the computed moment generated by the mechanism. The dotted line shows the ideal characteristic, i.e., the inverse of the load moment. The solid line shows the balanced behavior of the mechanism, when adding the load moment to the mechanism's moment. The shaded areas indicate the balancing error. This diagram shows good balancing behavior for both prototypes throughout the range of motion. **A** shows progressively imbalanced behavior towards the raised position, while **B** shows a sudden deviation at smaller angles.

The construction parameters for the flexures employed in **A** and **B** are given in Table 3.3 in the appendix. Corresponding tables for all other examples along with information about the joint stiffnesses and ranges of motion are provided in supplementary file 2. Table 3.4 in the appendix shows the energy distribution between the flexure and the individual joints at $\theta = 0$.

Movies showing the full animations of all simulated mechanisms shown in juxtaposition to the balancing graphs are provided in supplementary file 3.

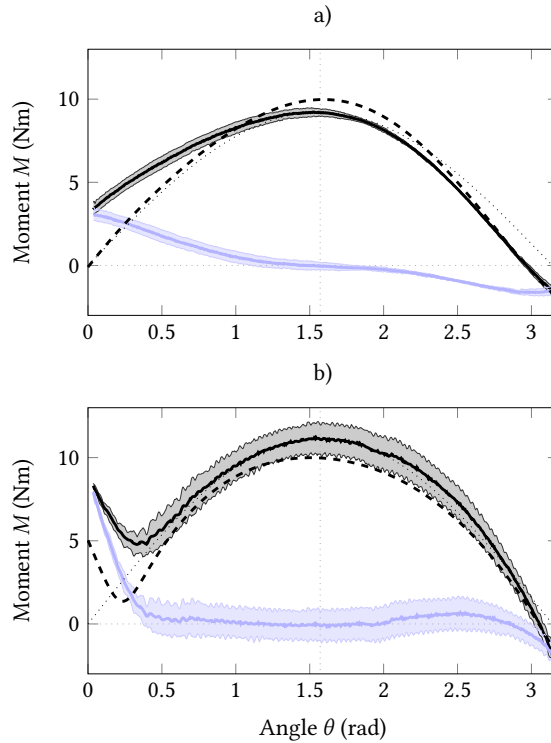
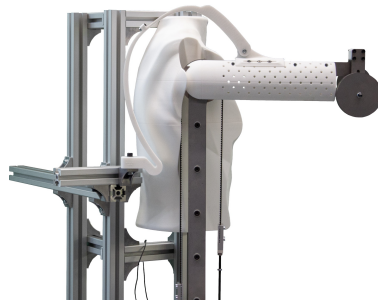
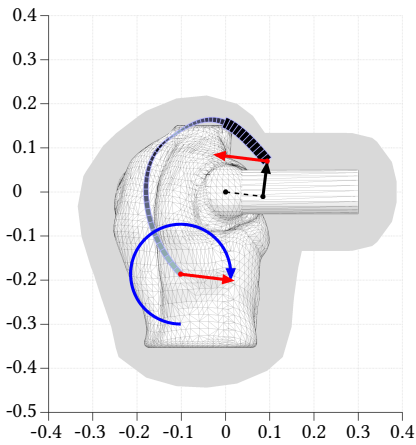
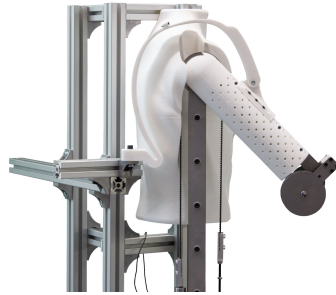
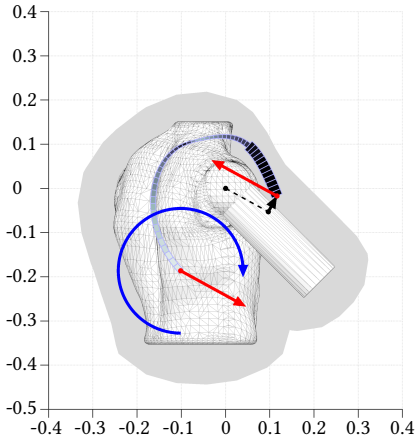
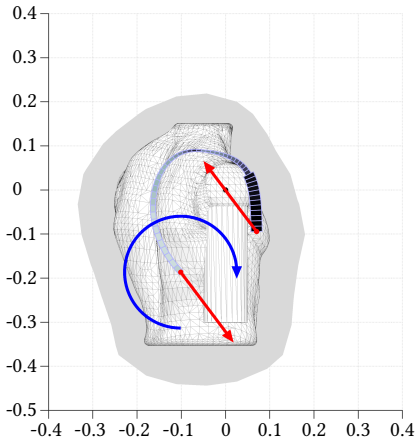


Figure 3.9: Experimental results for a) prototype **A** and b) prototype **B**. The thin black solid line depicts the measured moment exerted by the mechanism. The thick black solid line depicts the mean and the shaded area in between indicates the hysteresis. A sine curve matching the maximum amplitude of the measured mean is depicted by the black thin dotted line. The balanced moment characteristic, i.e., the difference between the sine curve and measured data, is analogously depicted in light blue. The corresponding simulation result is shown by the dashed line. In comparison to the computed results, prototype **A** shows additional progressively imbalanced behavior towards smaller angles. For prototype **B** the sudden deviation from balanced behavior at smaller angles occurs earlier. Furthermore, both results show a mismatch in amplitude of -0.78 Nm and $+1.2$ Nm for **A** and **B**, respectively. Prototype **B** exhibits significantly more hysteresis than prototype **A**.

The results of measurements performed at $\frac{\pi}{60}$ rad/sec are shown in Figure 3.9.

The animations of **A** and **B** in juxtaposition to photographs of the experiment are shown in Figures 3.10 and 3.11. Corresponding movies showing the full animation and photo time lapse alongside the respective graphs are provided in supplementary files 4 and 5.

Movies showing the experiment of **A** and **B** from several different angles are provided in supplementary files 6 and 7.



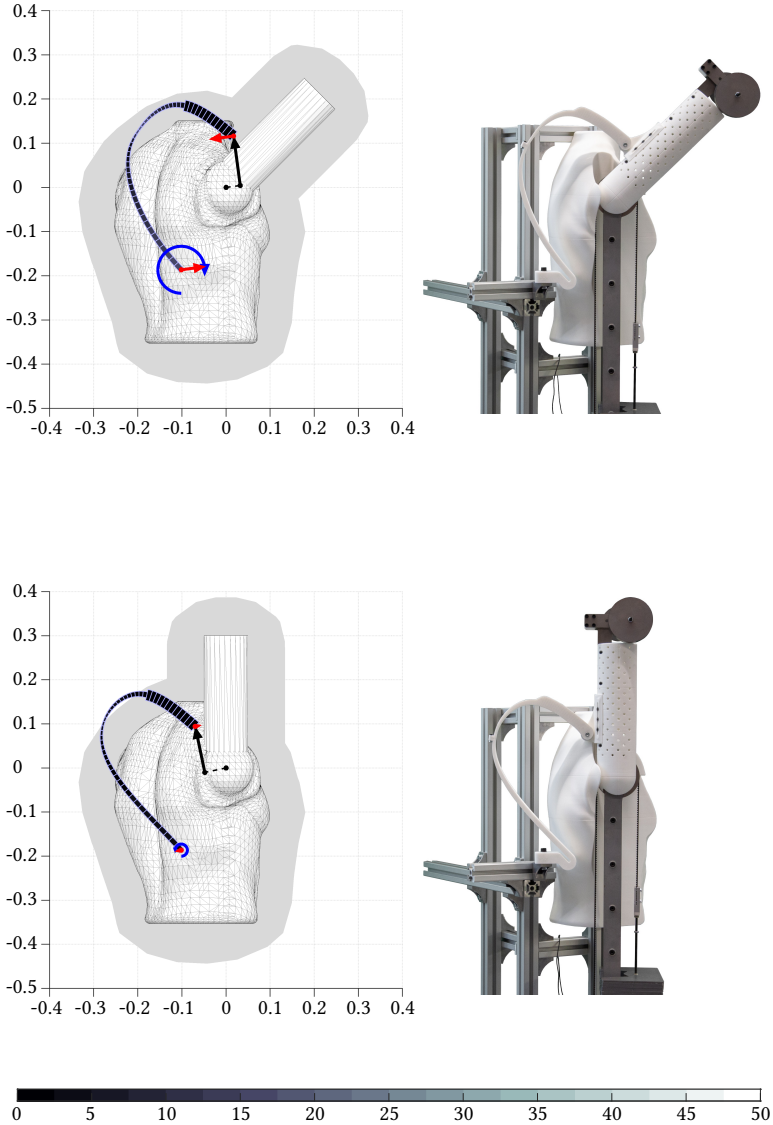
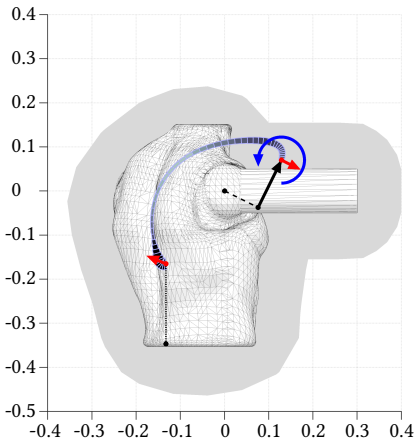
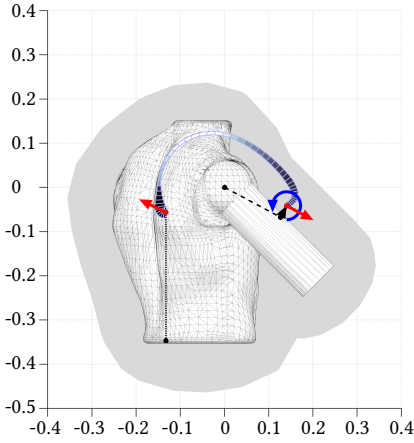
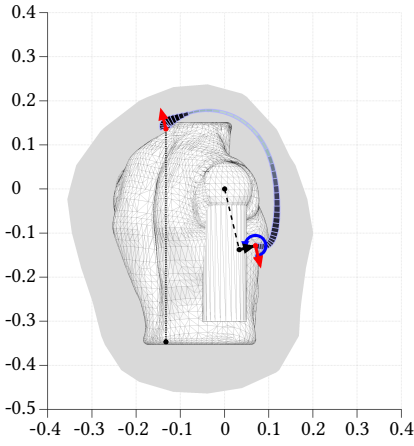


Figure 3.10: Juxtaposition of animation and photographs from the experiment, of **A**. Axes are in m, color scale is in MPa. The remaining description of the animation is equal to Figures 3.3 to 3.7.



3

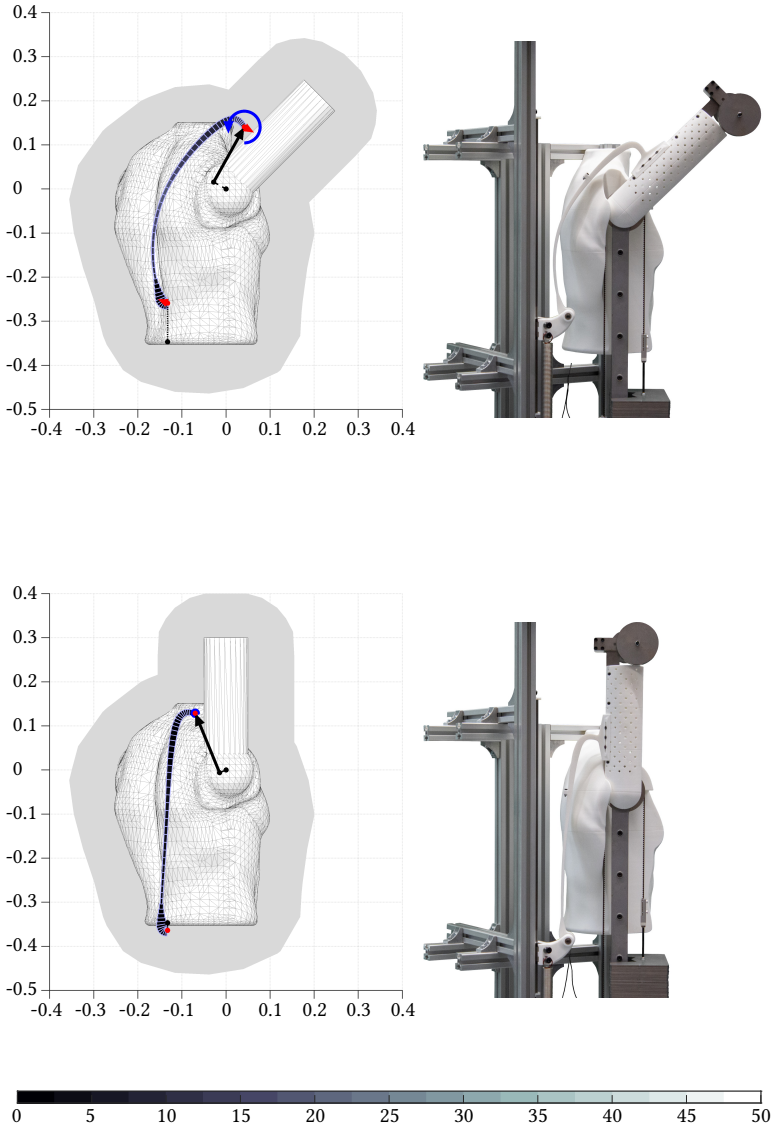


Figure 3.11: Juxtaposition of animation and photographs from the experiment, of **B**. Axes are in m, color scale is in MPa. The remaining description of the animation is equal to Figures 3.3 to 3.7. The shuttle counterweight and secondary spring are removed as not to obstruct the view on the flexure.

3.5 DISCUSSION

A large variety of different mechanisms was found that fulfill both the requirements regarding gravity balancing and collision avoidance. These can be categorized by their apparent kinematic behavior as shown in Figures 3.3 to 3.7, but also by the way they achieve gravity balancing and the degree to which they utilize the flexure.

When considering the force and moment at the arm interface, as can be seen in Figures 3.3 to 3.7, there are three ways of achieving gravity balancing. Mechanisms that feature no significant moment at the arm can only utilize the interface force for balancing. At the raised position they start with a small force, but large lever arm. As the arm moves down the force increases while the lever arm decreases, creating the sine-shaped moment at the shoulder joint. At the lowest position the force points directly at the shoulder joint to achieve a zero moment. Examples for this behavior are the categories *Hinge-Clamp*, *Slider-Hinge* and *Slider/Hinge-Hinge*. As for their functioning the force vector has to stay mostly parallel to the arm, these three categories feature larger relative shear forces than all other categories.

Mechanisms that feature a progressively increasing arm interface moment towards lower angles have to use the interface force to counteract it. As the arm moves from the raised position to the lowered position the moment arm is growing in opposite direction, often flipping its orientation relative to the shoulder. At lower angles the force vector points mostly perpendicular to the arm. Examples for this are the categories *Clamp-Clamp*, *Clamp-Hinge*, *Hinge-Slider* and *Hinge-Slider/Hinge*.

Lastly, mechanisms that can modulate the moment at the arm interface, can achieve balancing irrespective of the force. For this type of behavior the location of the back interface has to change significantly. Consequently, a slider with large stroke at the back is required. Examples for this are the *Clamp-Slider* and *Clamp-Slider/Hinge* categories. These type of mechanisms have the lowest interface forces.

When considering the energy distribution shown in Table 3.4 the mechanisms can, again, be divided into three different types. The first type uses only the flexure for energy storage. It corresponds to the three categories *Clamp-Clamp*, *Hinge-Clamp* and *Clamp-Hinge* for which results were found, when no joint stiffness is considered.

The second type is a hybrid which uses both the flexure and interfaces for storing energy. Mechanisms of this type feature up to two joints, of which one is used for energy storage. They belong to the categories *Clamp-Slider*, *Hinge-Slider* and *Clamp-Slider/Hinge*.

The third type nearly exclusively uses the joints for energy storage. In these cases the flexure is reduced to a means of transmission. For that reason this type was not considered for further investigation in this study. This pertains to the categories *Hinge-Hinge*, *Slider-Hinge*, *Slider/Hinge-Hinge* and *Hinge-Slider/Hinge*.

For A the *Hinge-Clamp* category was chosen, as one of the designs that utilizes only the flexure for energy storage. It, therefore, offers low complexity and a small number of parts. In comparison to the *Clamp-Clamp* and *Clamp-Hinge* categories it shows the best potential for close-to-body alignment and relative strength. Though the maximum protrusion is relatively high, it drops steadily from 18 cm at $\theta = \pi$, below

10 cm at $\theta = \frac{\pi}{2}$, and down to 6 cm at $\theta = 0$. However, the large shear force at the arm and very large moment at the back interface are the two main disadvantages of this design. In addition, the experiments indicate that purely force-based gravity balancing may be more sensitive to disturbances. Due to the small lever arm the orientation of the force vector with respect to the shoulder has to be very precise in order to function properly. The results indicate that with increasing stress and deformation in the system, this may be hard to achieve causing the progressive deviation between simulation and experiments towards smaller angles, as shown in Figure 3.9. Therefore, in retrospect, the *Clamp-Hinge* category may be the better choice out of the three flexure-only categories.

For **B** the *Clamp-Slider/Hinge* category was chosen. As one of the hybrid types it is more complex, but offers the best theoretical performance out of the flexure-based designs. In addition, the way the mechanism aligns with the body and the low reaction forces and moments appear very advantageous. In comparison to **A** the protrusion remains more steady, dropping from 10 cm at $\theta = \pi$, down to 7 cm for the range between $\theta = 2$ to $\theta = 0.5$, and going back up to 10 cm at $\theta = 0$. In comparison to the very similar *Clamp-Slider* category the additional hinge at the back yields performance gains throughout all metrics. By observation of the energy distribution and stiffnesses, it was concluded that for this prototype design predefined stiffness values can be assigned to the joints. Thereby, the search space for the optimization was reduced and the construction simplified. Considering the measurement data shown in Figure 3.9 the balancing behavior seems more robust than that of prototype **A**, showing larger qualitative divergence only at angles below 0.5 rad. At these smaller angles also a positional deviation of the back interface between simulation and experiment occurs, as can be seen in Figure 3.11. However, this is in part caused by the missing counterweight.

All mechanisms found in this study exhibit a maximum protrusions of at least 10 cm. Hence, modifications to the synthesis method are likely required to further improve the alignment with the body and reduce protrusion. The joint-centric designs may be improved by replacing the flexure element by a structure or mechanism which aligns laterally to the body, as is done in the ShoulderX [67] which shares similarities with the *Slider/Hinge-Hinge* designs.

For the flexure-based designs the *Clamp-Slider/Hinge* category seems to offer the best prospects. Potential ways of improving the alignment to the body may include the investigation of nonlinear tracks for the slider that conform better to the body, active guidance of the flexure, e.g., with rollers, allowing contact with the body, as well as the investigation of spatial flexure designs that connect laterally to the arm. In addition, the balancing error at lower angles needs to be addressed, and though out-of-plane behavior is not explicitly investigated, a vertical pivot to facilitate horizontal flexion/extension will likely be required.

In preparation to this study contact with the body and spatial flexure designs have already been investigated. However, the high computational cost for the contact analysis and the largely increased search space when considering additional bending and torsion deformation angles of the flexure were reasons to exclude these aspects from this study.

3.6 CONCLUSIONS

This study aimed to find a close-to-body gravity-balancing flexure-based mechanism for shoulder support that may be used without any additional rigid linkages between the torso and the arm. A broad optimization study into different kinematic support conditions revealed a multitude of possible designs – many of which are left for further investigation.

Of the two designs that were developed into prototypes and evaluated in experiment both show good gravity balancing behavior. Prototype **A** reduces the required maximum moment to lift the arm by more than 80 % over the entire simulated, and 85 % of the measured range of motion. Prototype **B** shows even better balancing qualities, offering the same more-than-80 % reduction over 97 % of the simulated, and 92 % of the measured range of motion. In addition, design **B**, having the lowest protrusion out of all flexure-based designs, features a maximum protrusion that is 46 % less than that of design **A**. Furthermore, the low interface forces and moments of design **B**, which are over 60 % lower compared to design **A**, are potential key enablers for a fully compliant exoskeleton structure. Therefore, a design with a spring loaded slider and a hinge at the back of the wearer, and a tapered flexure connecting it to the upper arm appears to be the most promising solution for the proposed exoskeleton architecture.

Though it seems feasible that in terms of size and protrusion the current design **B** could already compete with the mechanisms employed in commercially available shoulder supports, the device is still far from the aspired 3 cm distance to the body. Possible leads to mitigate this shortcoming in future work are provided. Aside from this, however, additional work will be necessary to translate the test bench prototype mechanism into a wearable assistive device. To this end, better integration, simplification and customization of all components will be the main challenges.

3.7 APPENDIX

3.7.1 Tables

Table 3.3: Flexure parameters

Parameter	Unit	A	B
s_x	mm	-101.4	-132.6
s_z	mm	-186.4	-346.6
l_1	mm	309.6	13.5
l_2	mm	127.8	468
l_3	mm	155.2	42.4
φ_1	rad	2.145	2.666
φ_2	rad	0.9105	1.4635
φ_3	rad	-0.4639	0.2735
t_1	mm	12.5 (12)	47.9 (38.1)
t_2	mm	11 (10.6)	5.2 (4.2)
t_3	mm	4.4 (4.2)	8 (6.3)
t_4	mm	12.9 (12.4)	16.1 (12.8)
t_5	mm	197.6 (189.4)	12.2 (9.7)
w	mm	38.7 (44.1)	30 (59.5)

Table 3.4: Energy distribution at $\theta = 0$ on a percentage basis

		Flexure	Arm		Back	
			Slider	Hinge	Slider	Hinge
A						
<i>Hinge-Clamp</i>		100		0		
B						
<i>Clamp-Slider/Hinge</i>		39			61	0
Clamp-Clamp		1 2	100 100			
Hinge-Clamp		1 2	100 100	0 0		
Clamp-Hinge		1 2	100 100			0 0
Hinge-Hinge		1 2	4 5	13 25		83 71
Slider-Hinge		1 2	10 15	87 46		3 39
Clamp-Slider		1 2	56 61		44 39	
Hinge-Slider		1 2	42 36	55 63	4 1	
Clamp-Slider/Hinge		1 2	38 36		61 61	0 3
Slider/Hinge-Hinge		1 2	8 10	87 72	0 10	4 7
Hinge-Slider/Hinge		1 2	6 6	64 46	1 2	29 46

3.7.2 Supplementary Files

- **Supplementary file 1 – Additional_Graphs.pdf**
Graphs showing the angle-dependent balancing behavior for all example mechanisms, arranged by their kinematic categories.
- **Supplementary file 2 – Additional_Tables.pdf**
A table stating the flexure parameters and a table stating the joint stiffnesses and joint ranges of motion for all example mechanisms.
- **Supplementary file 3 – Simulations.mp4**
Movie showing the full animations of all simulated mechanisms shown in Figures 3.3 to 3.7, in juxtaposition to the graphs from supplementary file 1.
- **Supplementary file 4 – Prototype_A.mp4**
Movie showing the full animation and photo time lapse corresponding to Figure 3.10, in juxtaposition to the graphs in Figures 3.8 and 3.9 for design **A**.
- **Supplementary file 5 – Prototype_B.mp4**
Movie showing the full animation and photo time lapse corresponding to Figure 3.11, in juxtaposition to the graphs in Figures 3.8 and 3.9 for design **B**.
- **Supplementary file 6 – Prototype_A_Experiment.mp4**
Movie showing the experiment of **A** from several different angles.
- **Supplementary file 7 – Prototype_B_Experiment.mp4**
Movie showing the experiment of **B** from several different angles.

The downloadable supplementary materials are available at:

<https://research.utwente.nl>

Digital Object Identifier 10.3990/1.9789036551342

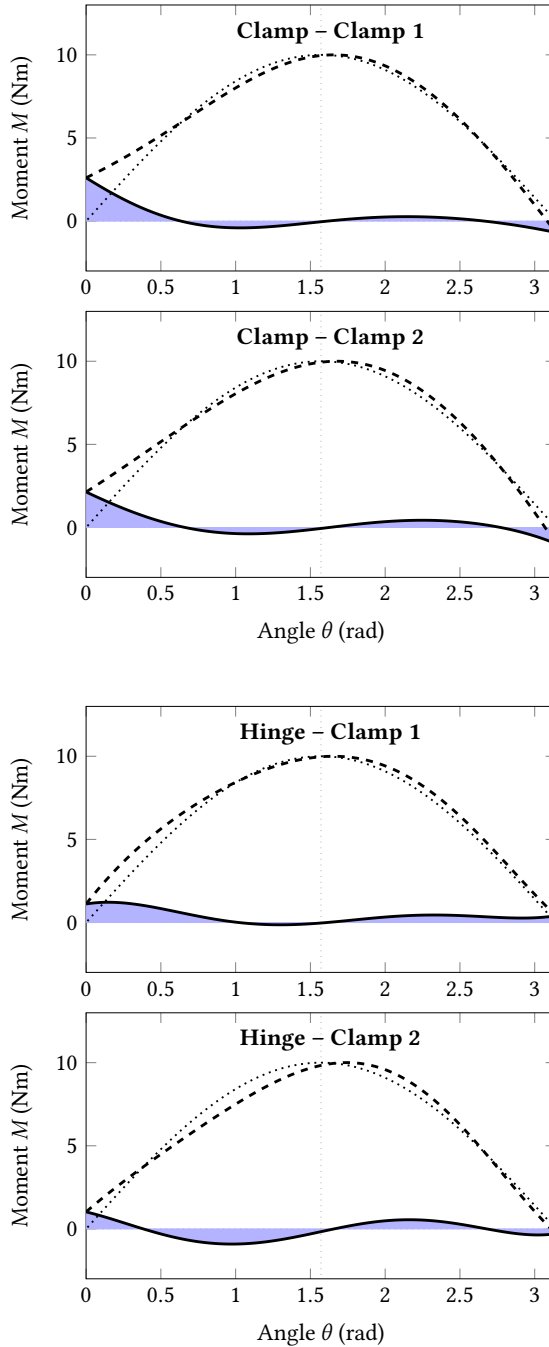
High image resolution movies (838 MB)

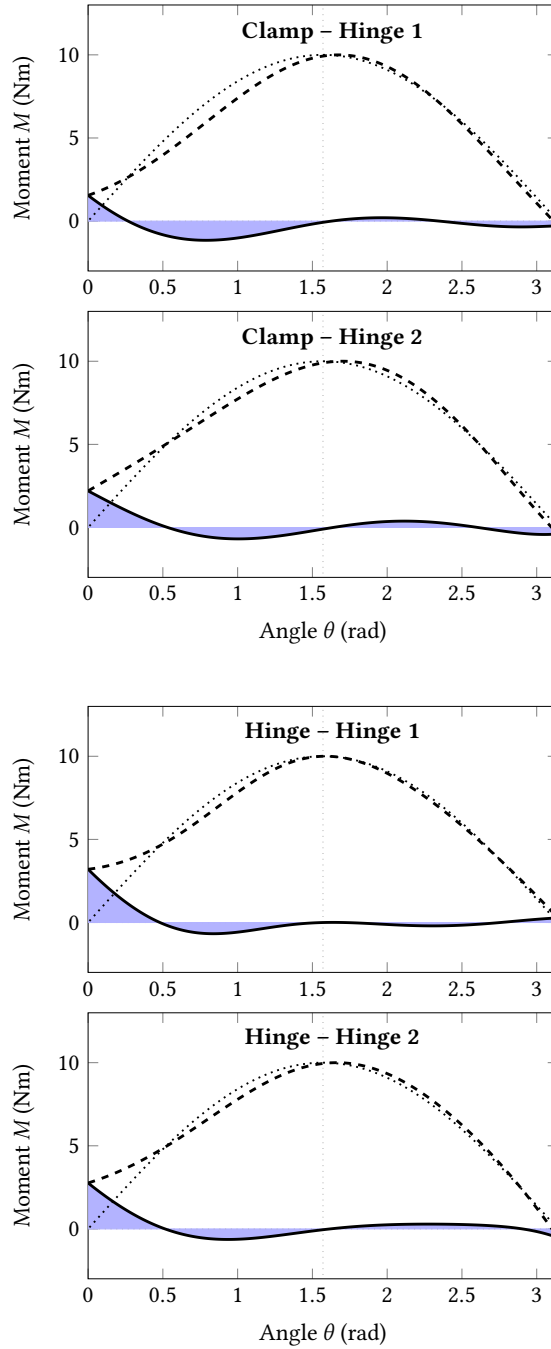
<https://techrxiv.org>

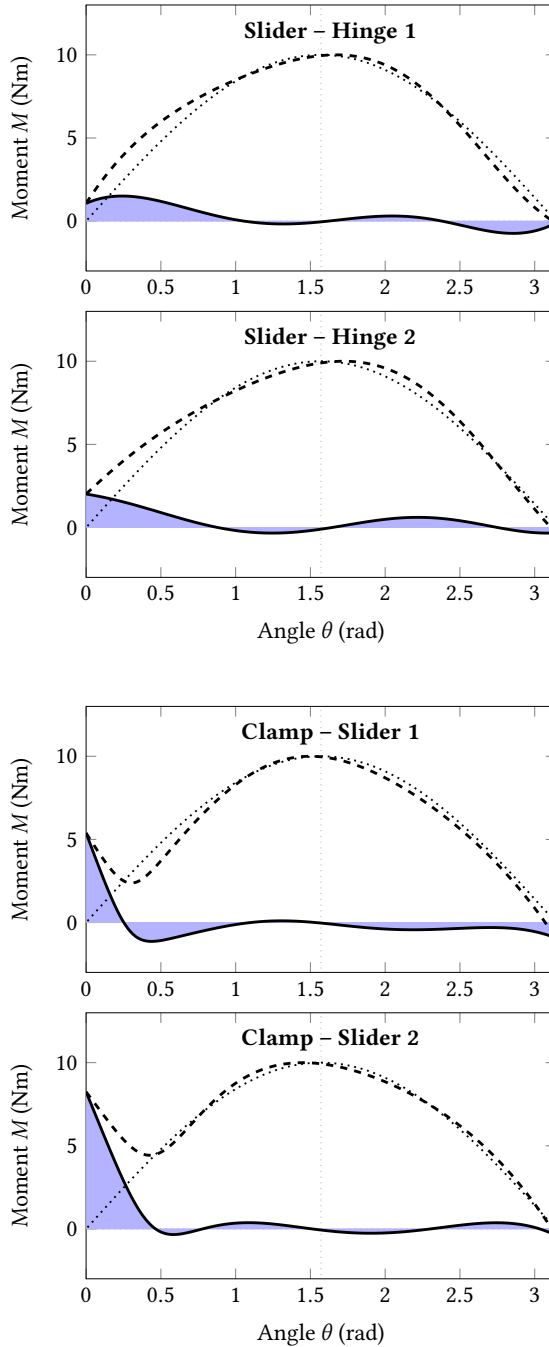
Digital Object Identifier 10.36227/techrxiv.14256044

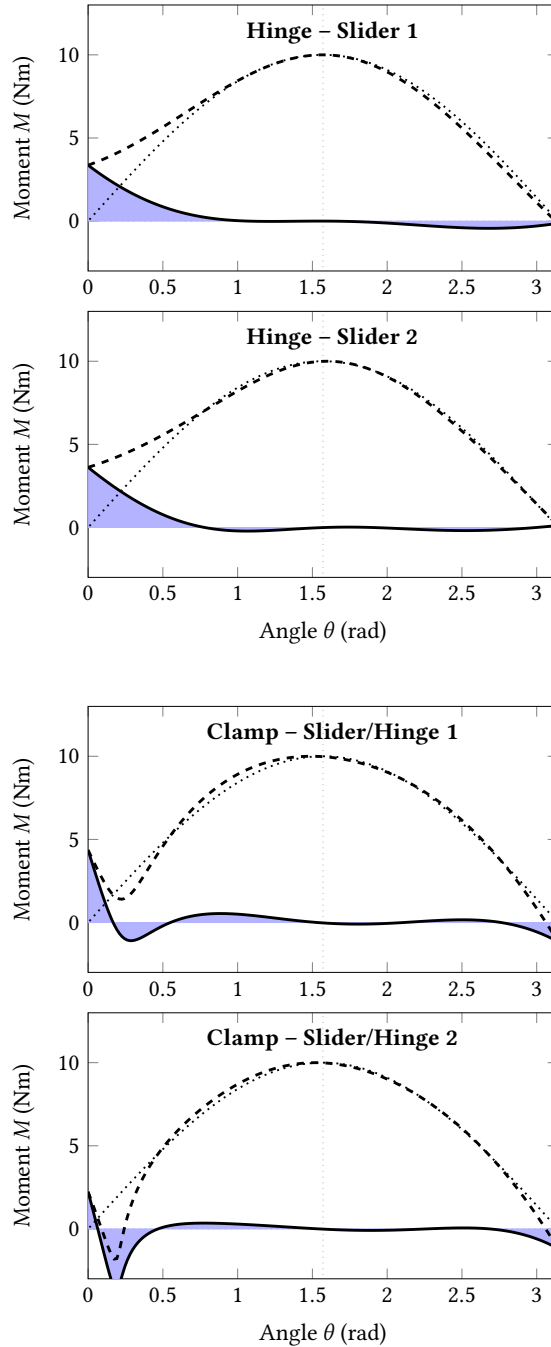
Standard image resolution movies (77 MB)

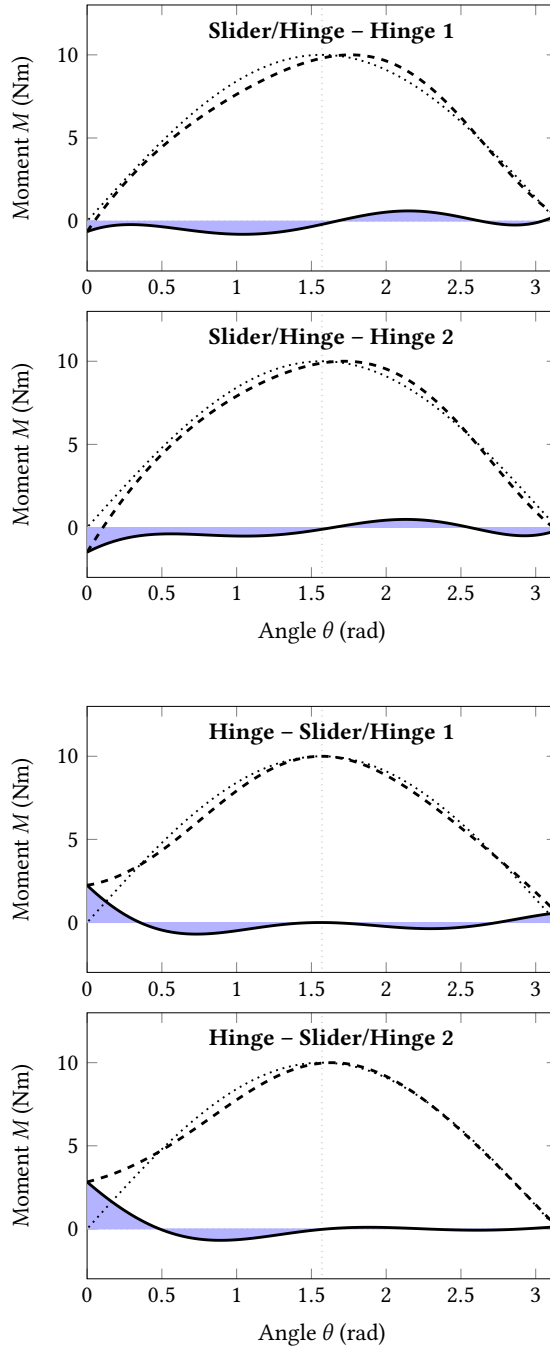
For alternative links and additional materials, visit: <https://tschiersky.org/dissertation>











Flexure parameters (1/2)

Par.	Unit	Clamp – Clamp		Hinge – Clamp	
		1	2	1	2
s_x	mm	-158.6	-101.6	-20.2	-121
s_z	mm	-35.8	-176.5	-326.8	-289.3
l_1	mm	137.9	212.4	453.1	15.8
l_2	mm	262	231	141.4	482.3
l_3	mm	429.7	371.2	152.9	225.7
φ_1	rad	-1.9271	3.1308	2.1969	2.8635
φ_2	rad	2.5273	2.0187	0.9591	1.8557
φ_3	rad	0.5637	0.3028	-0.5443	-0.438
t_1	mm	4.1	4.7	26.3	18.5
t_2	mm	4.1	4.9	18.5	19.9
t_3	mm	5.6	8.9	10.6	8.9
t_4	mm	3.7	1.4	10.8	13.8
t_5	mm	6.4	5.6	341.9	303.4
w	mm	81.1	106.8	19.6	26.6

Par.	Unit	Clamp – Hinge		Hinge – Hinge	
		1	2	1	2
s_x	mm	-162.3	-170.2	-131.9	-137.2
s_z	mm	-30.1	-92.3	36.9	27
l_1	mm	193.2	209.5	164.2	176.2
l_2	mm	427.3	58.7	196.6	335.4
l_3	mm	162.8	453.8	172.8	90.9
φ_1	rad	-3.0013	3.138	-3.1377	3.0465
φ_2	rad	0.8828	2.0036	1.3167	0.9608
φ_3	rad	-1.4753	0.7076	0.2094	-0.8429
t_1	mm	8.6	64.3	13.7	204.7
t_2	mm	8.9	9.3	99.8	9.3
t_3	mm	9.4	5	4.7	4.6
t_4	mm	16.6	6.6	2.7	319.3
t_5	mm	10.6	10.7	9.6	161.3
w	mm	29.1	50.5	23	18.2

Par.	Unit	Slider – Hinge		Clamp – Slider	
		1	2	1	2
s_x	mm	-73.3	-95	-147.7	-151.2
s_z	mm	78.6	83.1	-400	-399.1
l_1	mm	74.7	167.9	188.4	11.1
l_2	mm	272.1	199.3	377.3	303.5
l_3	mm	66.5	16.4	108.6	375.5
φ_1	rad	-3.1141	2.3775	1.4526	-0.633
φ_2	rad	1.3183	0.6052	1.5885	1.637
φ_3	rad	-1.3349	-2.0685	0.7564	1.3028
t_1	mm	1.6	20	2	2.2
t_2	mm	17.6	144.8	3.7	3.5
t_3	mm	45.2	3.2	4.7	5.3
t_4	mm	6	1.5	33.2	9.2
t_5	mm	2.4	1.5	3	11.8
w	mm	62.5	291.3	135.4	106.6

Flexure parameters (2/2)

Par.	Unit	Hinge – Slider		Clamp – Slider/Hinge	
		1	2	1	2
s_x	mm	-92.4	-188.1	-143.1	-132.8
s_z	mm	-365.5	-62.5	-395.5	-392.4
l_1	mm	498.5	371.7	451.3	487.8
l_2	mm	212.5	277.1	193.7	21.3
l_3	mm	176.7	66.6	20.1	233.1
φ_1	rad	2.0656	2.2265	1.5303	1.5931
φ_2	rad	0.8049	0.1319	1.0767	-0.5537
φ_3	rad	-0.875	-0.0084	-2.9133	1.2198
t_1	mm	31.7	5.2	3.7	4.6
t_2	mm	23.1	2	6.2	5.7
t_3	mm	9.6	1.2	9.3	24.5
t_4	mm	15.6	74	17.3	10.2
t_5	mm	20.3	13.1	147.3	16.8
w	mm	11.9	68.9	50.9	73.5

Par.	Unit	Slider/Hinge – Hinge		Hinge – Slider/Hinge	
		1	2	1	2
s_x	mm	-75	-79.8	-134.3	-136.3
s_z	mm	79.8	72.6	-89.6	-14.6
l_1	mm	29.3	86.3	140	141.5
l_2	mm	101.4	219.6	247.1	143.5
l_3	mm	133.8	22.8	136.4	223.1
φ_1	rad	-3.1134	2.8107	-3.1143	3.1218
φ_2	rad	2.0872	1.207	1.254	1.6744
φ_3	rad	1.0764	-0.465	-0.4641	0.1543
t_1	mm	43.9	60.8	30.5	40.8
t_2	mm	51.4	46.8	19.8	10.3
t_3	mm	48.6	71.4	22	15
t_4	mm	39.2	66	8.9	10.6
t_5	mm	43.6	58.8	25.5	48.7
w	mm	3.5	4	11.5	4.6

Preview: Supplementary file 2 – Additional_Tables.pdf (2/4)

Joint stiffnesses and ranges of motion (1/2)

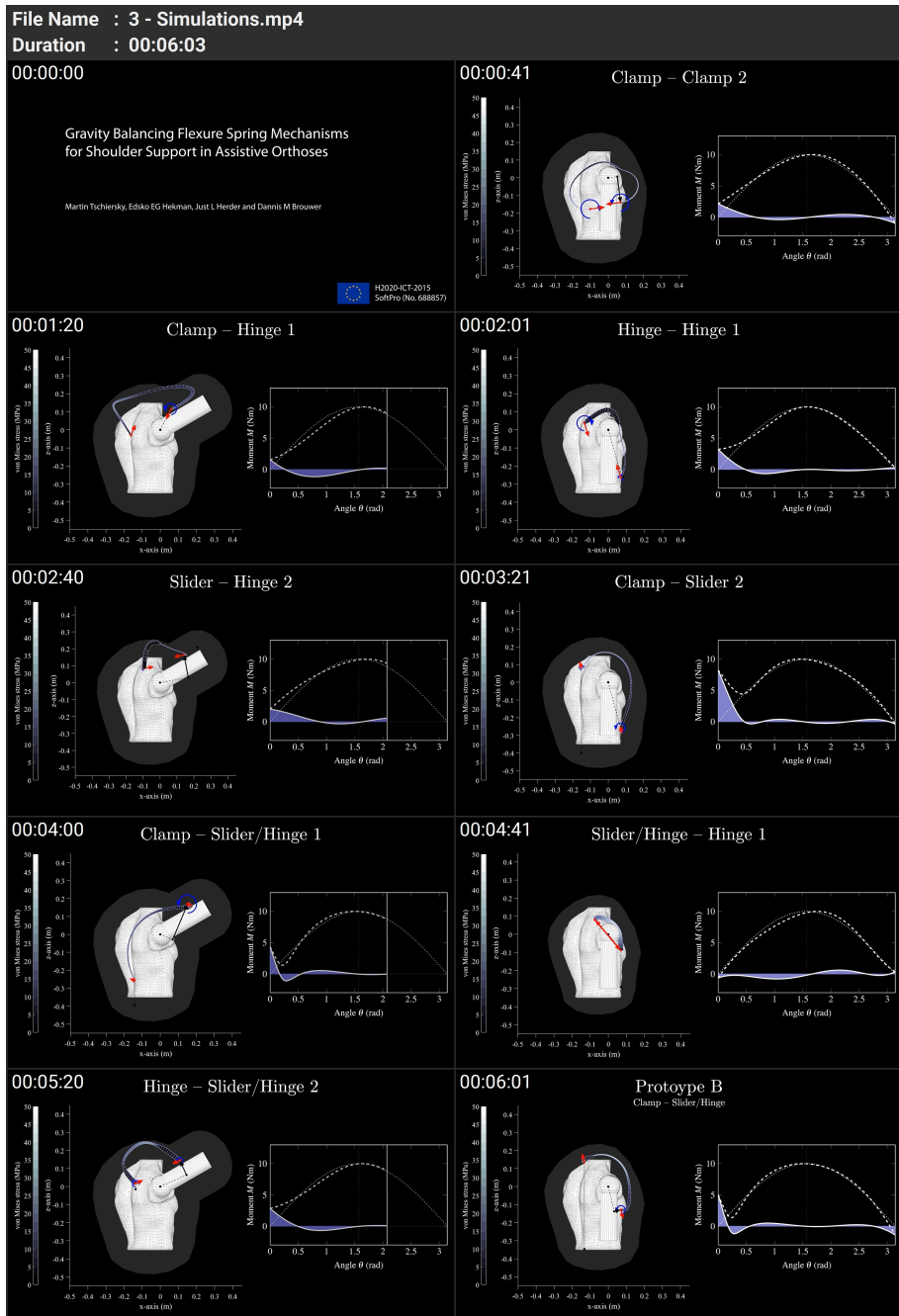
Par.	Unit	Clamp – Clamp		Hinge – Clamp	
		1	2	1	2
k_a	N/cm cm				
c_a	Nm/rad rad			0 [0.06 2.45]	0 [-0.04 2.35]
k_b	N/cm cm				
c_b	Nm/rad rad				
Par.	Unit	Clamp – Hinge		Hinge – Hinge	
		1	2	1	2
k_a	N/cm cm				
c_a	Nm/rad rad			3.3 [0.02 1.29]	8.93 [-0.01 1.07]
k_b	N/cm cm				
c_b	Nm/rad rad	0 [-2.65 0.05]	0 [-2.11 0.05]	4.57 [-2.71 -0.04]	4.11 [-2.65 0.06]
Par.	Unit	Slider – Hinge		Clamp – Slider	
		1	2	1	2
k_a	N/cm cm	8.69 [-20.4 0.1]	6.28 [-18 0.2]		
c_a	Nm/rad rad				
k_b	N/cm cm			0.7 [-0.8 49.6]	0.73 [-0.4 48.3]
c_b	Nm/rad rad	0.16 [-2.67 0.03]	2.68 [-2.49 0.05]		

The range of motion for each joint is given by the difference between the minimum and maximum displacement value, shown in the square brackets.

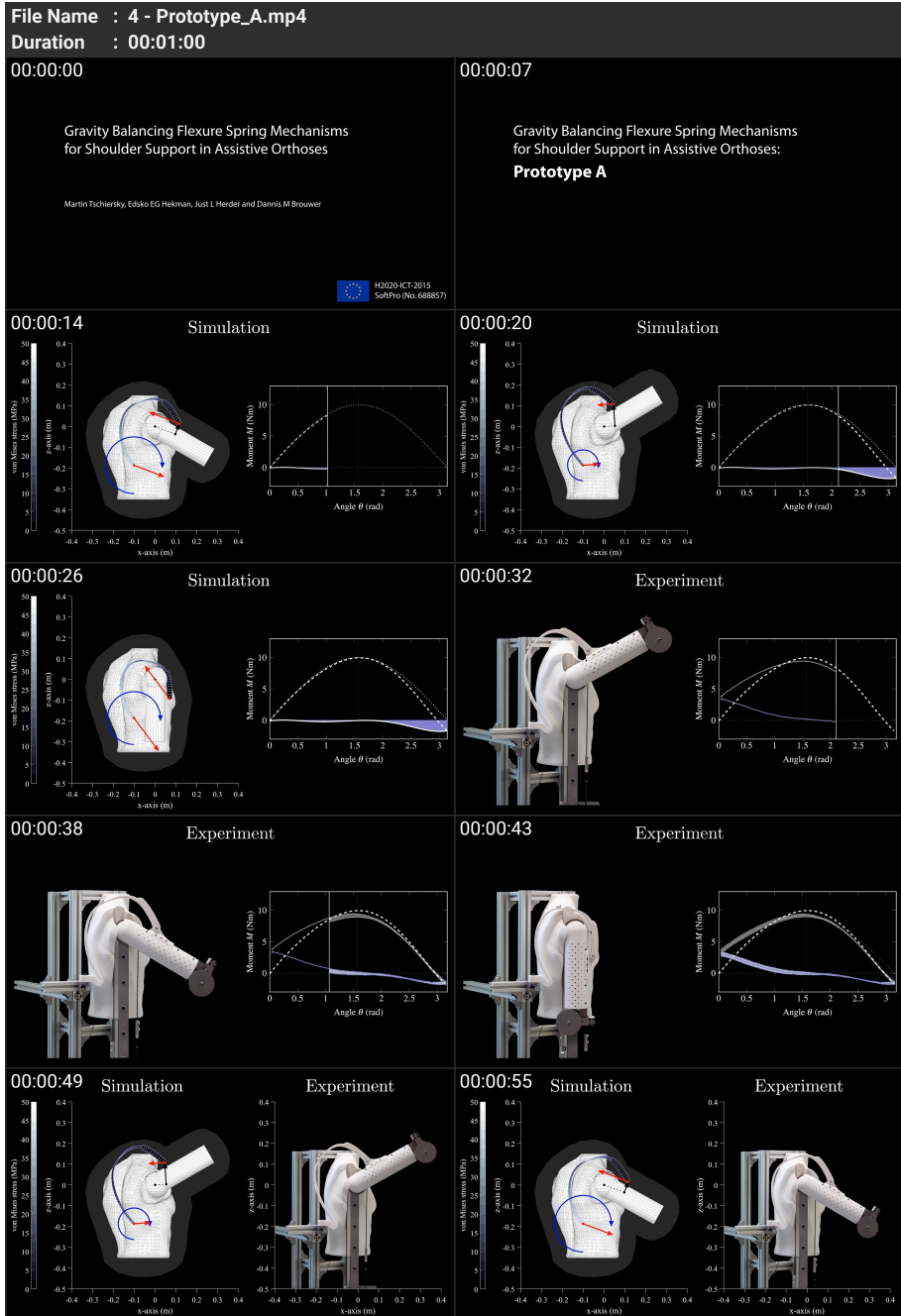
Joint stiffnesses and ranges of motion (2/2)

Par.	Unit	Hinge – Slider		Clamp – Slider/Hinge	
		1	2	1	2
k_a	N/cm cm				
c_a	Nm/rad rad	3.4 [-0.02 2.58]	10.24 [0.01 1.61]		
k_b	N/cm cm	5.93 [-5.2 1.8]	17.53 [-1.2 1]	0.84 [-1.2 54.6]	0.73 [-1.2 56.9]
c_b	Nm/rad rad			0.12 [-1.05 0.32]	0.79 [-1.3 0.24]
Par.	Unit	Slider/Hinge – Hinge		Hinge – Slider/Hinge	
		1	2	1	2
k_a	N/cm cm	8.3 [-20.3 -0.5]	9.56 [-17.5 0.2]		
c_a	Nm/rad rad	0.2 [-0.15 0.84]	6.09 [-0.06 0.81]	7.37 [0.04 1.86]	9.89 [0 1.37]
k_b	N/cm cm			6.83 [0.5 7]	6.19 [-3.7 3.1]
c_b	Nm/rad rad	0.24 [-2.68 -0.1]	0.39 [-2.63 0.03]	5.45 [-1.46 -0.03]	5.17 [-1.89 -0.01]
The range of motion for each joint is given by the difference between the minimum and maximum displacement value, shown in the square brackets.					

Preview: Supplementary file 2 – Additional_Tables.pdf (4/4)



3
A



Preview: Supplementary file 4 – Prototype_A.mp4

File Name : 5 - Prototype_B.mp4
Duration : 00:01:00

00:00:00

Gravity Balancing Flexure Spring Mechanisms for Shoulder Support in Assistive Orthoses

Martin Tschiersky, Edsko EG Hekman, Just L Herder and Dennis M Brouwer

10209-1CF-2019 SciPro (No. 688857)

00:00:07

Gravity Balancing Flexure Spring Mechanisms for Shoulder Support in Assistive Orthoses: **Prototype B**

00:00:14 **Simulation**

00:00:20 **Simulation**

00:00:26 **Simulation**

00:00:32 **Experiment**

00:00:38 **Experiment**

00:00:43 **Experiment**

00:00:49 **Simulation** **Experiment**

00:00:55 **Simulation** **Experiment**

3
A

File Name : 6 - Prototype_A_Experiment.mp4	
Duration : 00:02:39	
00:00:00	00:00:07
<p>Gravity Balancing Flexure Spring Mechanisms for Shoulder Support in Assistive Orthoses</p> <p>Martin Tschiersky, Edsko EG Hekman, Just L. Herder and Dennis M Brouwer</p> 	<p>Gravity Balancing Flexure Spring Mechanisms for Shoulder Support in Assistive Orthoses:</p> <p>Prototype A Experiment</p>
00:00:15	00:00:21
<p>Footage shows a sinusoidal velocity profile Actual experiments were conducted at a near constant velocity</p>	<p>Back view: -60°</p> 
00:00:43	00:01:05
<p>Side view: -30°</p> 	<p>Side view: 0° (perpendicular to flexure)</p> 
00:01:27	00:01:49
<p>Side view: +30°</p> 	<p>Front view: +60°</p> 
00:02:11	00:02:33
<p>Front view: +90°</p> 	<p>Front view: +120°</p> 

Preview: Supplementary file 6 – Prototype_A_Experiment.mp4

File Name : 7 - Prototype_B_Experiment.mp4	
Duration : 00:02:39	
00:00:00	00:00:07
<p>Gravity Balancing Flexure Spring Mechanisms for Shoulder Support in Assistive Orthoses</p> <p>Martin Tschiersky, Edsko EG Hekman, Just L. Herder and Dennis M Brouwer</p> 	<p>Gravity Balancing Flexure Spring Mechanisms for Shoulder Support in Assistive Orthoses:</p> <p>Prototype B Experiment</p>
00:00:15	00:00:21
<p>Footage shows a sinusoidal velocity profile Actual experiments were conducted at a near constant velocity</p>	<p>Back view: -60°</p> 
00:00:43	00:01:05
<p>Side view: -30°</p> 	<p>Side view: 0° (perpendicular to flexure)</p> 
00:01:27	00:01:49
<p>Side view: +30°</p> 	<p>Front view: +60°</p> 
00:02:11	00:02:33
<p>Front view: +90°</p> 	<p>Front view: +120°</p> 

3
A

Preview: Supplementary file 7 – Prototype_B_Experiment.mp4

CHAPTER 4

Wearable Implementations of Flexure Spring Mechanisms

Thesis note This chapter presents three wearable prototypes that make use of the technologies described in Chapter 2 and Chapter 3. These prototypes were made in the context of the SoftPro project¹ which was the main source of funding for this research. The purpose of this chapter is to briefly introduce these devices in order to show the reader wearable applications involving human subjects and thus, in addition to the rather abstract technical evaluations of the previous chapters, help assess the practical value of these technologies.

4.1 SOFTPRO WEARABLE SYSTEM

The SoftPro Wearable System [19] is a wearable technology demonstrator assembled and tested by the University of Siena. It integrates the Assistive Elbow Orthosis (ÆOs) from Chapter 2 with a supernumerary robotic finger called the Robotic Sixth Finger [59], a flexible surface electromyography (sEMG) interface [74] embedded in a cap called e-Cap [18, 26], and a haptic interface called CUFF [6]. The integrated device worn by a healthy subject is shown in Figure 4.1.

¹European Union's Horizon 2020 research and innovation programme, grant agreement No. 688857



Figure 4.1: The SoftPro Wearable System, worn by a healthy subject. a) e-Cap, b) Assistive Elbow Orthosis, c) CUFF, d) common power supply and control unit, e) Robotic Sixth Finger

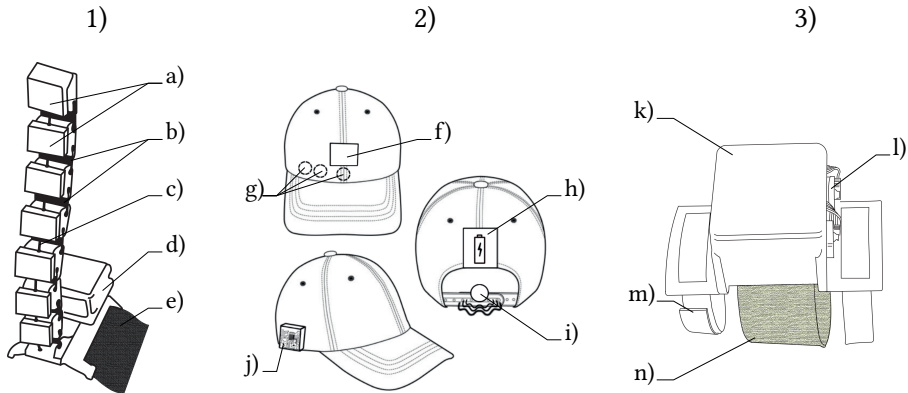


Figure 4.2: Schematic figures. 1) Robotic Sixth Finger: a) rigid links, b) flexible members, c) tendon, d) motor housing, e) Velcro strap; 2) e-Cap: f) capacitive touch sensor, g) sEMG electrodes (inside), h) power supply, i) vibrotactile motor, j) signal processing unit; 3) CUFF: k) motor housing, l) encoders and connectors, m) Velcro strap, n) fabric belt

The device is intended to assist people with impaired hand function, e.g., due to stroke, by restoring basic grasping capabilities. Since these subjects often also have impaired arm strength and coordination, providing them with elbow flexion support will indirectly support grasping by making it easier to reach the object to be grasped.

The Robotic Sixth Finger is the main component of the device. It acts like an opposable thumb that can be used to grasp an object by wrapping around it and pressing it against the adjacent limb, e.g., the forearm or hand. Its finger-like structure consists of a modular chain of rigid links connected by flexible members. It is driven by a geared electric motor via a tendon which is routed through the rigid links and fixed to the most distal link.

The opening and closing of the Robotic Sixth Finger finger is controlled via the e-Cap. The e-Cap features 3D-printed flexible sEMG electrodes [74], a signal processing unit, an autonomous power supply, a vibrotactile motor and a capacitive touch sensor, which are all integrated into a baseball cap. The sEMG electrodes are fixed to the forehead, and by activating the frontalis muscle the user can send trigger signals wirelessly to the Robotic Sixth Finger in order to control its operation. When a trigger signal is detected physical feedback is given to the user via the vibrotactile motor. The capacitive touch sensor is exclusively used to initiate the EMG calibration procedure, which is required before use.

To help the user control the operation of the supernumerary finger, the CUFF provides a haptic feedback to the user which is proportional to the force exerted by the Robotic Sixth Finger. The CUFF features a fabric belt that is attached to a geared electric motor at each end. The motors are located in a single housing. The housing and the belt form a loop which is worn around the arm. Force feedback is rendered by shortening the belt via the motors, and thus applying pressure to the arm.

A modified version of the Assistive Elbow Orthosis acts as the structural frame of the SoftPro Wearable System to which the Robotic Sixth Finger and CUFF are fixed. It is used to compensate for the weight of the wearer's forearm as well as for the weight of the additional components. Schematic figures of the Robotic Sixth Finger, the e-Cap and the CUFF are shown in Figure 4.2. For more information regarding the Assistive Elbow Orthosis, please refer to Chapter 2.

The integrated device has been used in a pilot study involving three people affected by stroke. The participants received the system at their paretic hand and were asked to perform common activities of daily living. Though the participants voiced several concerns, also with respect to the size of the spring, the study found that all participants perceived the device as both useful and easy to use [19].

4.2 WEARABLE SHOULDER SUPPORTS

Two wearable shoulder support prototypes are presented in this section. They are based on preliminary versions of the synthesis method which is described in Chapter 3, and reflect different stages of development.

Due to initial problems finding feasible mechanism designs, all objectives and constraints were only evaluated for elevation angles between 0 and 90 deg during the optimizations of both prototypes. A maximum moment amplitude of 9.16 Nm was used as reference and target value, based on the same assumptions as specified in subsection 5.2.1 of Chapter 5. Since the devices were not evaluated following scientific protocols, no performance claims with respect to the physical prototypes are made.

4.2.1 Prototype 1

The first prototype stems from the exploratory stage of development. It was optimized using a spatially curved flexure which is clamped at both interfaces. As bending in a second direction, torsion along the flexure and more thickness intervals were considered, the total number of optimization parameters was 32, which is significantly larger than the 13 to 17 parameters considered in Chapter 3. In comparison to later optimizations also stricter spatial constraints were applied, limiting the maximum protrusion in the range from $0 \leq \theta \leq 90$ deg to below 5 cm. The resulting optimized prototype – in its physical implementation as well as in simulation – can be seen in Figure 4.3, and its computed balancing behavior is shown in Figure 4.4.

The prototype exceeds the maximum stress of 41.67 MPa in simulation at elevation angles of $\theta \geq 161.5$ deg, as indicated by the red regions in Figure 4.4. Consequently, higher angles were not examined with the physical prototype. Also, mild collision between the flexure and the anterior side of the shoulder is encountered both in simulation and during tests with the physical prototype. The estimated assistive effect of the device, which has a maximum moment amplitude of 4 Nm, amounts to roughly 33 % gravity compensation in the range between 9 and 104 deg arm elevation. For angles above 104.5 deg the spring mechanism shows an adverse effect in simulation. However, the potentially beneficial effect of collision towards lower elevation angles is not captured by the simulation.

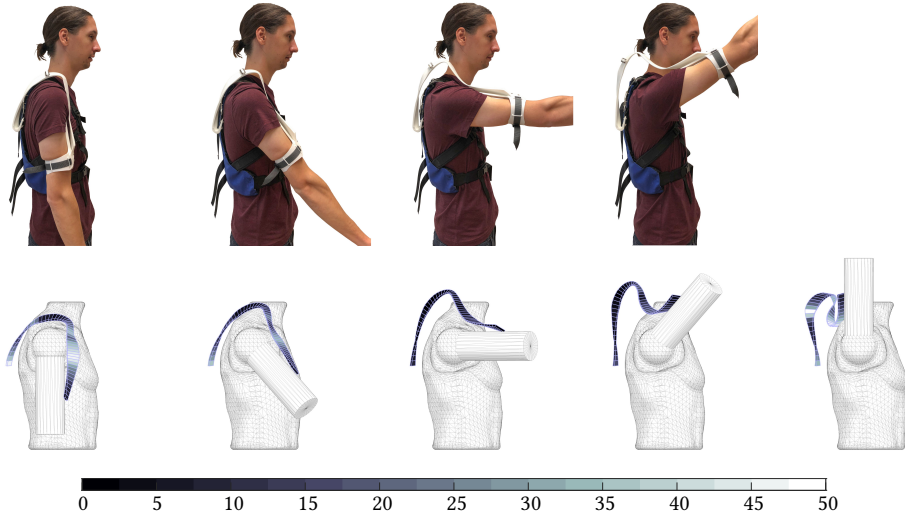


Figure 4.3: Photos of Prototype 1 worn by a healthy subject in juxtaposition to a simulated animation, shown in increments of $\pi/4$ from $\theta = 0$ (left) to $\theta = \pi$ (right). Color scale in MPa.

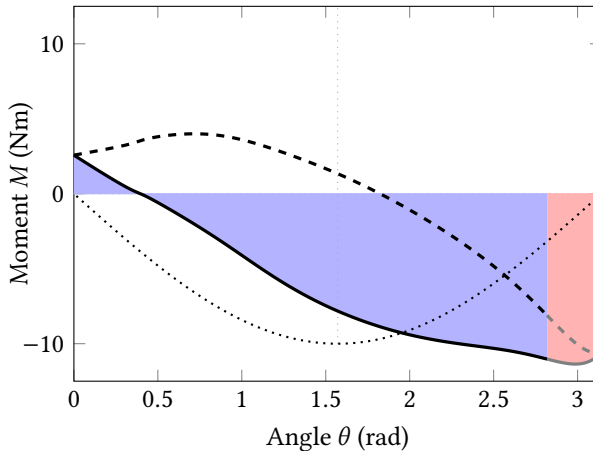


Figure 4.4: Optimized balancing behavior of Prototype 1. The dashed line depicts the computed moment generated by the flexure. The dotted line shows the unbalanced load moment. The solid line shows the balanced behavior of the mechanism, when adding the load moment to the flexure moment. The shaded areas indicate the balancing error. The lines are depicted in gray and the shaded areas in red for regions where the maximum stress is exceeded. This diagram shows that the necessary moment to lift the arm is reduced for elevation angles between 0.16 and 1.82 rad (9 and 104 deg), but increased outside of this range.



Figure 4.5: Front and back of Prototype 1 worn by a healthy subject.

In comparison to the results from Chapter 3 and using the same metrics as defined in subsection 3.2.2, this design has a significantly worse balancing error of $\delta = 0.3842$ and $\delta = 0.7058$ for the ranges from 0 to 90 deg and 0 to 180 deg, respectively. Also the relative strength of $\epsilon = 0.8$ N/cm in the assistive range from 9 to 104 deg is comparatively low, and somewhat atypical for the *Clamp-Clamp* category it also has a comparatively high relative shear force of 9.71 N/Nm. However, the design features a relatively close alignment with the body, having a maximum protrusion of 13.75 cm, going down to 4.17 cm when the arm is lowered, and averaging at 8.67 cm.

The physical prototype shown in Figure 4.3 consist of three components, which can be more closely examined in Figure 4.5. The first is a simple vest-like interface consisting of a reinforced backplate and a harness similar to a backpack. The second is the optimized flexure, made from laser-sintered PA2200, which is fixed to the vest via a sheet-metal extension. Due to the same size restrictions as discussed in Chapter 3, the flexure is split into two parts and joined with a bolted flange connection. For this a region of relatively low stress was chosen, as can be verified in Figure 4.3. The third and last part is the laser-sintered arm interface which is bolted to the end of the flexure, connecting it to the upper arm. The entire device has a weight of 1020 g.

4.2.2 Prototype 2

The second prototype stems from the later stages of development and is already very reminiscent of the results presented in Chapter 3. The synthesis method that was applied is largely identical to the one described in Chapter 3 and the used configuration is the same as for the *Hinge-Clamp* category. Thus, the device closely resembles the design of prototype A from Chapter 3. The largest difference with respect to these later studies is that this design was optimized using a torso mesh for collision detection which features additional cylindrical volumes at the shoulder regions. This was done as in the course of the research project this prototype was to be integrated with another device, which is not disclosed in this thesis. The physical prototype and respective animations from the simulation are shown in Figure 4.6, while Figure 4.7 shows the computed balancing behavior.

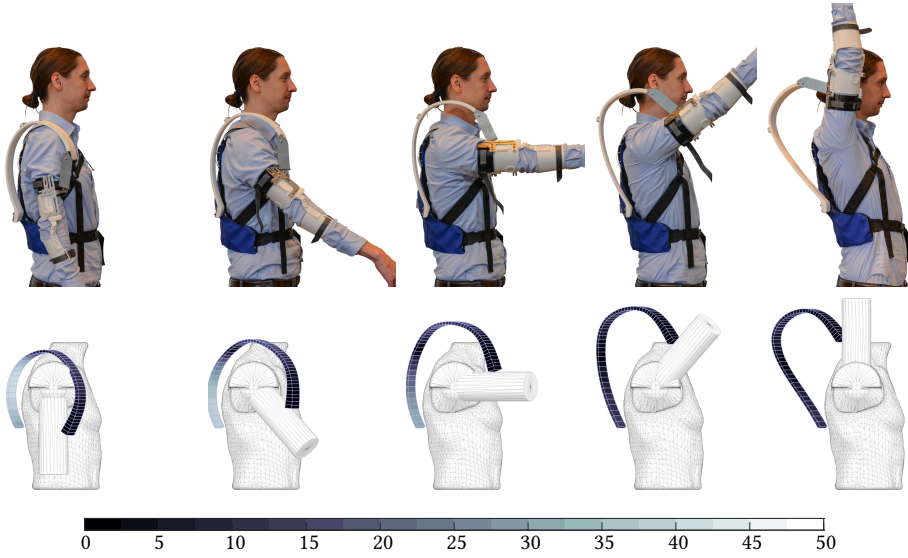


Figure 4.6: Photos of Prototype 2 worn by a healthy subject in juxtaposition to a simulated animation, shown in increments of $\pi/4$ from $\theta = 0$ (left) to $\theta = \pi$ (right). Color scale in MPa.

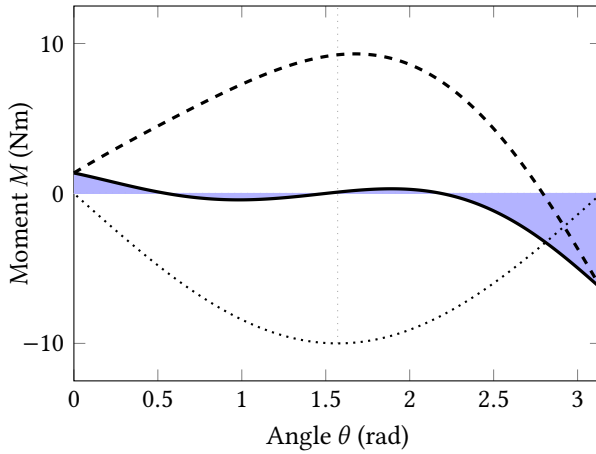


Figure 4.7: Optimized balancing behavior of Prototype 2. The dashed line depicts the computed moment generated by the flexure. The dotted line shows the unbalanced load moment. The solid line shows the balanced behavior of the mechanism, when adding the load moment to the flexure moment. The shaded areas indicate the balancing error. This diagram shows a good balancing behavior from 0 to 2.53 rad (0 to 145 deg), and a reduction of the required moment for elevation angles up to 2.79 rad (160 deg).

According to the simulations the device provides almost full gravity compensation for elevation angles up to 145 deg and continues to have an assistive effect up to 160 deg. Its maximum moment amplitude of 9.31 Nm meets the requirements and the balancing error is $\delta = 0.0475$ and $\delta = 0.1129$ for elevation angles from 0 to 90 deg and 0 to 180 deg, respectively. Considering the other performance metrics, it is a rather typical example for the *Hinge-Clamp* category, though performing slightly worse compared to later results shown in Chapter 3. It exhibits a relative strength of $\epsilon = 9.25$ N/cm and a relative shear force of 15.33 N/Nm. The protrusion has a maximum value of 24.68 cm, which reduces with decreasing arm elevation down to 5.82 cm, and has an average value of 13.64 cm. In comparison to the first prototype this device offers adequate gravity support, both qualitatively and quantitatively. However, it is at a disadvantage with regards to protrusion and relative shear force. To this end, the same analysis and criticism applies as pertains to the other designs of the *Hinge-Clamp* category and prototype A, presented in Chapter 3. Especially, the high shear force at the arm attachment which is computed to be up to 150 N for this device is a major drawback that likely negatively affects wearing comfort.

The physical prototype for this design also consists of three components. The vest is the same as the one used in the first prototype and the flexure was made in the same way, again consisting of two joined parts. The arm interface now extends over the elbow joint via a hinged connection, attaching and distributing the load to both the upper arm and forearm. A simple hinged connection between the flexure and the arm interface is realized with a cable tie. It connects a C-shaped metal extension bracket, which is fixed to the flexure and replaces part of its rigidly behaving section, with a metal arc above the upper arm which fixed to the arm attachment. The total weight of this prototype is 2011 g.

4.3 DISCUSSION

All gravity-balancing wearable assistive devices discussed in this chapter exhibit relatively low technology readiness levels. The only device that has been clinically evaluated is the Assistive Elbow Orthosis from Chapter 2. However, the respective pilot study only involved three participants and tested the orthosis as part of an integrated device, involving several other components. This makes it hard to determine the isolated benefit of the Assistive Elbow Orthosis. Specific feedback with regards to the orthosis, mainly criticizing the size of the spring, may be easily addressed in future prototypes, and is therefore not a valid measure for the underlying technology. With respect to the methodology, it should also be critically noted that due to creep and stress relaxation the mechanical behavior of the Assistive Elbow Orthosis used in the study is likely to differ from the simulated and measured behavior in Chapter 2.

The two wearable shoulder support prototypes can – for the most part – only be assessed based on computed performance measures. Concerning the first prototype, the poor balancing quality and low relative strength are likely in great part due to the tighter spatial constraints which have been applied and due to the larger number of design parameters, creating a vastly increased solution space for the optimization.

However, for this early stage of development the comparatively low protrusion of this device appeared very promising and its appearance was close to envisioned concept. Still, later research showed that the performance bottleneck induced by the constraints and number of parameters could not be overcome, leading to the planar designs presented in Chapter 3. The second prototype can already be seen as a representative of that latest design generation, being technically equivalent to prototype A from Chapter 3. Hence, its performance is also similar, though – for the reasons given in the previous section – having a larger maximum protrusion.

The only physical measures that were reliably obtained are the weights of the devices. These are promising, as they can compete with current commercial devices. However, it should be noted that both prototypes are unilateral designs, and that a bilateral design would be heavier. The juxtapositions of the physical devices worn by a healthy subject and the respective simulations generally show good agreement. Furthermore, by showing the device in proper context, the pictures provide a better sense of scale than the photos of the experiment presented in Chapter 3. Thus they are particularly useful for comparison with other wearable assistive devices.

Part II

Active Mechanisms

A Compact McKibben Muscle Based Bending Actuator for Close-to-Body Application in Assistive Wearable Robots

Abstract In this chapter a pneumatic bending actuator for upper-limb assistive wearable robots is demonstrated, which uses thin McKibben muscles in combination with a flexure strip. The actuator features both active soft actuation and passive gravity support, and in terms of force transmission bridges the gap between the classic rigid-type actuators and the emerging soft actuator technologies. Its flexure strip leverages the high-force low-displacement properties of McKibben muscles towards a large rotational range of motion and reduces localized forces at the attachments. The synthesis method by which these actuators can be obtained and optimized for high specific moment output is explained. Physical specimens of three optimized actuator designs are built and tested on a dedicated experimental setup, verifying the computational models. Furthermore, a proof-of-concept upper-limb assistive wearable robot is presented to illustrate a practical application of this actuator and its potential for close-to-body alignment. It is found that based on the currently available components actuators can be built which, given a width of 80 mm, are able to produce a moment exceeding 4 Nm at an arm elevation of 90 deg.

5.1 INTRODUCTION

Assistive wearable robots are devices that are designed to facilitate functional movements of their wearer. These devices target people suffering from deficient motor function [68]. By providing supporting forces and moments they mitigate the effects of muscular weakness, and thereby restore the ability to perform activities of daily living (ADLs). Thus, they can reduce the need for external help and may enhance social participation [40, 69]. Yet, to this day, active assistive wearable devices exhibit significant shortcomings which prevent their widespread adoption [21, 39, 40, 53, 66]. Many of these can be traced back to the method of actuation [40] which often determines the overall mechanical structure of the device.

Traditionally, industrial grade actuation components in combination with rigid-link braces or exoskeletons are used [69]. However, promising new technologies emerge from the field of soft robotics, which increasingly permeate into the field of assistive wearable devices. In comparison to their rigid-link counterparts soft orthotic systems are generally cheaper, lighter and have lower inertia. Furthermore, due to the absence of an external rigid-link structure they can feature a lower profile which makes them smaller, and therefore, more portable, easier to conceal and potentially even wearable underneath clothing [68].

These benefits of soft robotic architectures are key advantages to raise the functional and social acceptability [53] of assistive wearable robots in order to promote their widespread adoption for everyday use [68, 69].

The two predominant actuation methods currently used in wearable soft robotic devices are electric and pneumatic actuation [12, 68]. Electric actuation is almost exclusively implemented using cable-based transmission systems, which have the ability to provide high forces and large displacements [40, 68]. Pneumatic actuation, on the other hand, boasts a wide range of diverse implementations and embodiments. The advantages of pneumatic actuators are their low impedance, low weight and high power-to-weight ratio, when the pneumatic source is neglected. However, their main disadvantages are, generally, a low force and/or displacement capability [68].

The exception to this rule are the class of pneumatic artificial muscles (PAMs) which, although limited in stroke, possess high force capabilities. Several different embodiments of PAMs exist, but the most established and most commonly used in wearable robotic devices is the McKibben muscle type actuator [13, 68]. The basic structure of a McKibben muscle comprises a gas-tight elastic inflatable tube or bladder surrounded by a helical braided sleeve composed of flexible, inextensible threads. When pressure is applied, the inner tube expands radially against the braid. Due to the high longitudinal stiffness of the threads the actuator has to shorten for its volume to increase. This causes the actuator to contract and produce tension [11, 13].

Increasing efforts have been made to miniaturize McKibben muscles [5, 62, 70]. These miniaturized versions feature a reduced size and weight, while maintaining the high specific force and power characteristics. In addition, they stay flexible when pressurized, allowing them to bend while contracting [37]. These features make them exceptionally suitable for use in wearable soft robotic devices, as they enable alignment very close to the body, distribution of actuation across the body surface and organization into larger structures, such as bundles [37], braids [33], weaves [2] and active textiles [20, 24]. Their application to upper-limb soft exosuits was previously shown by Abe et. al [1, 2].

However, McKibben muscles – similar to cable-based systems – apply tension forces very localized at their attachment points. This can be a major design challenge for powerful wearable soft robots due to the lack of a rigid frame to bear, redirect and distribute these forces to the wearer's body [32, 68]. Furthermore, to produce functional strokes McKibben muscles require large lengths, resulting in extensive routing across the body which can lead them to slide, apply uncomfortable forces and restrict motion [47].

Therefore, this study proposes a pneumatic bending actuator (PBA) which uses miniaturized McKibben muscles in combination with a flexure strip to transform the linear displacements and forces into rotational displacements and moments, respectively. Many PBAs dedicated for use in wearable soft robotic devices were shown in previous works, some of them based on McKibben muscles [46]. However, dedicated research towards PBAs with maximized force or moment output, bending displacement and power density is scarce [72].

The goal of this study is to leverage the high-force low-displacement properties of McKibben muscles through a flexure mechanism which is optimized to maximize the moment for lifting the upper arm while enabling a natural range of motion (ROM) and close-to-body alignment. Thereby, an actuator is created which incorporates both active soft actuation and passive gravity assistance, within a structure which exhibits the compliant characteristics of soft robotic devices while featuring an external force transmission behavior comparable to rigid-link exoskeletons.

Following this introduction the actuator design, the computational models, the applied optimization as well as the experiment are presented in the *Methods* section. In the *Results* section the outcomes of both the simulation-based optimization and the physical experiment are shown. Furthermore, the application of the actuator to an upper-limb assistive wearable robot is illustrated. The results are further elaborated upon within the *Discussion* section. Lastly, in the *Conclusion* section, all key findings are concisely summarized.

5.2 METHODS

5.2.1 Application Requirements

The actuator presented in this study is designated for use in an upper-limb assistive wearable robot to provide active assistance for lifting the arms from a relaxed position at 0 deg elevation to ≥ 90 deg elevation, while passively allowing for a full natural ROM of up to 180 deg elevation.

Its primary purpose is to compensate for the weight of the arms. By augmenting the wearers residual force to an elevation, i.e., flexion or abduction, of at least 90 deg it could potentially assist in the execution of the majority of ADLs found in literature [48]. Using the mean body segment data of female and male subjects as provided by de Leva [38] an external gravity moment acting on the shoulder joint of 9.16 Nm is calculated, when lifting a fully extended arm to 90 deg elevation. During common ADLs maximum shoulder joint moments of up to 14.3 ± 1.4 Nm are encountered [45].

In addition, the actuator is supposed to stay very close to the body and have a low profile. Studies on passive assistive orthoses have shown that devices should generally stay within 30 mm from the body [69], and below 20 mm to be wearable underneath clothing [14].

The actuator is to be fixed to the top of the shoulder and to the upper arm at each end, respectively. These regions are favorable regarding natural self-perception and low obstructiveness [76]. As the actuator should wrap around the shoulder it is determined, based on anthropometric data [63] and own estimates, that the minimum bending radius of the actuator should reach 80 mm or less in order to achieve a close fit.

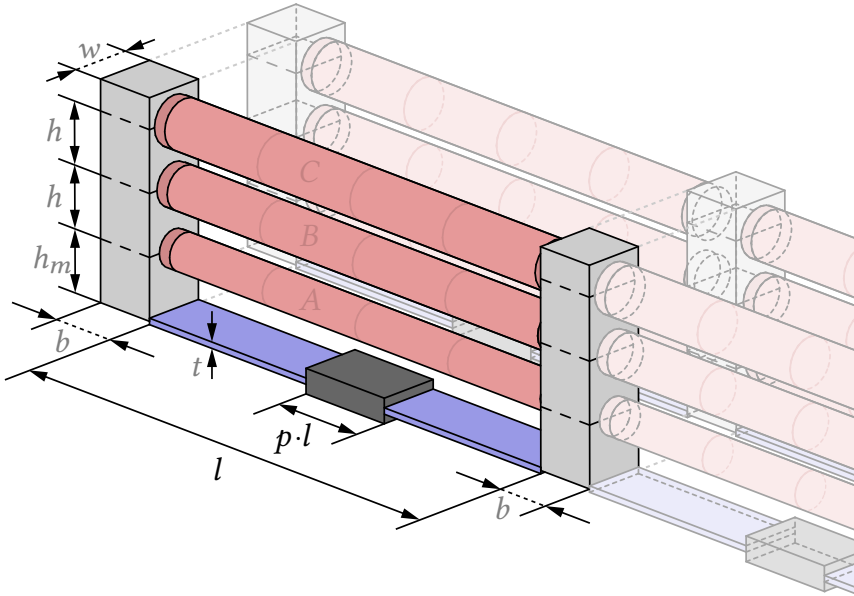


Figure 5.1: Parametrized actuator unit geometry. McKibben muscles are shown in red, their tip portions in dark red, the flexure strip in blue, the rigid brackets in light gray and the reinforced section in dark gray. Characters in black depict optimization parameters, in gray manually set parameters and in red the McKibben muscle indices. Serial and parallel units are indicated as half-transparent geometries.

5

5.2.2 Actuator Design

The proposed actuator consists of a straight flexure strip, which is subdivided into serial segments by means of equally spaced brackets that extend unilaterally from the strip. One or multiple miniaturized McKibben muscles run in parallel to the flexure, and are routed through and fixed to the brackets along their height. To avoid buckling, a central portion of the flexure strip can be reinforced by locally increasing the thickness. Multiple actuator strips can be arranged in parallel, either loosely or by physically merging them into one strip.

To enable bi-directional bending, and thus a natural ROM, the fully extended, i.e., the uninflated and unstressed length of the McKibben muscles has to be longer than the flexure length. Therefore, the McKibben muscles are compressed between each pair of brackets, externally applying an initial contraction to the braided sleeve, before they are fixed.

When the McKibben muscles are inflated their internal bladder causes them to contract further, and depending on the applied pneumatic pressure and the deflection state of the actuator, exert tension forces onto the brackets. The brackets, effectively acting as levers, transfer these forces to the flexure and induce moments. The actuator reaches an equilibrium state when the moments created by the McKibben muscles, the bending moments of the flexure strip, and the external moment loads are in balance.

5.2.3 Materials

For the flexure strip SK85 hardened steel sheets are used. Based on their specified hardness (HRC 42~46) a tensile strength of $\sigma_t = 1435$ MPa is determined [28]. The brackets and flexure reinforcement are made from an acrylonitrile-butadiene-styrene (ABS) copolymer [75]. The miniaturized McKibben muscles used in this study are production prototypes provided by s-muscle Co. Ltd. which have an uninflated and inflated diameter of 3 and 5 mm, respectively. Their pressure dependent stiffness properties are determined in isobaric quasistatic experiments on a tensile test setup consisting of a COMS PM80B-50X linear precision stage, Nidec-Shimpo FGP-50 digital force gauge, ANEST IWATA SLP-07EED air compressor and a CKD RP1000-8-07 precision regulator. This setup is identical to the one used in [33], [2] and [24]. Aside from measurements within the normal operating range, additional measurements for 0 and 0.5 MPa are conducted to determine the stiffness beyond the fully extended state.

5.2.4 Parametrization

The actuator geometry is described using the design parameters shown in Figure 5.1. To achieve a maximum power density the unit's width w and the vertical distances between the McKibben muscles h are set equal to the inflated diameter of the McKibben muscles of 5 mm. To maintain a total height below 20 mm the number of McKibben muscles is limited to three and the height of the first McKibben muscle above the flexure h_m is set to 5 mm. With regards to manufacturing, the bracket length b is also chosen to be 5 mm. The flexure thickness t is varied between 0.1 and 0.9 mm. The flexure length l , its reinforced portion p and the initial contraction ratios ε_{init} for each McKibben muscle are the optimization variables constituting the parameter vector.

$$\mathbf{x} = [l, p, \varepsilon_{init_A}, \varepsilon_{init_B}, \varepsilon_{init_C}] \quad (5.1)$$

The contraction ratio ε is defined as the relative shortening in respect to the uninflated and unstressed state.

$$\varepsilon = 1 - \frac{l}{l_0} \quad (5.2)$$

where l is the current length of the McKibben muscle and l_0 its length at rest.

In case of ε_{init} the length l equals the flexure length ($l_{init} = l$) and l_0 is the uninflated length at rest, before assembly. ε_{init} is limited to 0.1806, the maximum contraction ratio ε_{max} at 0.5 MPa, to avoid that the fully contracted length at 0.5 MPa exceeds the flexure length.

5.2.5 McKibben Muscle Model

McKibben muscles can be regarded as active nonlinear springs, where the stiffness can be controlled by the applied pressure P [64]. However, since this study is only concerned with the isobaric behavior at two distinct pressure states, the minimum and maximum operating pressures 0 and 0.5 MPa, respectively, the McKibben muscles are modeled as passive elements.

Their stiffness behavior is separated into three regions: a region of approximately linear stiffness in the operating range $0 \leq \varepsilon \leq \varepsilon_{max}$, a region of rapid nonlinear stiffness increase for $\varepsilon < 0$, and a region of rapid nonlinear stiffness decrease for $\varepsilon > \varepsilon_{max}$. Accordingly, the measurement data between $\varepsilon = 0$ and 0 N tensile force ($\varepsilon = \varepsilon_{max}$) are fitted using a first order polynomial. The data for $\varepsilon < 0$ are fitted using a third order polynomial.

$$F = \begin{cases} k_{l1}\varepsilon + C, & \text{if } \varepsilon \geq 0 \\ k_{nl3}\varepsilon^3 + k_{nl2}\varepsilon^2 + k_{nl1}\varepsilon + C, & \text{if } \varepsilon < 0 \end{cases} \quad (5.3)$$

where F is the tension force exerted by the McKibben muscle, k are the elongation stiffness coefficients and C is a constant depicting the tension force at $\varepsilon = 0$. To obtain a continuous function the constant C is equal for both cases. The rapid stiffness decrease for $\varepsilon > \varepsilon_{max}$ is achieved by assigning a low bending stiffness to the McKibben muscle elements which leads them to immediately buckle under compressive loads.

When McKibben muscles contract their diameter expands. However, at the tips where the McKibben muscles connect to the brackets the diameter is fixed to its initial value. This results in a region where the diameter transitions from the initial value to the contraction dependent value of the uniformly cylindrical portion. Due to this geometry constraint the deformations at the non-cylindrical tips are restricted which leads to a loss of contraction capability with respect to a purely cylindrical McKibben muscle [64]. This loss can be expressed as a reduction of the McKibben muscle length l which amounts to twice the difference between the initial radius r_0 and the radius of the cylindrical portion r [36].

$$l' = l - 2(r - r_0) \quad (5.4)$$

where l' is the corrected length.

5.2.6 Simulation

A single actuator unit of the mechanism shown in Figure 5.1 is modeled in the flexible multibody dynamics software package SPACAR [29] using finite two-node beam elements, which include geometric nonlinearities and flexibility formulated in discrete deformation modes. The flexure strip is modeled as a chain of flexible beam elements with rectangular cross-section. The brackets and the reinforced section are modeled as rigid beams. When $p \leq 0.01$, the reinforced section is omitted. The McKibben muscles are implemented as chains of beam elements with circular cross-section, which feature the stiffness properties described in subsection 5.2.5.

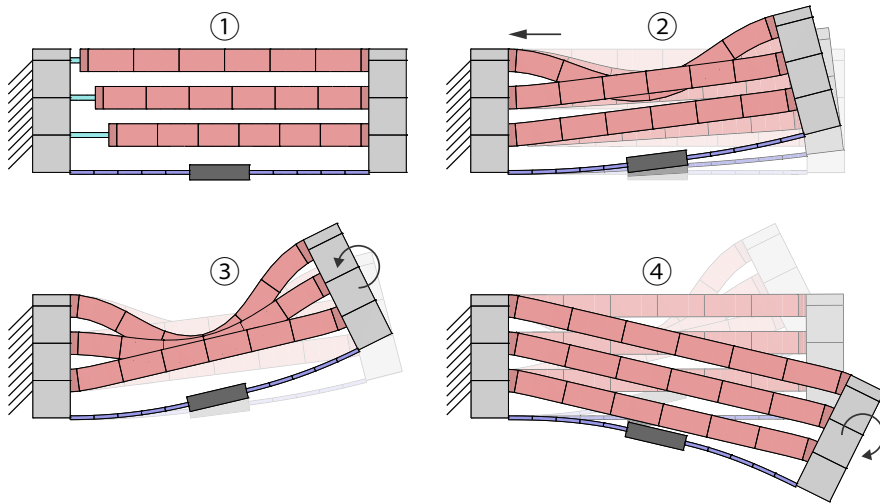


Figure 5.2: Two-step simulation procedure. The top two sub-figures show the pre-loading of the McKibben muscles from state 1 to state 2 by shortening the pre-loading beam elements, depicted in teal. The bottom two sub-figures show the primary load case, where the rotation φ is applied to the right bracket - first in positive direction (state 3) and consecutively in negative direction (state 4). Beam element borders are indicated by solid black lines. The remaining color coding is identical to Figure 5.1.

Furthermore, their lengths are corrected using the minimum and maximum radii 1.5 and 2.5 mm, respectively, which yields a tip length of 1 mm reducing, the initial McKibben muscle lengths l_{init} by an absolute value of 2 mm. The McKibben muscle elements are inserted into the model at their corrected minimum contracted length for the given pressure. This is done to achieve zero tension force at that length ($\varepsilon = \varepsilon_{max}$) as well as buckling for smaller lengths ($\varepsilon > \varepsilon_{max}$). The inactive tip portions are appended to each side of the McKibben muscles. These feature the same bending stiffness as the active portion but have an infinite elongation stiffness.

With this model kinetostatic simulations are performed to determine the significant characteristics of a specific actuator design. This is done in a two-step procedure, depicted in Figure 5.2. First, the McKibben muscles are pre-loaded using rigid beam elements that extend from one end of the contracted McKibben muscles to the bracket. The rigid elements shorten to zero length applying tension to the McKibben muscles. This is equivalent to pressurizing the McKibben muscles, given they were directly connected to the brackets.

This pre-loaded state marks the initial step of the primary load case in which the left bracket of the actuator unit is fixed while the right bracket is rotated by an angle φ , which is first applied in positive and consecutively in negative direction. The amount of rotation, i.e., the range of φ is set using the flexure length l and the desired minimum bending radius $\rho^* = 80$ mm, applying an additional 50 % margin.

$$\varphi \in \left[-1.5 \frac{l}{\rho^*} \dots 1.5 \frac{l}{\rho^*} \right] \text{ rad} \quad (5.5)$$

5.2.7 Optimization

Using the computational model which is described in the previous subsection 5.2.6 the mechanism is optimized to maximize the moment M at the position $\varphi = 0$ rad which, given the intended actuator placement, corresponds to an arm elevation angle of 90 deg. Thus, the objective is

$$\delta = M_{(\varphi=0)}^{-1} \quad (5.6)$$

In order to meet the requirements set in subsection 5.2.1 and to obtain a feasible design, penalties \mathbf{p} are multiplied with a penalty coefficient $k_p = 10^5$ and added to the objective. The first penalty applies in case the bending radius ρ does not reach the desired value ρ^* before one of the McKibben muscles is fully extended. The bending radius is determined by fitting a circle tangentially to the centers of the brackets.

$$\mathbf{p}_1 = \begin{cases} 0, & \text{if } \rho - \rho^* \leq 0 \\ \rho - \rho^*, & \text{if } \rho - \rho^* > 0 \end{cases} \quad (5.7)$$

$$\rho = \left(\frac{l}{\varphi(\varepsilon=\varepsilon_{max})} + \left(\frac{b}{2} \right)^2 \right)^{1/2} \quad (5.8)$$

The second penalty applies in case the von Mises stress in the flexure exceeds a limit value σ_{max} . The von Mises stress is determined for each load step where $0 \leq \varepsilon \leq \varepsilon_{max}$.

$$\mathbf{p}_2 = \begin{cases} 0, & \text{if } \sigma_{mises} - \sigma_{max} \leq 0 \\ \sigma_{mises} - \sigma_{max}, & \text{if } \sigma_{mises} - \sigma_{max} > 0 \end{cases} \quad (5.9)$$

$$\sigma_{max} = \frac{\sigma_t}{FOS} \quad (5.10)$$

where σ_t is the tensile strength of the flexure material and $FOS = 1.2$ is applied as a factor of safety.

The cost function for the minimization problem thus becomes

$$f(\mathbf{x}) = \delta + k_p(\mathbf{p}_1 + \mathbf{p}_2) \quad (5.11)$$

According to this cost function ideal parameter sets \mathbf{x}^* are determined using the Genetic Algorithm function $ga()$ from the MATLAB Global Optimization Toolbox.

5.2.8 Specimens

To validate the simulation and optimization results, physical specimens based on the optimized results for the flexure thicknesses 0.3, 0.4 and 0.5 mm are manufactured and tested. The used materials are described in subsection 5.2.3. Each specimen consists of one flexure, three McKibben muscles and seven individual parts which are produced in ABS via fused deposition modeling on a Zortrax M200 and M300.

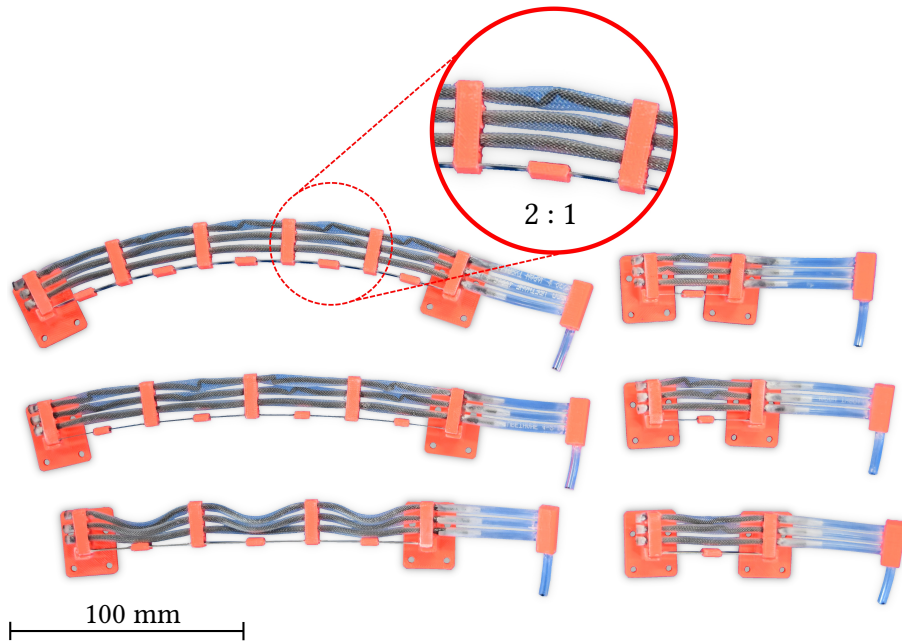


Figure 5.3: Test specimens. Multi-unit specimens are shown to the left and the respective single-unit specimens to the right. Flexure thicknesses from top to bottom: $t = 0.3, 0.4$ and 0.5 mm.

All parts are joined together using Loctite 401 instant adhesive. Two ABS parts are glued to the flexure which form a brace that contains the stiffeners as well as the frames for each bracket. The McKibben muscles are sealed off to one side and routed through and fixed to a chain of $5 \times 5 \times 5$ mm brackets with 3 mm through-holes. For each McKibben muscle the space between the brackets is set according to their computed length at rest l_0 . Correct spacing between parts is achieved by thin struts that are removed after assembly.

At the open end of the McKibben muscles 50 mm long pieces of polyurethane tube are attached as pressure inlets. The individual tubes lead to an ABS manifold part where they are merged into a single tube which connects to the pressure supply. Subsequently, the brackets are placed inside and glued to the bracket frames. In doing so the correct amount of pre-contraction is applied to each McKibben muscle. At both terminal points of the actuator interface parts are attached, which are used to mount the actuator to the test setup using M3 bolts.

For each flexure thickness one actuator consisting of a single unit and one consisting of multiple units is produced. The number of units is determined such that the actuator can attain a total deflection of at least ± 90 deg. All six tested physical specimens are shown in Figure 5.3.

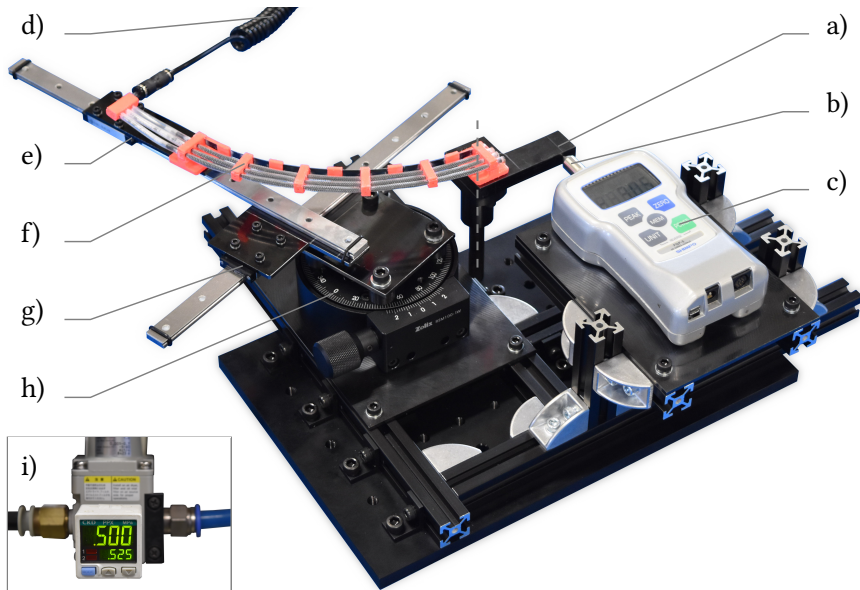


Figure 5.4: Experimental setup to measure the pressure and angle-dependent moments. a) lever (rotary axis indicated by dashed line), b) conical tip, c) force gauge, d) coiled tube (pressure supply), e) linear guide 1, f) specimen, g) linear guide 2, h) manual rotary stage, i) regulator.

5

5.2.9 Test Setup

To test the angle-dependent moment characteristic of each actuator a dedicated test setup, shown in Figure 5.4, is built which emulates the load conditions set in simulation. The test specimen is fixed on one end to a linear guide, connected to a second linear guide which is oriented perpendicular to the first and in turn is connected to a Zolix Instruments RSM100-1W manual rotary stage. This arrangement enables the application of precise rotations without imposing translational constraints within the plane. Therefore, only a moment is transmitted and measured. The other end is fixed to a lever made from 10 mm thick steel plate which rests on a flange that connects to a shaft via two ball bearings. The rotation of the lever is unilaterally blocked by a Nidec-Shimpo FGP-5 digital force gauge which connects to the lever via a cone shaped tip which is placed at a distance of 50 mm from the rotation axis. In this way, the moments exerted by the actuator onto the lever can be accurately measured.

All elements of the test setup connect to each other via 3 mm thick steel mounting plates, 20x20 mm aluminum extrusions and a 10 mm thick aluminum optical plate which forms the base of the setup. Pressure to the McKibben muscles is supplied through a coiled tube which is suspended from the ceiling to minimize external moments and forces exerted onto the test setup. The pressure is supplied by a ANEST IWATA SLP-07EED air compressor and controlled using a CKD RP1000-8-07 precision regulator.

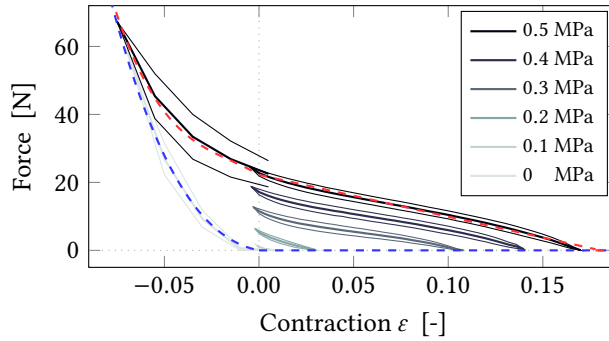


Figure 5.5: Isobaric McKibben muscle stiffness. The thin solid lines represent the mean of five consecutive measurements (counter-clockwise direction), the thick solid lines their average, i.e., the center of the hysteresis field. The blue and the red dashed lines show the fitted stiffness models for 0 and 0.5 MPa, respectively, which are used in the simulations.

Table 5.1: McKibben muscle stiffness model

P MPa	k_{l1} N/ϵ	k_{nl3} N/ϵ^3	k_{nl2} N/ϵ^2	k_{nl1} N/ϵ	C N
0.5	-123.03	-127033	-5669.1	-337.5	22.219
0	0	-57212	6090.7	-110.71	0

5.2.10 Experiment

Using this test setup all six test specimens are characterized under quasistatic conditions at inlet pressures of 0 and 0.5 MPa. The specimens are fixed to the setup at a zero deflection angle and the inlet pressure is set to the specified value using the regulator. The angle is manually adjusted in intervals of 2 and 5 deg for the single-unit and the multi-unit specimens, respectively, and the force is read from the force gauge display.

First, the angle is adjusted from its initial position at the zero angle to the minimum negative angle, then to the maximum positive angle, and back to the zero angle. These minimum and maximum angles are either the values of maximum von Mises stress as determined in simulation for the specific specimen or are dictated by the test setup which is limited to a range of -35 to 100 deg, before its components collide. The procedure is repeated five times for each specimen and the data of the five measurements are averaged to obtain the characteristic angle to moment behavior of the respective actuator.

Table 5.2: Optimized parameters

t mm	l m	p -	ε_{init_A} -	ε_{init_B} -	ε_{init_C} -	$M_{(\varphi=0)}$ Nm
0.9	0.0132	0.0008	0.1576	0.1653	0.1796	0.0344
0.8	0.0319	0.0535	0.0578	0.1106	0.1596	0.1999
0.7*	0.0451	0.0557	0.0471	0.1008	0.1489	0.2380
0.6*	0.0495	0.0202	0.0408	0.094	0.1421	0.2630
0.5*	0.0453	0.1566	0.0489	0.0994	0.1467	0.2431
0.4	0.0389	0.1569	0.0472	0.1014	0.1498	0.2347
0.3	0.0311	0.2699	0.0547	0.1074	0.155	0.2100
0.2	0.025	0.7064	0.0625	0.1149	0.1645	0.1826
0.1	0.0183	0.8103	0.0721	0.1203	0.1711	0.1540

*McKibben muscle intersecting flexure in simulation

5.3 RESULTS

The stiffness of the McKibben muscle, measured according to subsection 5.2.3, as well as the modeled stiffness are shown in Figure 5.5. The parameters of the stiffness model fitted according to subsection 5.2.5 are presented in Table 5.1.

The optimized parameters and moments at $\varphi = 0$ rad for the individual actuator configurations are given in Table 5.2. Several trends can be observed. With increasing flexure thickness t , the moment $M_{(\varphi=0)}$ and the length l increase. Conversely, with the exception of $t = 0.5$ and 0.4 mm which have similar values, the relative size of the stiffer section p decreases and the values of ε_{init} also decrease. However, all these trends are broken and mostly reversed at $t \geq 0.7$ mm.

The simulated angle-dependent moment curves of the optimized designs for $t = 0.3$, 0.4 and 0.5 mm are shown in Figure 5.6. To illustrate the contribution of each McKibben muscle to the total moment of the actuator, the figure also shows simulation data for the cases when either only McKibben muscle A, or the combination of McKibben muscles A and B are used in the computational model. To further exemplify this Figure 5.7 shows the angle-dependent tension force of each McKibben muscle for all three flexure thicknesses.

The experimental results for the specimens with $t = 0.3$, 0.4 and 0.5 mm thickness are shown in Figure 5.8. The respective measured moments at the straight position ($\varphi = 0$) are 0.246, 0.256 and 0.312 Nm for the single-units and 0.220, 0.274 and 0.270 Nm for the multi-units. The physical geometries were measured, revealing that the value of h_m in all test specimens is significantly larger by 0.71, 0.76 and 0.85 mm (14.2 %, 15.1 % and 17.1 %), respectively. Therefore, simulations with adjusted h_m were conducted and presented as well in Figure 5.8. The root-mean-square errors (RMSE) between the measurements and the corrected simulation data are presented in Figure 5.8, and are in the range between 0.013 and 0.049 Nm.

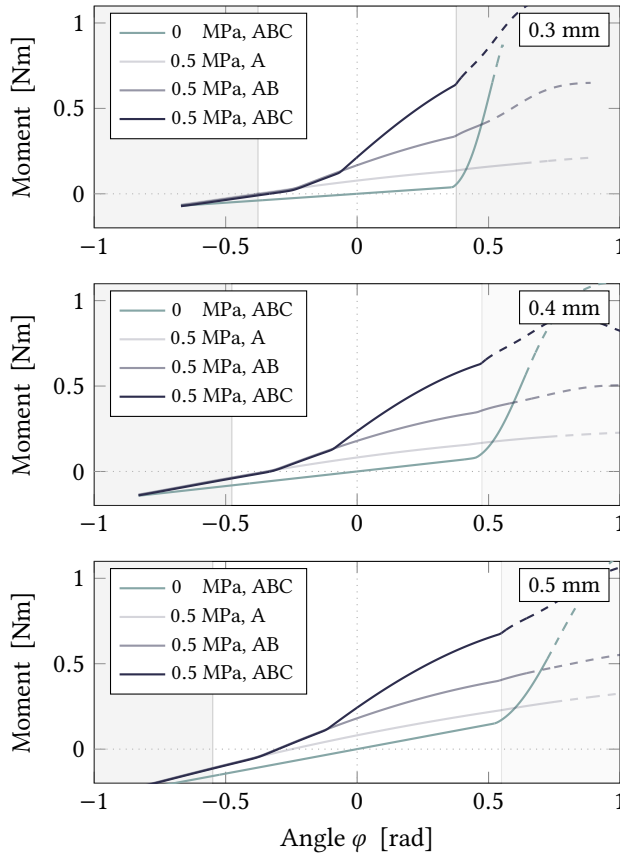


Figure 5.6: Simulated moment response curves. From top to bottom: $t = 0.3, 0.4$ and 0.5 mm. The solid lines transition into dashed lines at the point where the maximum von Mises stress is exceeded. The normal operating range, i.e., the range in which the absolute bending radius $|\rho|$ is ≥ 80 mm, is highlighted by a white background while the shaded areas indicate the regions outside of this range. The thin dotted lines indicate $\varphi = 0$ and $M = 0$, respectively. From this figure it can be seen that the McKibben muscles start contributing to the overall stiffness at different angles, beginning with muscle A and ending with muscle C, shortly before $\varphi = 0$. The stiffness added by each consecutive McKibben muscle increases with respect to the prior ones. Beyond the upper end of the operating range a rapid increase in stiffness can be observed for the ABC curves, while the AB curves exhibit only a slight and the A curves no increase, which points to McKibben muscle C being the main cause.

To illustrate a potential application of the actuator, a wearable proof-of-concept prototype based on the optimized design for $t = 0.4$ mm is built and is shown in Figure 5.9. Its unilateral actuator is 80 mm wide, giving it a theoretical moment output of 3.76 Nm at 90 deg arm elevation which is 41 % of the required moment to lift a fully extended arm.

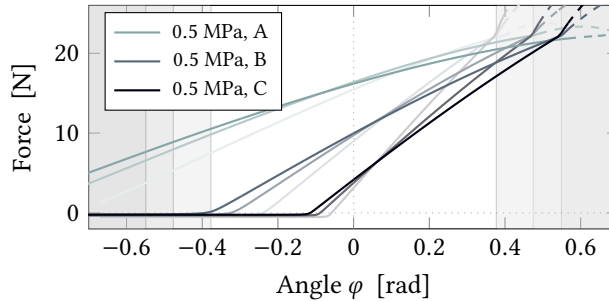


Figure 5.7: Simulated force response curves. From light to dark: $t = 0.3, 0.4$ and 0.5 mm. The solid lines transition into dashed lines at the point where the maximum von Mises stress is exceeded. The shaded areas adhere to the same color grading and indicate the respective regions outside of the normal operating range. The thin dotted lines indicate $\varphi = 0$ and $F = 0$, respectively. This figure shows that optimized designs are characterized by the force curves of all McKibben muscles intersecting at a point close to the end of their respective operating range, after which the stiffness of muscles A and B increases. The force exerted at these intersection points is similar across all McKibben muscles and optimized designs, yet occurring at different angles.

5.4 DISCUSSION

The results support that the presented synthesis method is suitable to obtain bending actuators with maximized moment outputs for a given set of components. Generally, it can be stated that a larger flexure thickness increases the buckling resistance and bending stiffness, but also the bending stress at a given bending radius. Due to the increase in buckling resistance, the flexure itself can withstand higher compressive forces exerted by the McKibben muscles. Furthermore, the McKibben muscles together with the flexure can become longer and the reinforced section shorter. This allows for a larger moment at $\varphi = 0$ rad, while maintaining the necessary ROM. Adversely affecting this, however, is the bending stress which for flexure thicknesses $t \geq 0.7$ mm and the required minimum bending radius of $\rho^* \leq 80$ mm apparently becomes the limiting factor to the acquirable moment at $\varphi = 0$ rad.

The effect of increasing bending stiffness is ambivalent. While it passively provides a moment that counteracts gravity, and thereby relieves the McKibben muscles and lowers the energy requirement, it could become disadvantageous in an assistive device, if considerable force is required by the user to reach the full natural ROM. The flexure thicknesses $t = 0.3, 0.4$ and 0.5 mm were chosen for evaluation, as their stiffnesses appeared to lie within a favorable range.

For longer flexure lengths the simulation showed intersection of the flexure and McKibben muscle A. To avoid this an intersection penalty could be added, contact modeled and h_m adjusted or used as a design variable. However, for the specimens with flexure thickness $t = 0.5$ mm no negative effect of this could be observed during experiments.

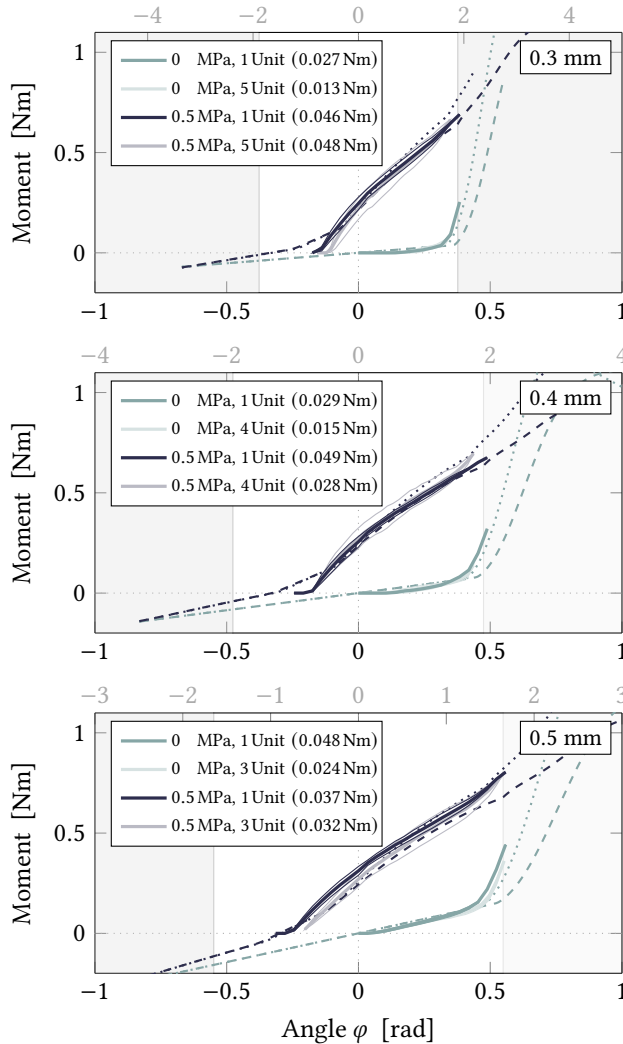


Figure 5.8: Experimental results. From top to bottom $t = 0.3, 0.4$ and 0.5 mm. The thin solid lines represent the mean of five consecutive measurements (clockwise direction), the thick solid lines their average, i.e., the center of the hysteresis field. The dashed lines show the simulated moment curves using the optimized parameters. The dotted lines show the simulated moment curves using the measured values for the parameter h_m . The normal operating range is highlighted by a white background while the shaded areas indicate the regions outside of this range. The thin dotted lines indicate $\varphi = 0$ and $M = 0$, respectively. The multi-unit result angles are divided by the number of units. Their actual angles are indicated in gray on the top. The root-mean-square error (RMSE) for each measurement with respect to the corrected simulation data (dotted line) is shown in brackets. These results show that the experimental results for both single units and multiple units generally show good agreement with the simulated results, if the measured geometric dimensions of the physical specimens are applied in the computational model.



Figure 5.9: Wearable proof-of-concept prototype worn by a healthy subject. This figure illustrates the actuator's potential to achieve close alignment to the body and an overall small size of the resulting assistive device.

With respect to the experimental validation some uncertainties remain. In the tension tests it was difficult to determine the exact absolute position that corresponds to a zero contraction ratio. Consequently, the measured stiffness curves, shown in Figure 5.5, may be slightly shifted along the x-axis with respect to reality. This, along with the manufacturing inaccuracies are probably the main reasons for the discrepancies between the simulated and the measured behavior of the actuators. In comparison to the initial predictions, the moments at $\varphi = 0$ rad are 5 to 28 % higher and the onsets of the rapidly increasing stiffness occur up to 7 and 21 deg earlier for the single-unit and multi-unit specimens, respectively. Adjusting the parameter h_m according to the measured geometry improved the match to a maximum deviation of 4 and 11 deg, respectively.

The wearable prototype illustrates the potential of this actuator design regarding its size and close-to-body alignment. However, using the currently available components it is likely too weak for practical purposes. By using the design for $t = 0.6$ mm its theoretical moment output could be raised to 4.21 Nm, i.e., 46 % of the required moment.

Considering the values of ε_{initC} which all approach the limit $\varepsilon_{max} = 0.1806$, adding a fourth McKibben muscle of the same type does not seem a feasible option to further increase the moment at $\varphi = 0$ rad. Therefore, to improve the performance the active components need to be revised. To this end, the maximum contraction ratios of the McKibben muscles could be customized according to their height above the flexure, e.g., by adjusting the braid angles. This would potentially also enable the use of additional McKibben muscles along the height. Alternatively, the pneumatic McKibben muscles may be replaced by more powerful alternatives, such as hydraulic artificial muscles or cable-based actuation systems.

The actuator concept can potentially be applied to other joints of the human body, as well. This, however, will in most cases require the actuator to be optimized for different bending angles and radii. If two-way actuation is required, McKibben muscles could be placed to either side of the actuator, or an antagonistic pair of unilaterally acting actuators could be used.

5.5 CONCLUSIONS

The pneumatic bending actuator proposed in this chapter is the first to combine McKibben muscles with flexures, resulting in a leveraged large rotational range of motion and reduced localized forces at the attachments. A method is presented to optimize the actuator design towards a maximum output moment, given a set of basic components and initial design specifications. The computational results are verified by experiments, displaying the ability of this actuator to provide assistance while allowing for a natural range of motion in the actuated degree of freedom. Its close-to-body alignment and potential for building small size upper-limb assistive wearable robots is illustrated by means of a proof-of-concept prototype. When employed on an upper-limb wearable robot and given a width of 80 mm, the optimized designs can theoretically produce a moment of up to 4.21 Nm at 90 deg arm elevation.

5.6 APPENDIX

5.6.1 Supplementary Files

- **Supplementary file 1 — `supp1-2975732.mp4`**
Video showing the actuator concept, animations of the optimized results, the experimental setup as well as the wearable prototype.

The downloadable supplementary materials are available at:

<https://research.utwente.nl>

Digital Object Identifier 10.3990/1.9789036551342

High image resolution movies (450 MB)

<https://ieeexplore.ieee.org>

Digital Object Identifier 10.1109/LRA.2020.2975732

Standard image resolution movies (20 MB)

For alternative links and additional materials, visit: <https://tschiersky.org/dissertation>

File Name : supp1-2975732.mp4
Duration : 00:02:59

00:00:00

A Compact McKibben Muscle Based Bending Actuator for Close-to-Body Application in Assistive Wearable Robots

Marin Trichersky, Edsko EG Holman, Dennis M Brouwer, Just L Herder and Koichi Suzumori

JSPS P192019 (P1919704)
 H2020-ICT-2019 SC4Pro (No. 688857)

00:00:33 **Optimized Results**

t = 0.3 mm t = 0.4 mm t = 0.5 mm

single unit

00:00:40 **Optimized Results**

multi unit t = 0.5 mm

00:01:02 **Angle vs Moment Test**

t = 0.5 mm
 multi unit
 4x speed
 P = 0.5 MPa

00:01:32 **Isometric Moment Test**

t = 0.5 mm
 multi unit
 1x speed
 P = 0.5 MPa

00:01:55

00:02:09 **Passive Range of Motion**

Pressure: off

00:02:18 **Active Range of Motion**

Pressure: on

00:02:36 **Active Range of Motion**

Pressure: off

00:02:57 **Preliminary Test**

Pressure: off
 Muscles: relaxed
 Equilibrium

5
A

Preview: Supplementary file supp1-2975732.mp4

CHAPTER 6

Discussion

This thesis explored the application of flexure-based mechanisms for upper-limb support in passive and active wearable assistive devices. Though the synthesis process shares many similarities across all presented devices, the functional requirements and consequent design challenges differ considerably between passive and active mechanisms. This discussion, therefore, first addresses the two parts separately, before discussing aspects pertaining to both.

6.1 PASSIVE MECHANISMS

The main function of the passive mechanisms presented in this thesis is to store and release elastic strain energy in an appropriate manner, and exert the necessary forces and moments to provide gravity balancing to the upper limb. Compared to linear springs which are traditionally used in gravity-balancing orthoses, bending elements like the flexures used in this thesis have the ability to exert forces not only along their length, but also perpendicular to it. In addition, they can also transfer moments, which combined properties enable complex mechanical loading. Previous works showed that this can be used to achieve gravity-balancing properties by simply tweaking the shape of the flexible structure [9, 10, 54, 55, 56].

In contrast to previous works, however, this thesis pursued the goal of finding flexible structures that are wearable. Thus, they should remain in close proximity to the body throughout the functional range of motion, be compact, lightweight and preferably usable without the addition of a load-bearing rigid-link structure. This means that aside from exhibiting a minimum balancing error, the protrusion distance to the body should be minimized while avoiding harmful collision, the overall volume and weight should be minimized while still achieving the necessary performance, and all interface forces and moments that do not directly contribute to the balancing behavior, but especially forces parallel to the skin, should be minimized as well.

6.1.1 Protrusion and Collision

To minimize protrusion and avoid harmful collision, the main strategy employed in this thesis was to confine the flexible element to certain areas during deflection. In Chapter 2, initially a simple rectangle was used to specify the accessible areas around the supported joint. This still left ample design freedom with regards to flexure shapes, as not even the position with respect to the supported joint was specified. However, the resulting flexure designs quickly showed that this type of constraint would not suffice when considering cases in which the flexure should wrap around the body.

For example, the presented design **Set A**, shown in Figure 2.7-a, passes through the pivot of the supported joint when deflecting. This, in practice, forces a lateral placement of the spring, as it would otherwise inevitably collide with the wearer.

To prevent this, a circular area around the joint was subtracted from the feasible region and the undeformed flexure was forced to enclose this area. When using a constant thickness along the flexure, however, enforcing this new constraint would lead to significant degradation of the balancing quality. The solution to this problem was to allow for local thickness variations, and thereby influence the stiffness along the length of the flexure. Thus, with **Set B** a design could be obtained that encloses the supported joint while preserving a very good balancing quality. The final design of the elbow balancer in Chapter 2 has a variable thickness, but does not wrap around the body, as for the presented use case a lateral placement as well as increasing the energy density through additional nested springs appeared more advantageous.

For Chapter 3 significantly more stringent spatial constraints were applied. For this study, the flexure was forced to wrap around the wearer's torso while being restricted to a limited distance from the body. The results show that the solution found in Chapter 2 would not suffice to find designs with low protrusion and no collision. Considering the *Clamp-Clamp* case which is most equivalent to the configuration used in Chapter 2, only designs with more than 29 cm of maximum protrusion were found. A large scope investigation into different mechanism topologies revealed, that changing the support conditions of the flexure element can lead to designs with significantly less protrusion. In particular, a design with a spring-loaded slider and a hinge at the back of the wearer, and a clamped connection at the arm yielded the most promising results, featuring a maximum protrusion below 10 cm. In this and similar designs, close alignment is maintained while collision of the flexure with the adjacent body is avoided by changing the position of the back attachment, and thus aligning the bending flexure with the curvature of the body, particularly in the areas around the shoulder.

Apart from these two strategies, two other approaches have been explored. The first was to enable spatial flexure designs. The second was to allow for limited collision with the wearer's body. Extrapolating from the experience made in Chapter 2, the assumption was made that by simply offering more design freedom to the flexible element lower levels of protrusion would be attainable. Consequently, spatial flexure designs were considered which featured additional parameters for modeling bending in a second direction and torsion along the flexure. An intermediary result of this design approach is the Prototype 1 which is presented in Chapter 4, and can be seen in Figure 4.3 and Figure 4.5. This design offers relatively good close-to-body alignment, but otherwise fails to provide significant gravity support, and furthermore shows mild collision with the body. Aside from spatially curved flexures based on beam elements, also the use of doubly curved shell elements was briefly investigated, but quickly disregarded due to the significantly increased computation time for each simulation. Moreover, in practice no discernible benefit of using spatially curved flexure elements was observed during these preliminary investigations, and the increased solution space due to the additional design parameters severely hampered the search for suitable solutions. Therefore, in the end only planar mechanisms were considered.

As increasing the complexity of the flexure geometry did not provide the anticipated results, allowing contact between the flexure and the wearer was hypothesized to be another suitable means for achieving better close-to-body alignment. Several different ways of implementing contact into the simulation analysis were tested, eventually leading to a relatively stable and performant implementation. However, the increase in computation time for the contact simulation was still in the orders of magnitudes. In addition, open questions remained to what degree contact would be tolerable, also with respect to sliding and the resulting friction forces, and how negative stiffness could be created when the flexure gradually transitions into contact with the wearer. Hence, this approach was also disregarded.

6.1.2 Volume and Weight

Reducing the total volume and weight of the balancing mechanism are important aspects to increase the portability and wearability of the resulting devices, and are also instrumental in reducing protrusion, which is addressed in the previous subsection. Still, it is crucial that the necessary absolute performance of the mechanism to fulfill its function is maintained. Hence, the stored strain energy and assistive output moment relative to the volume and weight of the mechanism become important factors.

To that end, using a variable thickness along the flexure length appears to be inherently advantageous. In Table 2.1 of Chapter 2 it can be seen that, compared to design **Set A**, **Set B** has a specific energy that is roughly double and an energy density that is nearly four times as high.

The increased specific energy points towards a more efficient use of the material achieved by a more uniform stress distribution, which can be visually verified by comparison of Figure 2.7-a and Figure 2.7-b. In addition to that, the design with variable thickness features a larger material cross-section with respect to the occupied in-plane area, thus has a larger material volume relative to the occupied space. Hence, in addition to the better material utilization which is expressed by the specific energy, this increased space utilization explains the even higher gains in energy density.

To further increase the cross-sectional area, concentric nesting of differently sized springs proved to be a suitable means. In comparison to **Set B** with a single spring, the effective cross-sectional area of design **Set C** is significantly increased. Thereby, as can also be seen in Table 2.1, the energy density was increased by more than twofold, however, without affecting the specific energy. Still, as a prerequisite for this nesting technique the original design must be concentric around the supported joint, as the individual springs are scaled with respect to the that joint. Otherwise, scaled springs would intersect each other, making the nesting approach infeasible. Moreover, as the enclosed volume is occupied by the additional springs, nesting generally implies a lateral placement of the spring.

Another approach that seems promising to reduce the size and weight of the flexure component specifically, is to employ dedicated energy storing elements in series at the interfaces. Though the data do not provide a consistent picture, Table 3.2 together with Table 3.4 in Chapter 3 show that the highest relative strengths are achieved by the mechanisms that mainly rely on their interfaces for storing energy.

In this case, the benefit of the better energy storing capabilities of elements like rubber bands may be exploited. However, since a key benefit of flexures is their potential for function integration, a more holistic system-level view must be applied, comparing the volume and weight of all components to the achieved performance. To this end, the added volume and weight of the energy storing mechanisms at the interfaces, including elements like dedicated springs, hinges and sliders, must be taken into account.

6.1.3 Interface Forces and Moments

To achieve complete function integration and reap the full benefits of a flexure-based architecture, the use of additional load-bearing structures such as rigid-link orthoses should be avoided. The mechanisms presented in Chapter 2, though presumably outperforming any similar preexisting flexure-based gravity-balancing mechanism in terms of energy density and specific energy, still rely on a rigid structure to which they can attach to. Since their springs exert relatively large forces onto the supported joint, a design without an additional external structure to absorb these remains infeasible, as otherwise transferring these large forces via the skin to the anatomical joint of the body would likely induce uncomfortable and potentially harmful skin shear, and could furthermore have negative long-term effects on the anatomical joint which has to bear these loads. Therefore, in their current form the mechanisms from Chapter 2 do not offer an obvious practical advantage in comparison to simpler conventional designs, as for example the rubber band based solution used in the shoulder balancing mechanism shown by Chen and Lum [7, 8].

To avoid the use of separate dedicated load-bearing structures and enable completely integrated designs, all interface forces and moments that are not necessary for gravity balancing, and in particular forces parallel to the skin surface which – in the absence of a load-bearing structure – induce skin shear and make tight attachments to the body necessary, ought to be minimized. In that regard, special emphasis should be placed on the arm interfaces, as in comparison to the torso less surface area is available to transmit loads via the skin to the musculoskeletal system. Table 3.2 in Chapter 3 shows that based on the applied support conditions at the interfaces, the shear force at the arm attachment interface assumes different levels. To that effect, the ability to transmit moments to the arm appears to be a key requirement to reduce shear forces. The absolute lowest interface forces were observed for the designs that feature a slider at the back of the wearer. To this end, the ability of the back interface to undergo large translations while storing energy seems to provide a decisive benefit.

6.1.4 Future Work

Depending on the use case, the recommendations for future work vary, as the challenges regarding spatial constraints and size differ profoundly between laterally aligned designs and the body-enclosing designs.

If a lateral placement of the balancing mechanism is chosen, the main focus should be on further downsizing the mechanism and finding more suitable aspects

ratios which minimize protrusion. Moreover, minimizing the shear forces at the interfaces should be the second priority in order to make do without a rigid-link orthosis in parallel. A frameless design may not only result in an overall lighter device, but could also make it more self-adapting to different body shapes and less prone to harmful misalignment. Achieving this would give such flexure-based devices a decisive advantage.

In addition, choosing different flexure spring materials may also have a positive impact. Choosing a spring material with a higher Young's modulus would lead to overall thinner individual springs. This would allow for a higher nesting density, i.e., a larger number of springs within the same envelope. However, the effect of this on the achievable energy density remains to be investigated. Also, thinner springs can have a negative impact on manufacturability, as the minimum thickness is generally limited by the manufacturing method. This affects the minimum achievable spring size, as exemplified by the nested design **Set C** shown in Figure 2.8 which features an area of unutilized space at its center. On the other hand, a smaller Young's modulus results in thicker individual springs. This would result in an increased material volume for the same in-plane footprint, and may improve manufacturability for smaller springs. Also, the combination of different materials may be investigated, e.g., in a laminated composite structure to homogenize the stress over the flexure thickness. In any case, to prevent gradual degradation of the mechanical behavior, the material or material combination should not exhibit any significant creep or stress relaxation.

When opting for a complete redesign of the laterally placed mechanisms from Chapter 2, the insights from Chapter 3 should be incorporated. More specifically, designs should undergo a second optimization step aimed at increasing the strength, and different support conditions for the springs should be explored. As in Chapter 3, the latter may be used to potentially discover designs that feature reduced interface forces, and thus mitigate the need for a rigid-link structure in parallel to the limb. Yet, in contrast to Chapter 3, the second optimization step should also take the achievable nesting density into consideration, as this proved an essential means for achieving large energy densities. To this end, reducing the thickness variation and favoring shapes that are mostly circular, i.e., equidistant to the joint may be two strategies towards high nesting densities. Especially the latter is important to prevent the formation of large voids that occur due to the different scaling behavior of the flexure's neutral axis and its thickness, as can be seen at the static interface of design **Set C**, best visible in the preview of supplementary file 7 in Chapter 2.

For a design in which the flexure encloses the body, simple downsizing and nesting are no viable options. Generally, the optimal size for these mechanisms is prescribed by the body dimensions of each individual wearer, making the need for mass customization a potential issue in the later stages of development. In contrast to the laterally placed mechanisms, investigating materials with different Young's modulus also appears less beneficial, as both nesting and manufacturability are typically not an issue. Achieving a lower flexure thickness would only have little impact on the overall protrusion. Furthermore, for very thick sections at which the flexible element behaves rigid, additional reinforcements made from different materials could be used to locally reduce thickness without changing the main material.

Instead, primarily a better alignment with the body and better biomechanical compatibility should be pursued for these designs. This includes both bringing the device closer to the body and reducing stiffness in non-supported directions in order to facilitate joint mobility. To this end, the concepts of spatial flexure designs and allowing limited collision with the wearer should be reconsidered and further investigated. Due to restrictions in computational resources and time their full potential could not be revealed within this thesis.

For both laterally aligned and body-enclosing designs the trade-off between the local thickness and width could be exploited for better performance and better biomechanical compatibility. To achieve a higher energy density and specific energy, the thickness in regions that do not experience high stresses could be increased while the width is decreased to maintain the same local stiffness. In the ideal case, a uniform stress distribution would be achieved where all parts along the flexure experience the same maximum stress. Thereby, the amount of material is reduced while maintaining the same function, improving both energy density and specific energy.

To achieve better biomechanical compatibility, the same trade-off could be applied, but with the intentional goal to locally decrease the stiffness in lateral direction to the flexure and thereby facilitate motions in non-supported directions without the use of dedicated joints. Also, when necessary, the trade-off could be applied to avoid excessive protrusion or collision at specific parts of the flexure. These adjustments could be made in a subsequent step and should be generally unproblematic for any planar designs, thus apply to all designs presented in Part I. When considering spatial designs, however, the changes in support stiffness could have negative influence on the overall function.

The relative success of designs with spring-loaded joints in Chapter 3 to some degree contradicts the initial premise of striving towards more integrated, even monolithic design. Some joints, for example elastic hinges, could be potentially integrated into the flexure. However, due to large ranges of motion and specific requirements regarding the stiffness values at the interfaces, many of these designs imply the use of conventional components such as bearings, sliders and dedicated springs. This poses additional design challenges in terms of weight and biomechanical compatibility, but may also offer opportunities. If done correctly, a function separation where the flexure is mainly used as a means for flexible power transmission and as the load-bearing structure while dedicated springs are used for energy storage may even increase the overall performance.

Lastly, the influence of misalignment should be more closely investigated. This is especially critical for designs that lack a dedicated support structure, e.g., in the form of an orthosis. For these, large misalignment can occur during donning of the device. Furthermore, shifting centers of rotation, motion of the attachment relative to the skin and motion of the skin relative to the bone are other sources of potential misalignment that can occur while wearing the device.

6.2 ACTIVE MECHANISMS

Compared to the passive mechanisms, the function of flexures in active mechanisms differs substantially. Though the energy storing capabilities can still be exploited, as shown in Chapter 5, their main function is to provide the kinematic structure of the mechanism.

6.2.1 Buckling and Bending Stress

The two main limiting factors for the performance of the active mechanisms are the critical buckling load and maximum endurable stress of the flexure. In Chapter 5 the flexible members are bent and loaded in compression by the McKibben muscles.

To increase buckling resistance, rather established approaches were implemented. Specifically, reducing the length and increasing the thickness of the loaded members, as well as employing a thicker stiffening section at the center of each member were strategies by which better buckling resistance was achieved. By inverting the load case from compression to tension, buckling could be avoided entirely. However, since McKibben muscles can only exert tension forces, this inversion could not be applied.

Yet, all the previously mentioned measures against buckling also increase the bending stiffness of the respective elastic member. This can have a negative impact on the performance, as more actuation force is necessary in order to induce bending deformations. Furthermore, these measures generally also result in a higher bending stress, and thus potentially reduce the achievable range of motion.

6.2.2 Stiffness and Elastic Energy

The stiffness and the associated elastic energy stored in the mechanism can be both an advantage and a disadvantage. In the bending actuator proposed in Chapter 5 a high bending stiffness can prevent reaching low arm elevation angles, unless using substantial external force. Though the stiffness helps returning the mechanism to its initial state, and thus assists in lifting the arms up to an angle of 90 deg, a low bending stiffness would be generally favorable.

More reasons to favor a low bending stiffness are founded in the limitations of the actuators. When a high bending stiffness is present, a large portion of the force capability has to be spent on deforming the mechanism, which reduces the force that can be transmitted to the load. This is further exacerbated by the fact that McKibben muscles have a direct relation between the exerted load and achievable stroke. Thus, a high stiffness in the actuated degree of freedom inevitably results in a loss of actuator stroke, reducing the range of motion for these mechanisms.

6.2.3 Actuation and Transmission

McKibben muscles are considered to have high-force and low-displacement properties. Thus, the flexure mechanism has to offer a suitable transmission to achieve useful output strokes. In the bending actuator, presented in Chapter 5, the linear motion

of the McKibben muscles is converted into a rotation at both ends of each actuator segment. To this effect, a basic lever principle is applied and the transmission ratio for each McKibben muscle is thus a result of the lever length, i.e., the distance to the flexure. Due to the high force capabilities of McKibben muscles, only relatively short lever lengths are necessary to achieve adequate output moments. This allows for the shallow design which makes this actuator attractive for wearable applications.

However, the power density of the McKibben muscles is still insufficient to achieve the aspired performance characteristics. Thus multiple McKibben muscles have to be stacked on top of each other, to increase the applied moment and extend the supported range of motion.

6.2.4 Future Work

For the bending actuator presented in Chapter 5 the McKibben muscles are currently the largest performance bottleneck. A more powerful alternative to the employed pneumatic McKibben muscles would immediately enable the design of more powerful bending actuators, without any changes to the synthesis method. Promising candidates are hydraulic artificial muscles or tendon-based solutions. Furthermore, finding ways to increase the buckling resistance without affecting the bending stiffness would offer additional performance benefits. A promising approach to that end is the use of spatially curved flexures, e.g., tape springs as used in [22].

Alternatively, also an inverted design might be pursued that would eliminate the risk of buckling entirely, and thus enable designs with thinner flexures, and thus a lower bending stiffness. However, to that end, a soft pushing actuator would need to be employed which has similar or better performance characteristics than the currently employed McKibben muscles. Such actuators are not readily available, and a custom design would therefore be necessary.

Towards practical application of the bending actuator the biomechanical compatibility has to be improved. To this end, decoupling the actuator from internal/external arm rotation and from movement along the arm axis will be necessary. Also, incorporating internal compliance in the lateral width-direction of the actuator may further increase wearing comfort.

6.3 GENERAL REMARKS AND LIMITATIONS

A fundamental limitation of this work is its focus on the mechanism level, be it the passive gravity-balancing mechanisms in Part I or the compliant actuator in Part II. Yet, in order to build fully compliant wearable assistive devices, the ultimate goal would be to incorporate the design of all necessary components, such as structures to absorb and transmit forces and moments, attachments to interface with the body, decoupling mechanisms for releasing passive degrees of freedom, and – with respect to the gravity balancing devices – decoupling mechanisms to achieve correct balancing irrespective of the torso inclination and arm orientation. Without thorough consideration of these aspects, the full potential of the compliant wearable technologies presented in this

thesis may not be realized. Therefore, these areas require further extensive research and development.

In the absence of well-researched and well-developed complementary technologies, only early proof-of-concept prototypes of wearable devices were built. These made use of preexisting orthoses, employed rather rudimentary attachments and mechanisms to release degrees of freedom, and lacked decoupling mechanisms for robust gravity balancing. Furthermore, the employed materials, especially the plastic that was used for the springs in Part I, which exhibited extensive creep and stress relaxation, are unsuitable for long-term use. Consequently, no sufficiently performant prototype was available to reliably assess the technologies' potential under real-life conditions, e.g., in the form of a clinical trial. Therefore, the practical usefulness of these technologies for the proposed use cases remains to be established.

A conceptual approach that was applied to all mechanisms presented in this thesis was to strive for a high degree of integration. While this potentially offers benefits in terms of size, weight and cost, it also has some inherent disadvantages. To that effect, it is much more difficult to make changes to selected aspects of the device, without immediately influencing others. This especially applies to the mechanisms in Part I. These show that functional features like balancing quality, strength relative to size and weight, interface interactions, and maximum protrusion cannot be treated separately, but must always be dealt with holistically. This is in contrast to current commercially available devices where, for example, the balancing mechanism can be adjusted irrespective of the shape of the frame or the nature of the interfaces. Furthermore, the mechanisms in Chapter 3 which have the best overall performance feature interfaces which require dedicated conventional components. Thus, full function integration may not always be a helpful paradigm towards designing the best possible device.

Regarding the synthesis method, all main chapters take an approach in which the mechanism is modeled in the flexible multibody dynamics software package SPACAR, and optimized using gradient-free population-based solvers from the MATLAB Global Optimization Toolbox. While this proved to be an effective approach, it also appears to be very inefficient. Setting up optimization problems as naively as has been done in this thesis can quickly result in a large number of optimization parameters, increasing the dimensionality of the search space and thus hampering the search for optimal results. Furthermore, gradient-free population-based solvers often require a very large number of objective function evaluations in order to converge towards global optima. Thus, meticulous care has to be taken to reduce the computation time for each individual objective function evaluation. To that end, the very efficient beam-theory-based analysis offered by SPACAR played an integral part. However, optimizations still turned out to be very resource-demanding and time-consuming. Thus, for example in Chapter 3, the sample size of successful mechanisms per category is relatively small, compromising the universal validity of the results.

To allow for the optimization of more complex structures, additional measures have to be taken, in spite of the ever increasing available amount of computing power. To that end, future work may incorporate some of the engineering insights which

this thesis has established to model mechanisms more efficiently and thereby reduce the necessary number of design parameters. Also, new computational methods that are within the realm of what is currently referred to as 'artificial intelligence' may offer more efficient alternatives to the solvers used in this thesis.

Conclusion

The goal of this thesis was to explore mechanisms for upper-limb support which employ flexible elements that can be simultaneously used for internal energy storage, for power transmission and as load-bearing structures. These were investigated in detail for their potential to provide passive gravity balancing and concealed actuation in compliant upper-limb wearable assistive orthoses. The added value of using flexible structures was believed to be in their potential for function integration and better biomechanical compatibility, leading to less protrusive and lighter designs which offer an increased wearing comfort. In comparison to traditional rigid-link exoskeletons, the stored elastic energy and the actuation would be distributed throughout the entire structure of the device, rather than being concentrated in localized elements. In doing so, the ultimate ambition was to build devices that would resemble exterior compliant shells – similar to the exoskeletons of insects – which would behave much like a ‘second skin’ while offering full gravity support to the user. Though this ultimate ambition could not be fulfilled, this thesis presents several crucial advances on the path towards it.

Part I presents passive flexure-based gravity-balancing mechanisms for use in wearable assistive orthoses. To this end, Chapter 2 lays the foundation in developing the fundamental methodology by which gravity-balancing flexure mechanisms were synthesized that show superior energy densities and specific energies, and allow for more freedom in the placement of the flexure through better control over its shape at any deformed state. The chapter shows that by changing the local stiffness along the length of the flexure, additional design freedom can be gained to enable adherence to spatial constraints without compromising the balancing quality. Furthermore, using variations in the thickness to that effect, flexures will generally feature a larger material volume relative to the occupied space and a more uniform stress distribution along their length, yielding gains in both energy density and specific energy. As a way to utilize the additional design freedom the chapter presents the method of nesting flexure springs into concentric stacks in order to use more of the available volume, and thereby further increase the energy density. The computational results have been verified via three physical test specimens, each of which represent a distinctive step in the development process, and a proof-of-concept assistive elbow orthosis prototype was built to show the practical applicability of this technology. In doing so, the chapter fulfills three fundamental subgoals of this research track. These are: the development of a synthesis method for gravity-balancing flexure mechanisms, the improvement of the energy density and specific energy, and the handling of basic spatial constraints. While the first subgoal has been previously achieved by other

researchers, the other two subgoals, which are essential to make this type of balancing mechanism viable for use in wearable assistive orthoses, go beyond the previous state of the art. In particular, the approach of using a variable thickness along the flexure element's length is a key differentiator to previous works and was established as a crucial means for achieving the latter two subgoals.

Chapter 3 extends the synthesis methodology of Chapter 2. Within the chapter body-enveloping flexure-based gravity-balancing mechanisms have been synthesized that exhibit no collision with the wearer, have relatively low protrusion from the body and feature reduced shear forces at the interfaces. These are crucial advances to make flexure-based mechanisms more suitable for close-to-body use and to mitigate the need for dedicated load-bearing structures. These improvements were achieved by a systematic investigation of different model topologies. In the course of this investigation different support conditions of the flexure element, representing hinges and sliders with and without an associated spring stiffness, were considered. Apart from providing a comprehensive overview of feasible design topologies, two promising designs were chosen as representative examples for further investigation. These designs, which were reoptimized and validated in experiment, serve to provide an indication of the final potential of this technology. While generally improving on the subgoals of Chapter 2, Chapter 3 addresses three additional distinct subgoals. These are: avoiding collision with the wearer, restricting protrusion from the wearer, and minimizing reaction forces and moments at the interfaces to the wearer. Thereby, the chapter expands significantly on the research of Chapter 2, and thus on the previous state of the art. In particular, the identification of specific support conditions of the flexure element, which improve adherence to spatial constraints and simultaneously reduce interfaces loads, marks a fundamental step in the development towards fully compliant wearable assistive devices. However, while collision can be reliably avoided, allowing for close-to-body arrangements, the protrusion from the body remains still too large to make these devices inconspicuous or even wearable underneath clothing. Furthermore, whether the extend to which the interface forces and moments were reduced suffices to allow for use of these mechanisms without any additional load-bearing elements remains to be established.

Chapter 4, which concludes Part I, presents further illustrative examples of potential applications in addition to the devices shown in Chapter 2 and Chapter 3. To this end, an integrated device utilizing the Assistive Elbow Orthosis (ÆOs) prototype and two wearable shoulder support prototypes provide a practical notion of how the technologies from Part I could be implemented in actual products.

In conclusion, Part I shows that passive flexure-based gravity-balancing mechanisms can be synthesized that are suited to build upper-limb wearable assistive orthoses which can provide ample support, both qualitatively and quantitatively, and can be competitive with traditional rigid-link devices in terms of size and weight. With respect to the previous state of the art in compliant gravity-balancing mechanisms for use in upper-limb orthoses, significant improvements in terms of performance, close-to-body alignment and biomechanical compatibility have been made. However, the present amount of protrusion still prevents these devices from being wearable

underneath clothing. Furthermore, the use of additional components, such as springs, hinges and sliders to allow for closer alignment and to mitigate undesired interface forces and moments, may increase size, weight and the overall design complexity.

Part II presents an active flexure-based mechanism. Chapter 5 demonstrates that, by using McKibben muscles acting against a parallel flexure, a semi-soft bending actuator with a low height can be built that potentially enables the design of actuated assistive devices which are wearable underneath clothing. The modular design, in which individual cells can be arranged in parallel and in series, enables distribution of the actuator across the available body surface. This allows for close-to-body arrangements, as is illustrated by a proof-of-concept prototype. Thus, this active flexure-based solution has the potential to make actuated assistive orthoses smaller, lighter and less conspicuous. Conceptually, the use of a flexure-based architecture in this active mechanism provides an effective means to achieve suitable transmissions behaviors and to utilize small actuator strokes within a confined space. Still, further improvements for better biomechanical compatibility with the body and a higher power density are necessary to make it viable for practical use. The chapter followed an exploratory approach and in contrast to the devices in Part I the actuator design was developed ad hoc without any distinct substeps. The combination of flexures and soft actuator technologies with the goal to build a compact bending actuator is a concept new to the field of wearable assistive devices. Thus, this chapter may serve as an inspiration or starting point for future research that aims to further explore this new class of semi-soft actuators.

Overall, this thesis shows that flexure-based designs provide promising new solutions to improve upper-limb wearable assistive devices across a wide range of applications. Concrete designs have been proposed that show several distinct advantages compared to traditional rigid-link mechanisms. Furthermore, a universal synthesis methodology, which employs beam-based multibody models in combination with global optimization solvers, is presented. It was successfully applied throughout all main chapters of this thesis and provides the conceptual framework and the tools to recreate the work and adapt it to new custom use cases. Moreover, the design insights that have been gained in the course of this research and that are presented in thesis will help to guide future work in the research and development of well-performing, close-fitting and comfortable compliant assistive devices.

7.1 OUTLOOK

For future work following in the footsteps of this thesis many potential leads are discussed in the individual chapters as well as in the overall discussion chapter. However, it seems unlikely that by simply following the same approach as this thesis continued performance yields can be achieved that will eventually culminate in the perfect device. Starting from a new performance baseline, future work will need to develop new ideas and concepts to further push the technologies towards that goal. To this end, the ever-increasing abundance of computing resources will certainly aid in the process, but disruptive technologies may also open up new unforeseen

opportunities. What appears obvious, however, is that future devices will need to become more compliant and close-fitting to satisfy the user's requirements regarding wearing comfort and aesthetic appearance.

With respect to the passive assistive devices several developments are visible. In the course of this doctoral research several companies entered the market with their respective shoulder support devices for assisting work-related tasks, which in the meantime already reached their second or third product generation. These devices offer gravity compensation to the shoulder joint either through precise or approximate gravity balancing, and have promising prospects in improving work safety and reducing long-term injuries. As they previously have done, they will likely continue to evolve, whereby a trend towards more compliant designs is foreseeable. For example, similar to the work presented in this thesis, the Skelex devices [61] use a flexure for both storing energy and as part of the load-bearing structure. Also, instead of the formerly rather bulky rigid-link design in the EksoVest, the recently introduced EVO from Ekso Bionics [16] uses an adaptive back frame consisting of a chain of rigid linkages combined with an elastic band routed through the links to add internal stiffness. This gradual trend towards incorporating compliance into the design will likely continue. However, whether the flexure-based technologies proposed in this thesis will ever be fully adapted remains an open question.

Another foreseeable trend is the permeation of the technologies from work-assist devices into other fields, such as rehabilitation and assistance of activities of daily living. Here, Ekso Bionics [16] provides another example with their also recently introduced EksoUE, which appears to be a slightly modified version of the EksoVest. However, as their progenitor, these descendants of the work-assist devices will – at least in the near future – likely only feature shoulder support. Still, this is a very positive trend, as passive upper-limb wearable assistive devices directly originating from the fields of rehabilitation and daily assistance are scarce, and the interest in the development of new such devices seems to remain low and limited to sporadic academic research.

In the recent years, the development of active devices received a boost through the emerging soft actuation technologies. These currently offer the most promising solution for lightweight and close-fitting devices, and in comparison to passive devices are furthermore able to provide more universal support, making them potentially useful beyond task-specific contexts. To this end, this thesis revealed a promising new direction. Still, the success of active devices is closely tied to the developments in energy storage technologies. Provided that battery capacity, i.e., their energy density and specific energy continue to increase, it seems plausible that active devices will eventually supersede the currently prevalent passive devices.

Ultimately, the probably most important questions with respect to the future are: how quickly, and if ever, will these assistive technologies find widespread adoption; and how long will they continue to have practical relevance? For rehabilitation and especially daily assistance the devices have not yet reached a sufficiently high level of functional and social acceptability to be widely adopted in the near future. In work-related settings the long-term benefit of upper-limb assistive devices to prevent

injury, e.g., musculoskeletal disorders, is still not conclusively proven. Furthermore, as long as the use of assistive orthoses does not translate to an increase in productivity, the motivation of employers to equip their workforce with these will remain low. Though rehabilitation and work related setting currently show the largest rate of adoption, their use seems to be limited to a few flagship projects in developed countries. To overcome these thresholds assistive upper-limb devices need to improve both technically and aesthetically, and better incentive structures for their adoption need to be established.

Considering long-term developments, the widespread demand for wearable assistive devices is likely to decrease. With the increasing automation in manufacturing, construction, agriculture and logistics strenuous manual labor will become increasingly rare. Also, as medicine continues to progress and conditions that lead to deficient motor function like stroke, muscular dystrophy or spinal chord injury become better treatable and potentially healable, assistive orthoses for daily assistance and even those used in rehabilitation training may eventually become obsolete. Therefore, also in the future, wearable assistive devices are likely to remain a niche market product.

References

- [1] T. Abe, S. Koizumi, H. Nabae, G. Endo, and K. Suzumori. “Muscle textile to implement soft suit to shift balancing posture of the body”. In: *2018 IEEE 1st International Conference on Soft Robotics (RoboSoft)*. 2018, pp. 572–578.
- [2] T. Abe, S. Koizumi, H. Nabae, G. Endo, K. Suzumori, N. Sato, M. Adachi, and F. Takamizawa. “Fabrication of ‘18 Weave’ muscles and their application to soft power support suit for upper limbs using thin McKibben muscle”. In: *IEEE Robotics and Automation Letters* 4.3 (2019), pp. 2532–2538.
- [3] *Airframe™*. Levitate Technologies, San Diego, CA, USA. URL: levitatetech.com.
- [4] V. Arakelian. “Gravity compensation in robotics”. In: *Advanced Robotics* 30.2 (2016), pp. 79–96.
- [5] K. P. Ashwin and A. Ghosal. “A survey on static modeling of miniaturized pneumatic artificial muscles with new model and experimental results”. In: *Applied Mechanics Reviews* 70.4 (2018), pp. 040802–040802–20.
- [6] S. Casini, M. Morvidoni, M. Bianchi, M. Catalano, G. Grioli, and A. Bicchi. “Design and realization of the CUFF - clenching upper-limb force feedback wearable device for distributed mechano-tactile stimulation of normal and tangential skin forces”. In: *2015 IEEE/RSJ International Conference on Intelligent Robots and Systems (IROS)*. 2015, pp. 1186–1193.
- [7] J. Chen and P. S. Lum. “Spring operated wearable enhancer for arm rehabilitation (SpringWear) after stroke”. In: *2016 38th Annual International Conference of the IEEE Engineering in Medicine and Biology Society (EMBC)*. 2016, pp. 4893–4896.
- [8] J. Chen and P. S. Lum. “Pilot testing of the spring operated wearable enhancer for arm rehabilitation (SpringWear)”. In: *Journal of NeuroEngineering and Rehabilitation* 15.1 (2018), p. 13.
- [9] Z. Cheng, S. Foong, D. Sun, and U. X. Tan. “Algorithm for design of compliant mechanisms for torsional applications”. In: *2014 IEEE/ASME International Conference on Advanced Intelligent Mechatronics*. 2014, pp. 628–633.
- [10] Z. Cheng, S. Foong, D. Sun, and U. X. Tan. “Towards a multi-DOF passive balancing mechanism for upper limbs”. In: *2015 IEEE 14th International Conference on Rehabilitation Robotics (ICORR)*. 2015, pp. 508–513.
- [11] C.-P. Chou and B. Hannaford. “Measurement and modeling of McKibben pneumatic artificial muscles”. In: *IEEE Transactions on Robotics and Automation* 12.1 (1996), pp. 90–102.

- [12] C.-Y. Chu and R. M. Patterson. “Soft robotic devices for hand rehabilitation and assistance: a narrative review”. In: *Journal of NeuroEngineering and Rehabilitation* 15.1 (2018). Art. no. 9.
- [13] F. Daerden and D. Lefeber. “Pneumatic artificial muscles: actuators for robotics and automation”. In: *European Journal of Mechanical and Environmental Engineering* 47 (2002).
- [14] A. G. Dunning and J. L. Herder. “A review of assistive devices for arm balancing”. In: *2013 IEEE 13th International Conference on Rehabilitation Robotics (ICORR)*. 2013, pp. 1–6.
- [15] A. G. Dunning, M. M. H. P. Janssen, P. N. Kooren, and J. L. Herder. “Evaluation of an arm support with trunk motion capability”. In: *Journal of Medical Devices* 10.4 (2016).
- [16] *EksoVest, EksoUE & EVO*. Ekso Bionics, Richmond, CA, USA. URL: eksobionics.com.
- [17] *Feinpolyamide PA 2200 for EOSINT P*. EOS GmbH – Electro Optical Systems. 2004. URL: materflow.com/wp-content/uploads/2018/07/material-data-pa2200.pdf.
- [18] L. Franco, G. Salvietti, and D. Prattichizzo. “Command acknowledge through tactile feedback improves the usability of an EMG-based interface for the frontalis muscle”. In: *2019 IEEE World Haptics Conference (WHC)*. 2019, pp. 574–579.
- [19] L. Franco, M. Tschiersky, G. Wolterink, F. Barontini, M. Poggiani, M. Catalano, G. Grioli, M. Bianchi, A. Bicchi, S. Rossi, D. Prattichizzo, and G. Salvietti. “The SoftPro Wearable System for grasp compensation in stroke patients”. In: *Wearable Robotics: Challenges and Trends*. Proceedings of the 5th International Symposium on Wearable Robotics, Werob2020, and of Wearacon Europe 2020. Vol. 27. 1. 2021. Chap. 59.
- [20] Y. Funabara. “Flexible fabric actuator realizing 3D movements like human body surface for wearable devices”. In: *2018 IEEE/RSJ International Conference on Intelligent Robots and Systems (IROS)*. 2018, pp. 6992–6997.
- [21] R. Gopura, D. Bandara, K. Kiguchi, and G. K. I. Mann. “Developments in hardware systems of active upper-limb exoskeleton robots: a review”. In: *Robotics and Autonomous Systems* 75 (2016), pp. 203–220.
- [22] C. J. W. Haarman, E. E. G. Hekman, H. S. Rietman, and H. van der Kooij. “Pushing the limits: a novel tape spring pushing mechanism to be used in a hand orthosis”. In: *Wearable Robotics: Challenges and Trends*. Ed. by M. C. Carrozza, S. Micera, and J. L. Pons. Springer International Publishing, 2019, pp. 475–479.
- [23] T. Haumont, T. Rahman, W. Sample, M. M. King, C. Church, J. Henley, and S. Jayakumar. “Wilmington Robotic Exoskeleton: a novel device to maintain arm improvement in muscular disease”. In: *Journal of Pediatric Orthopaedics* 31 (2011).

- [24] T. Hiramitsu, K. Suzumori, H. Nabae, and G. Endo. "Experimental evaluation of textile mechanisms made of artificial muscles". In: *2019 IEEE 2nd International Conference on Soft Robotics (RoboSoft)*. 2019, pp. 1–6.
- [25] J. Hull, R. Turner, A. A. Simon, and A. T. Asbeck. "A novel method and exoskeletons for whole-arm gravity compensation". In: *IEEE Access* 8 (2020), pp. 143144–143159.
- [26] I. Hussain, G. Salvietti, G. Spagnoletti, and D. Prattichizzo. "The Soft-SixthFinger: a wearable EMG controlled robotic extra-finger for grasp compensation in chronic stroke patients". In: *IEEE Robotics and Automation Letters* 1.2 (2016), pp. 1000–1006.
- [27] S. Iranzo, A. Piedrabuena, D. Iordanov, U. Martinez-Iranzo, and J.-M. Belda-Lois. "Ergonomics assessment of passive upper-limb exoskeletons in an automotive assembly plant". In: *Applied Ergonomics* 87 (2020), p. 103120.
- [28] *Hardness tests and hardness number conversions*. Standard. SAE International, 2018.
- [29] J. B. Jonker and J. P. Meijaard. "SPACAR – computer program for dynamic analysis of flexible spatial mechanisms and manipulators". In: *Multibody Systems Handbook*. Ed. by W. Schiehlen. Berlin, Heidelberg: Springer Berlin Heidelberg, 1990, pp. 123–143.
- [30] H. Kim, J. Min, and J. Song. "Multiple-degree-of-freedom counterbalance robot arm based on slider-crank mechanism and bevel gear units". In: *IEEE Transactions on Robotics* 32.1 (2016), pp. 230–235.
- [31] S. Kim, M. A. Nussbaum, M. I. Mokhlespour Esfahani, M. M. Alemi, S. Alabdulkarim, and E. Rashedi. "Assessing the influence of a passive, upper extremity exoskeletal vest for tasks requiring arm elevation: part I – 'expected' effects on discomfort, shoulder muscle activity, and work task performance". In: *Applied Ergonomics* 70 (2018), pp. 315–322.
- [32] H. Kobayashi, Y. Ishida, and H. Suzuki. "Realization of all motion for the upper limb by a muscle suit". In: *2004 IEEE 13th International Workshop on Robot and Human Interactive Communication (RO-MAN)*. 2004, pp. 631–636.
- [33] S. Koizumi, S. Kurumaya, H. Nabae, G. Endo, and K. Suzumori. "Braiding thin McKibben muscles to enhance their contracting abilities". In: *IEEE Robotics and Automation Letters* 3.4 (2018), pp. 3240–3246.
- [34] P. N. Kooren, J. Lobo-Prat, A. Q. L. Keemink, M. M. Janssen, A. H. A. Stienen, I. J. M. de Groot, M. I. Paalman, R. Verdaasdonk, and B. F. J. M. Koopman. "Design and control of the Active A-Gear: a wearable 5 DOF arm exoskeleton for adults with Duchenne muscular dystrophy". In: *2016 IEEE 6th International Conference on Biomedical Robotics and Biomechatronics (BioRob)*. 2016, pp. 637–642.

- [35] P. N. Kooren, A. G. Dunning, M. M. H. P. Janssen, J. Lobo-Prat, B. F. J. M. Koopman, M. I. Paalman, I. J. M. de Groot, and J. L. Herder. “Design and pilot validation of A-Gear: a novel wearable dynamic arm support”. In: *Journal of NeuroEngineering and Rehabilitation* 12.1 (2015), p. 83.
- [36] C. S. Kothera, M. Jangid, J. Sirohi, and N. M. Wereley. “Experimental characterization and static modeling of McKibben actuators”. In: *Journal of Mechanical Design* 131.9 (2009), pp. 091010-091010-10.
- [37] S. Kurumaya, H. Nabae, G. Endo, and K. Suzumori. “Design of thin McKibben muscle and multifilament structure”. In: *Sensors and Actuators A: Physical* 261 (2017), pp. 66-74.
- [38] P. de Leva. “Adjustments to Zatsiorsky-Seluyanov’s segment inertia parameters”. In: *Journal of Biomechanics* 29.9 (1996), pp. 1223-1230.
- [39] P. Maciejasz, J. Eschweiler, K. Gerlach-Hahn, A. Jansen-Troy, and S. Leonhardt. “A survey on robotic devices for upper limb rehabilitation”. In: *Journal of NeuroEngineering and Rehabilitation* 11.1 (2014). Art. no. 3.
- [40] S. K. Manna and V. N. Dubey. “Comparative study of actuation systems for portable upper limb exoskeletons”. In: *Medical Engineering & Physics* 60 (2018), pp. 1-13.
- [41] MATE. Comau, Turin, Italy. URL: comau.com.
- [42] P. Maurice, J. Čamernik, D. Gorjan, B. Schirrmeister, J. Bornmann, L. Tagliapietra, C. Latella, D. Pucci, L. Fritzsche, S. Ivaldi, and J. Babič. “Objective and subjective effects of a passive exoskeleton on overhead work”. In: *IEEE Transactions on Neural Systems and Rehabilitation Engineering* 28.1 (2020), pp. 152-164.
- [43] T. McFarland and S. Fischer. “Considerations for industrial use: a systematic review of the impact of active and passive upper limb exoskeletons on physical exposures”. In: *IIEE Transactions on Occupational Ergonomics and Human Factors* 7.3-4 (2019), pp. 322-347.
- [44] J. P. Meijaard. “Fluid-conveying flexible pipes modeled by large-deflection finite elements in multibody systems”. In: *Journal of Computational and Nonlinear Dynamics* 9.1555-1415 (2014).
- [45] I. A. Murray and G. R. Johnson. “A study of the external forces and moments at the shoulder and elbow while performing every day tasks”. In: *Clinical Biomechanics* 19.6 (2004), pp. 586-594.
- [46] T. Noritsugu. “Pneumatic soft actuator for human assist technology”. In: *Proceedings of the 6th JFPS International Symposium on Fluid Power, Tsukuba*. 2005, pp. 11-20.
- [47] A. Ohno, H. Nabae, and K. Suzumori. “Static analysis of powered low-back orthosis driven by thin pneumatic artificial muscles considering body surface deformation”. In: *2015 IEEE/SICE International Symposium on System Integration (SII)*. 2015, pp. 39-44.

- [48] A. Oosterwijk, M. Nieuwenhuis, C. van der Schans, and L. Mouton. "Shoulder and elbow range of motion for the performance of activities of daily living: a systematic review". In: *Physiotherapy Theory and Practice* 34.7 (2018). PMID: 29377745, pp. 505–528.
- [49] *PA 2200 Performance 1.0 (PA12)*. EOS GmbH – Electro Optical Systems. 2010. URL: eos.materialdatacenter.com.
- [50] I. Pacifico, A. Scano, E. Guanziroli, M. Moise, L. Morelli, A. Chiavenna, D. Romo, S. Spada, G. Colombina, F. Molteni, F. Giovacchini, N. Vitiello, and S. Crea. "An experimental evaluation of the Proto-MATE: a novel ergonomic upper-limb exoskeleton to reduce workers' physical strain". In: *IEEE Robotics & Automation Magazine* 27.1 (2020), pp. 54–65.
- [51] *PAEXO*. Ottobock, Duderstadt, Germany. URL: paexo.com.
- [52] D. H. Plettenburg. "The WILMER Elbow Orthosis". In: *2007 IEEE 10th International Conference on Rehabilitation Robotics*. 2007, pp. 1031–1035.
- [53] O. Plos, S. Buisine, A. Aoussat, F. Mantelet, and C. Dumas. "A universalist strategy for the design of assistive technology". In: *International Journal of Industrial Ergonomics* 42.6 (2012), pp. 533–541.
- [54] G. Radaelli and J. L. Herder. "A monolithic compliant large-range gravity balancer". In: *Mechanism and Machine Theory* 102. Supplement C (2016), pp. 55–67.
- [55] G. Radaelli and J. L. Herder. "Isogeometric shape optimization for compliant mechanisms with prescribed load paths". In: *ASME 2014 International Design Engineering Technical Conferences and Computers and Information in Engineering Conference (DETC2014)*. Vol. 5A: 38th Mechanisms and Robotics Conference. 2014.
- [56] G. Radaelli and J. L. Herder. "Shape optimization and sensitivity of compliant beams for prescribed load-displacement response". In: *Mechanical Sciences* 7.2 (2016), pp. 219–232.
- [57] T. Rahman, W. Sample, S. Jayakumar, M. M. King, J. Yong Wee, R. Seliktar, M. Alexander, M. Scavina, and A. Clark. "Passive exoskeletons for assisting limb movement". In: *Journal of rehabilitation research and development* 43 (2006), pp. 583–90.
- [58] E. Rocon, A. F. Ruiz, R. Raya, A. Schiele, J. L. Pons, J. M. Belda-Lois, R. Poveda, M. J. Vivas, and J. C. Moreno. "Human-robot physical interaction". In: *Wearable Robots*. John Wiley & Sons, Ltd, 2008. Chap. 5, pp. 127–163.
- [59] G. Salvietti, I. Hussain, D. Cioncoloni, S. Taddei, S. Rossi, and D. Prattichizzo. "Compensating hand function in chronic stroke patients through the Robotic Sixth Finger". In: *IEEE Transactions on Neural Systems and Rehabilitation Engineering* 25.2 (2017), pp. 142–150.
- [60] *ShoulderX*. SuitX, Emeryville, CA, USA. URL: suitx.com.

- [61] *SkelEx*. Skel-Ex, Rotterdam, The Netherlands. URL: skelex.com.
- [62] M. Takaoka, K. Suzumori, S. Wakimoto, K. Iijima, and T. Tokumiya. "Fabrication of thin McKibben artificial muscles with various design parameters and their experimental evaluations". In: *The 5th International Conference on Manufacturing, Machine Design and Tribology (ICMDT2013)*. 2013, p. 82.
- [63] A. R. Tilley and Henry Dreyfuss Associates. *The measure of man and woman: human factors in design, revised edition*. Whitney Library of Design, 2001.
- [64] B. Tondu. "Modelling of the McKibben artificial muscle: a review". In: *Journal of Intelligent Material Systems and Structures* 23.3 (2012), pp. 225–253.
- [65] M. Tschiersky, E. E. G. Hekman, D. M. Brouwer, and J. L. Herder. "Gravity balancing flexure springs for an assistive elbow orthosis". In: *IEEE Transactions on Medical Robotics and Bionics* 1.3 (2019), pp. 177–188.
- [66] L. A. van der Heide, B. van NINHUIJS, A. Bergsma, G. J. Gelderblom, D. J. van der Pijl, and L. P. de Witte. "An overview and categorization of dynamic arm supports for people with decreased arm function". In: *Prosthetics and Orthotics International* 38.4 (2014). PMID: 23950551, pp. 287–302.
- [67] L. Van Engelhoven and H. Kazerooni. "Design and intended use of a passive actuation strategy for a shoulder supporting exoskeleton". In: *2019 Wearable Robotics Association Conference (WearRAcon)*. 2019, pp. 7–12.
- [68] R. J. Varghese, D. Freer, F. Deligianni, J. Liu, and G.-Z. Yang. "Chapter 3 - Wearable robotics for upper-limb rehabilitation and assistance: a review of the state-of-the-art, challenges, and future research". In: *Wearable Technology in Medicine and Health Care*. Ed. by R. K.-Y. Tong. Academic Press, 2018, pp. 23–69.
- [69] A. J. Veale and S. Q. Xie. "Towards compliant and wearable robotic orthoses: a review of current and emerging actuator technologies". In: *Medical Engineering & Physics* 38.4 (2016), pp. 317–325.
- [70] M. D. Volder, A. Moers, and D. Reynaerts. "Fabrication and control of miniature McKibben actuators". In: *Sensors and Actuators A: Physical* 166.1 (2011), pp. 111–116.
- [71] A. de Vries, M. Murphy, R. Könemann, I. Kingma, and M. de Looze. "The amount of support provided by a passive arm support exoskeleton in a range of elevated arm postures". In: *IIEE Transactions on Occupational Ergonomics and Human Factors* 7.3-4 (2019), pp. 311–321.
- [72] B. Wang, K. C. Aw, M. Biglari-Abhari, and A. McDaid. "Design and fabrication of a fiber-reinforced pneumatic bending actuator". In: *2016 IEEE International Conference on Advanced Intelligent Mechatronics (AIM)*. 2016, pp. 83–88.
- [73] *Wilmington Robotic Exoskeleton (WREX)*. JAECO Orthopedic, Hot Springs, AR, USA. URL: jaecoorthopedic.com.
- [74] G. Wolterink, P. Dias, R. G. P. Sanders, F. Muijzer, B.-J. van Beijnum, P. Veltink, and G. Krijnen. "Development of soft sEMG sensing structures using 3D-printing technologies". In: *Sensors* 20.15 (2020), p. 4292.

- [75] *Z-ULTRAT technical data sheet*. Zortrax S.A. 2018. URL: cf.zortrax.com/wp-content/uploads/2018/06/Z-ULTRAT_Technical_Data_Sheet_eng.pdf.
- [76] C. Zeagler, M. Gandy, and P. M. Baker. “The assistive wearable: inclusive by design”. In: *Assistive Technology Outcomes and Benefits* 12 (2018), pp. 11–36.

List of publications

JOURNAL ARTICLES

First author

- M. Tschiersky, E.E.G. Hekman, J.L. Herder, D.M. Brouwer. “Gravity balancing flexure spring mechanisms for shoulder support in assistive orthoses”. Submitted to *IEEE Transactions on Medical Robotics and Bionics*.
- M. Tschiersky, E.E.G. Hekman, J.L. Herder, D.M. Brouwer, K. Suzumori. “A compact McKibben muscle based bending actuator for close-to-body application in assistive wearable robots”. *IEEE Robotics and Automation Letters* vol. 5 no. 2 (2020), pp. 3042–3049.
- M. Tschiersky, E.E.G. Hekman, D.M. Brouwer, J.L. Herder. “Gravity balancing flexure springs for an assistive elbow orthosis”. *IEEE Transactions on Medical Robotics and Bionics* vol. 1 no. 3 (2019) pp. 177–188.

Co-author

- L. Franco, M. Tschiersky, G. Wolterink, M. Bianchi, A. Bicchi, F. Barontini, M. Catalano, G. Grioli, M. Poggiani, S. Rossi, D. Prattichizzo and G. Salvietti. “Integration of a passive exoskeleton and a robotic supernumerary finger for grasping compensation in chronic stroke patients: The SoftPro Wearable System”. Submitted to *Frontiers in Robotics and AI*.

CONFERENCE CONTRIBUTIONS

First author

- M. Tschiersky, E.E.G. Hekman, J.L. Herder, D.M. Brouwer, K. Suzumori. “A compact McKibben muscle based bending actuator for close-to-body application in assistive wearable robots”. *2020 IEEE International Conference on Robotics and Automation, ICRA 2020 – Virtual Conference* (2020). Paris, France.¹
- M. Tschiersky, G. Berselli, J.L. Herder, D.M. Brouwer, S. Stramigioli. “PZT-actuated compliant locking device”. *Proceedings of The 33rd Annual Meeting of the American Society for Precision Engineering* (2018) pp. 174–179. Las Vegas, NV, USA.

¹published in the *IEEE Robotics and Automation Letters* vol. 5 no. 2 (2020), pp. 3042–3049.

Co-author

- L. Franco, M. Tschiersky, G. Wolterink, F. Barontini, M. Poggiani, M. Catalano, G. Grioli, M. Bianchi, A. Bicchi, S. Rossi, D. Prattichizzo and G. Salvietti. “The SoftPro Wearable System for Grasp Compensation in Stroke Patients”. *Wearable Robotics: Challenges and Trends; Proceedings of the 5th International Symposium on Wearable Robotics, WeRob2020, and of WearRAcon Europe 2020 – Virtual Conference* (2021). Vigo, Spain.
- A. Birkholz, M. Tschiersky, J. Wortberg. “Injection molding simulation with vario-thermal mold temperature control of highly filled polyphenylene sulfide”. *Proceedings of The 30th International Conference of the Polymer Processing Society* vol. 1664 (2015). Cleveland, OH, USA.

For future publications, please refer to my Open Researcher and Contributor ID.

ORCID iD: 0000-0002-4866-3175

Résumé

Martin Tschiersky

Date of Birth: 17/05/1989

Place of Birth: Düsseldorf, Germany

Nationality: German



EDUCATION

2016 – 2021	Doctor of Philosophy in Mechanical Engineering University of Twente, Enschede
2019	Visiting Researcher Tokyo Institute of Technology, Tokyo
2014 – 2016	Scholar of the German Academic Exchange Service (DAAD) 'Language and Practical Experience in Japan' Programme
2012 – 2014	Master of Science in Mechanical Engineering University of Duisburg-Essen, Duisburg
2008 – 2012	Bachelor of Science in Mechanical Engineering University of Duisburg-Essen, Duisburg
1999 – 2008	High School Friedrich-Rückert-Gymnasium, Düsseldorf

PROFESSIONAL EXPERIENCE

2015 – 2016	Intern Bosch Corporation, Tokyo
2011 – 2013	Student Employee University of Duisburg-Essen, Duisburg

HONORS & AWARDS

- | | |
|------|--|
| 2019 | FY2019 Postdoctoral Fellowship for Research in Japan (Short-term)
Japan Society for the Promotion of Science (JSPS) |
| 2014 | Brose Prize 2014
Scientific Alliance of Polymer Technology (WAK) |
| 2014 | 'Language and Practical Experience in Japan' Scholarship
German Academic Exchange Service (DAAD) |
| 2014 | Master of Science <i>summa cum laude</i>
University of Duisburg-Essen |

Acknowledgments

*[...] 'My name is Ozymandias, king of kings:
Look on my works, ye Mighty, and despair!
Nothing beside remains. Round the decay
Of that colossal wreck, boundless and bare
The lone and level sands stretch far away.*

Ozymandias — Percy Bysshe Shelley

Every good thesis should have at least one pretentious quote – and this one is mine. Judging from personal experience, this part of the thesis is likely to be read by more people than even the summary. So, I'll try to do my best:

First, I would like to express my gratitude towards my supervision team. Just, Dannis and Edsko, thank you for your continued support and valuable feedback without which this thesis would not have been possible. Our regular discussions always remained a source of motivation and a helpful way to correct my course when necessary. I can say with full honesty that I enjoyed most of them, even. . . no, maybe especially when they went off on a tangent. Playing 'big brain sports' when crafting my propositions was unquestionably one of the highlights.

Just, thank you for taking me in as your PhD student and for continuing my supervision after leaving Twente. Though we didn't have the chance to spend much time in person since, I fondly remember my visits to Delft and our trips abroad. Those trips were not only a rare chance to talk with you in person, but also gave me an educational glimpse into the high art of academic diplomacy.

Dannis, thank you for 'adopting' me as your PhD student and making me a genuine member of the PE group. I truly appreciate your effort in taking an active and invested role in my supervision, even though you joined the supervision team at a relatively late stage. Precision engineering may not have been perfectly aligned with the topic of my thesis, but I really enjoyed this different aspect of my work and the trip to Las Vegas was certainly a welcome bonus.

Edsko, thank you for having been a very reliable and consistent part of my supervision team. Your detailed and in-depth feedback on my papers and on my thesis, with respect to contents and even down to specific wording, was always much appreciated.

To all of you, but also to Prof. Suzumori and Ms. Suzuki, I would like to express a special thank-you for supporting my plan to conduct a research stay in Japan.

A dedicated thanks goes to Prof. Suzumori and all members of the Suzumori-Endo lab. Even though I only had the chance to stay with you for four months, I immediately felt welcome and as part of the team. That time – especially our Nomikai, the trip to Ibaraki-ken and the Baka-zemi – has been one of the most memorable episodes of my PhD trajectory. Also, thank you German for your help and making that time even more enjoyable.

My gratitude also extends to the members of the graduation committee, Dirk Lefeber, Conor Walsh, Hans Rietman and Herman van der Kooij, who took the time to assess my work and provided valuable feedback on my manuscript.

Next, I would like to thank my three dearest colleagues who were there for me from the first day and accompanied me throughout my journey of becoming a respectable researcher in the world of academia: dr. Marijn, dr. Jan and Mark. Thank you for always offering me your help when needed. While learning SPACAR – I may recall, after you coaxed me into using it – I was undoubtedly not shy of needing that help.

Marijn, thank you for sharing the road with me – both figuratively and literally. I cannot say that I like it much when you often refute my assertions and call me out on my complacency, but it may have helped to shed at least a tiny fraction of my arrogance and ignorance along the way. Still, aside from being a great colleague, I got to know you as a good friend to have plenty of beers and steaks with, and as an excellent companion on road trips. The grand tour through the national parks and metropolises of the US west coast will remain in good memory – *that's true*.

Jan, I always appreciated your open and welcoming nature. After having been shoved into an office that had more throughput of people than your average train station lobby, you have remained my loyal companion. But also your eagerness to organize intellectual exchanges, e.g., with our sister group in Delft and your ballistic cycling style will be remembered.

Mark, it never ceased to amaze me how much noise someone can make by simply sitting in a chair. However, after getting used to the elevated noise levels you have turned out to be a great colleague and my personal role model when it comes to work efficiency. Sometimes when I got lost in minuscule details of my work, I only had to recall your famous motto: “dat moet je ook niet willen”.

Thank you, also, to all the other members of the extended PE family and the ‘corridor crew’, current and past. Leo, thank you for helping me building my setups and for your technical support throughout the years. Martina, Debbie, Axel, Belinda and Tjerkje thank you for your assistance, especially when dealing with the university bureaucracy. Ronald, Wouter H., Jaap, Gert-willem, Johannes, Koen, Wout, Bram, Wouter v. D., Sil, Tim and Rick, thank you for for being interesting colleagues and great company during coffee breaks.

Boukje and Jurnan, thank you for the friendly exchange between the rivaling factions of the corridor, and for being great company during after-work dinners and beers. Luis, thank you for being a great study mate on our quest of beating DPPM2 and for being one of the more pleasant people to share an office with. To all members of the laser group: I liked you more when you were still part of WA, but you remained very good neighbors on the corridor. Finally, though you don't all fit into one set category: Abijeet, Earvin, Mieke, Farnaz, Farshad and Łukas, it was nice having you around.

Marek danke, dass du das Landleben diesseits der Grenze erträglicher gemacht hast. Ich hoffe es wird nicht das letzte Mal gewesen sein, dass wir bei BBQ, Bier, Whiskey und Tatra-Tee zusammensaßen.

Lars, Nina and Anders, thank you for having done your graduation projects with me.

Giovanni, thank you for the joint work on our paper and your great hospitality during my short stay in Genoa.

Johan, Martin W. and Martin A., thank you for the good cooperation during the project. The work on our demonstrator was not the most relaxing, but you made it a nice experience after all. Stefano, Gijs, Peter, Ed, Bert-Jan, Frodo, Benjamin, Gerjan, Claudia and Freek, thank you for the great company during our trips to the numerous consortium meetings. Leonardo, thank you for taking the effort of compiling our integrator research into a paper, and for letting me use your figures in my thesis. To all the other members of the SoftPro consortium: thank you for the generous hospitality during our meetings. The food was always excellent. However, some presentations could have been shorter, so we could have enjoyed it a bit earlier.

Werner, Freek, Reinier and 'that guy' (Oliver), the trip to Montréal showed me what a PhD is really about – traveling abroad on the university's budget. If I remember correctly, there should be some deep knowledge engraved on the inside of my skull now, but craft beer seemed to have been an effective tool to wash that nonsense away.

Frikandel, Krokot and Mexicano, thank you for being great staples during the numerous lunch breaks at the overpriced cafeteria.

Nicht zuletzt gilt mein Dank auch Familie und Freunden, nah und fern. Ihr habt stets dazu beigetragen die Zeit (auch) abseits der Arbeit schön zu gestalten.

Lastly, to anyone who may continue in the footsteps of my work I would like to recite the words a wise man told me once: "It's only a piece of plastic – how hard can it be?"

